24 Copy

3896

REPORT No. ER-3911

THE SNAP II POWER CONVERSION SYSTEM

TOPICAL REPORT No. 3 DYNAMIC ANALYSIS

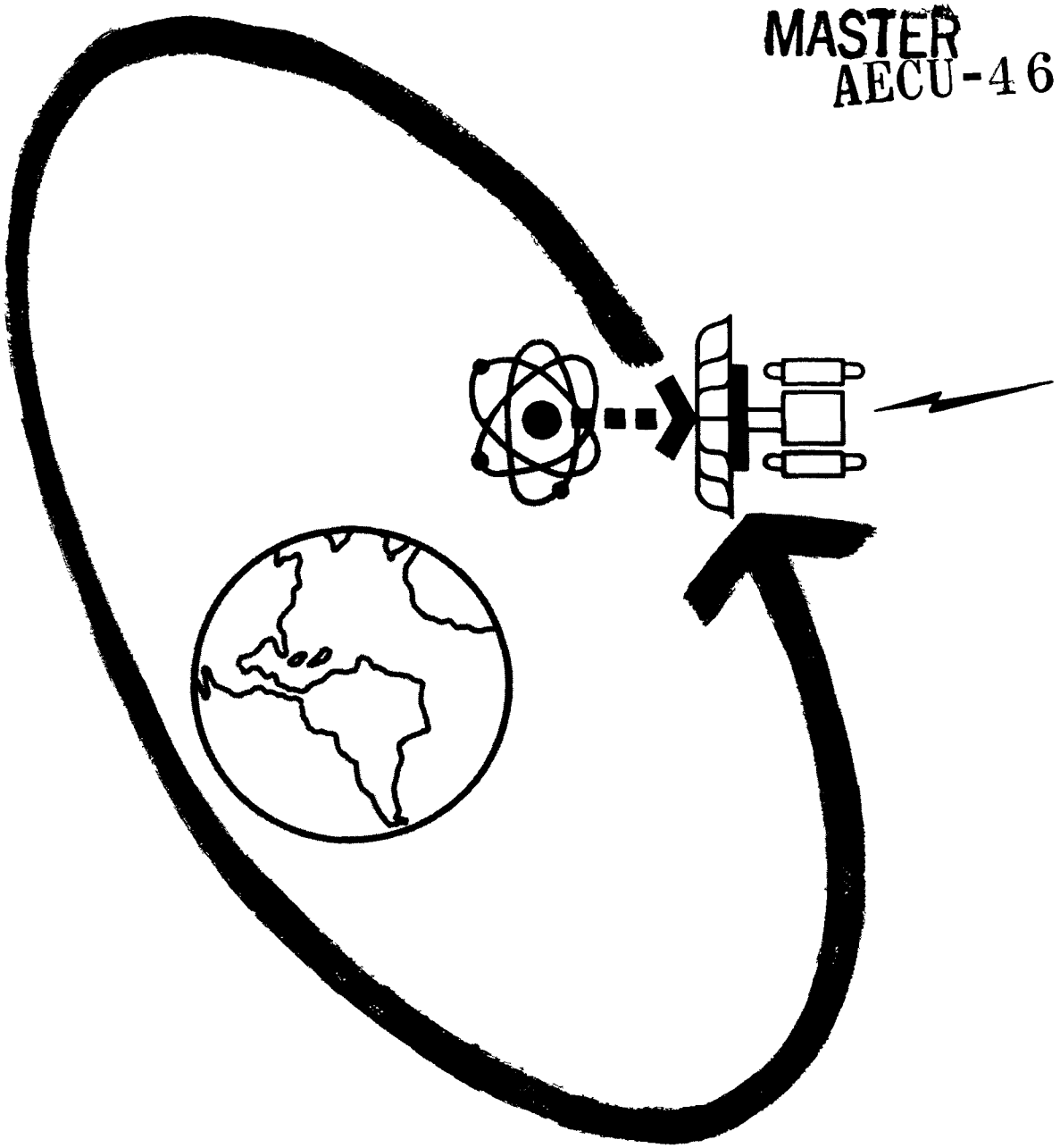

STAFF RESEARCH AND DEVELOPMENT
THOMPSON PRODUCTS DIVISIONS
Thompson Ramo Wooldridge Inc.
CLEVELAND, OHIO

DISCLAIMER

PROJECT

562-007252-88

AF [illegible] 355

REPORT NO. ER 3911

THE SNAP II POWER CONVERSION SYSTEM

TOPICAL REPORT NO. 3

DYNAMIC ANALYSIS

PREPARED BY:	CHECKED BY:	APPROVED BY:
David L. Deibel Research Engineer	William J. Leovic Project Engineer	W. R. Chapman Manager - Engineering
Gene L Mrava Research Engineer	Donald L. Southam Project Manager	J. Ed Taylor Manager
Kurt Seldner Research Engineer		New Devices Laboratories

DATE

January 15, 1960

DEPARTMENT

8868

Thompson Ramo Wooldridge Inc.

CLEVELAND, OHIO, U. S. A.

LEGAL NOTICE

This report was prepared as an account of Government sponsored work. Neither the United States, nor the Commission, nor any person acting on behalf of the Commission:

A. Makes any warranty or representation, express or implied, with respect to the accuracy, completeness, or usefulness of the information contained in this report, or that the use of any information, apparatus, method, or process disclosed in this report may not infringe privately owned rights; or

B. Assumed any liabilities with respect to the use of or for damages resulting from the use of information, apparatus, method, or process disclosed in this report.

As used in the above, "person acting on behalf of the Commission" includes any employee or contractor of the Commission to the extent that such employee or contractor prepares, handles or distributes, or provides access to, any information pursuant to his employment or contract with the Commission.

ABSTRACT

SNAP II is the designation for a nuclear auxiliary power unit, designed primarily for utilization in the WS117L satellite vehicle. The SNAP II system consists of a reactor heat source, a mercury Rankine engine, and an alternator. Dynamic analysis of the power conversion system was conducted utilizing a comprehensive analog computer simulation. Feasibility of a parasitic load control for numerous system disturbances was demonstrated. This analysis was performed under a subcontract to Atomics International as part of the Atomic Energy Commission Contract No. AT (11-1)-GEN-8.

TABLE OF CONTENTS

DYNAMIC ANALYSIS OF THE SNAP II SYSTEM

I. SUMMARY

The mathematical model for an analog computer simulation of the SNAP II system is developed. Available data is combined with characteristics performance equations to provide a mathematical description of each component. The interrelations between variables are indicated by information flow diagrams for the individual elements. The computer diagrams are also given for each individual component.

From this computer study, the feasibility of a parasitic load control was established for all transients anticipated in an orbiting satellite.

II. INTRODUCTION

The function of the SNAP II system is to convert the heat energy available from a nuclear reactor into electrical energy to be delivered to a load. The method of conversion utilized is a Rankine cycle employing mercury as the working fluid. The Rankine engine is composed of a mercury boiler heated by a sodium heat transfer loop, an axial flow impulse turbine which extracts energy from the superheated mercury vapor, a condenser which returns the vapor to a liquid state and a mercury pump which returns the condensate to the boiler. The turbine directly drives the alternator, the mercury pump, and a permanent magnet induction sodium pump which is designed to circulate the sodium between the mercury boiler and the reactor.

Development of the mathematical model proceeded from analysis of the individual components such as the boiler, turbine, alternator, etc., and included consideration of additional effects such as transport delay in pipe lines, incident power radiation on the vehicle, etc. An overall information flow diagram is shown in Figure 1.

The photograph on the following page shows the computer installation at the Systems Analysis Laboratory of Thompson Ramo Wooldridge Incorporated. Five consoles of Electronics Associates equipment were available. For the SNAP II simulation approximately three of these consoles were used. Total equipment utilized was:

1. 140 operational amplifiers
2. 12 diode function generators
3. 12 servo multipliers
4. 20 electronic multipliers

The scale factors used throughout the simulation were as follows:

INFORMATION FLOW DIAGRAM - SNAP II SYSTEM

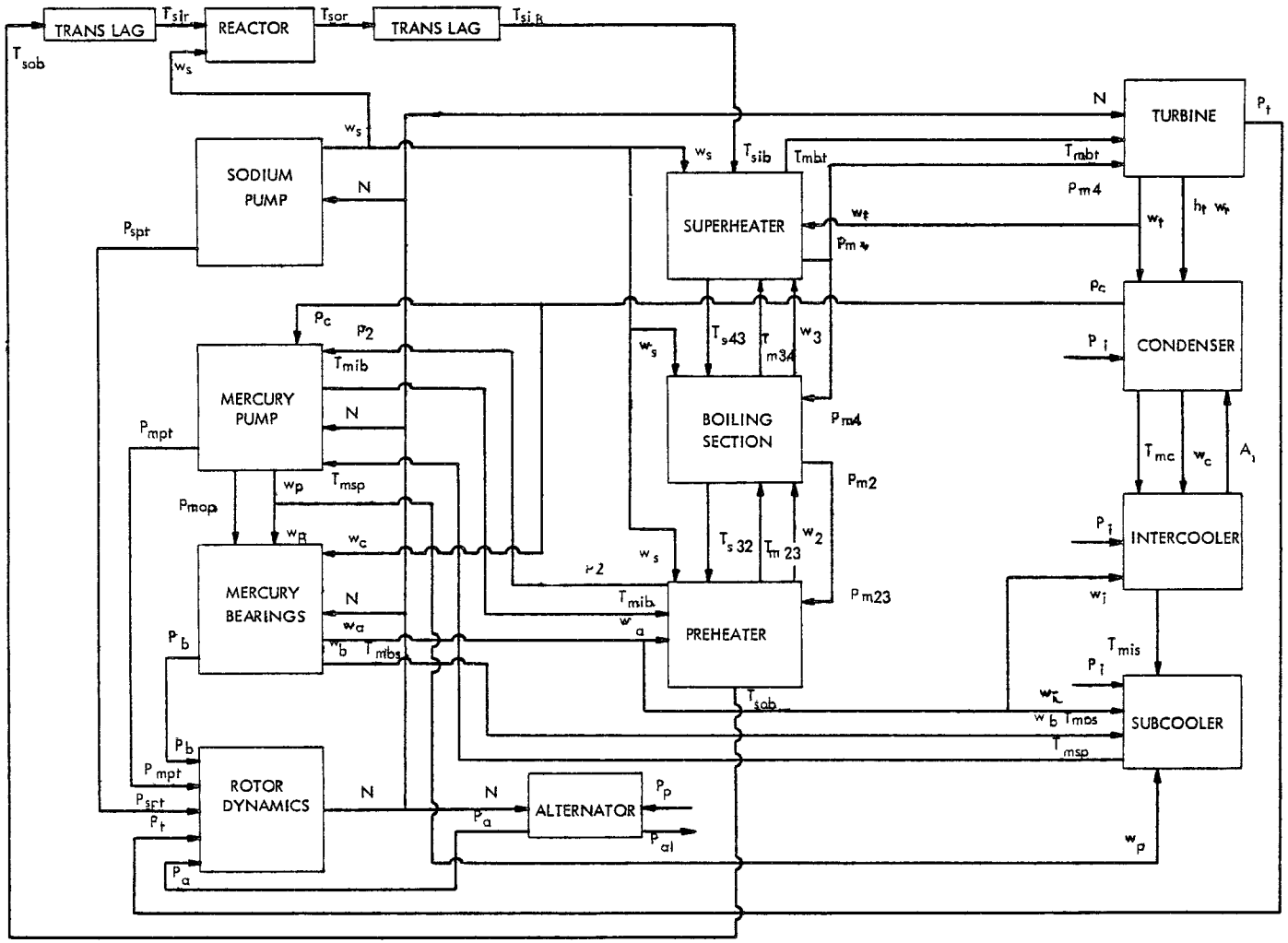

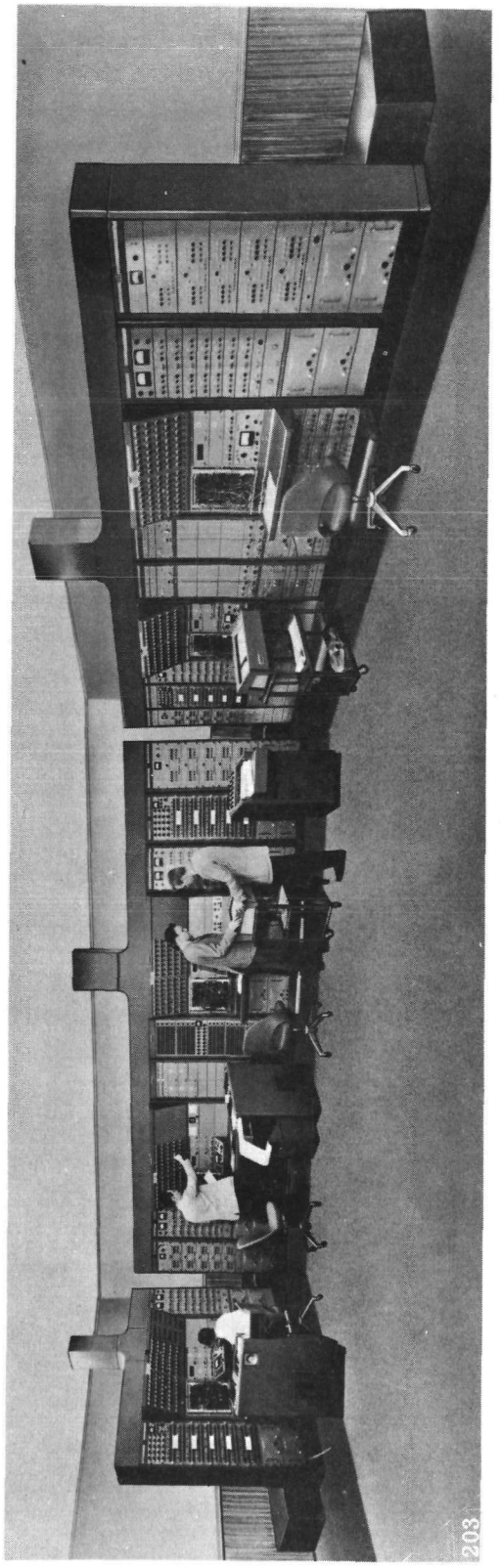

ANALOG COMPUTER

$$1 \text{ Volt} = 1^{\circ}F$$

$$1 \text{ Volt} = 1 \text{ psi}$$

$$1 \text{ Volt} = 1 \text{ rpm}$$

For example, if the output voltage equals 50.00 volts and its represents 0.05T, then the actual temperature is computed as shown below:

$$.05\,T = 50.00 \text{ Volts}$$

$$.05\,T = \frac{50.00 \text{ Volts}}{1 \text{ Volt}/^{\circ}F}$$

$$T = \frac{50.00}{.05} \,^{\circ}F$$

$$T = 1000^{\circ}F$$

III. COMPONENT DESCRIPTION

A. Heat Source

The heat source is a nuclear reactor from which heat energy is transferred into the sodium loop. The kinetic equation of the reactor describes the power output level as a function of changes in reactivity and effects introduced by delay neutrons groups. Changes in reactivity occur with variations in the temperature of the reactor vessel. The kinetic equations for a simplified version of the nuclear reactor are used to represent the power source; a negative temperature coefficient controls power output. The significant equations (1) and (2) and a block diagram are shown in Figure 2.

The thermodynamics of the reactor are specified in terms of the reactor power output and sodium flow. The effective heat capacities of the device are contributed by the fuel and enclosed sodium. If an unbalance exists between the transferred heat energy and that taken from the reactor by the sodium flow, a change in average temperature of the enclosed sodium will occur.

The heat transfer equations are of partial derivative form with independent time and space variables. The computer can accommodate only one independent variable (time) so that changes with respect to the geometrical variables must be expressed as difference equations. The geometry of the sodium flow through the reactor is such

REACTOR EQUATIONS

$$(1)\quad \dot{P}_r = \left[\frac{\delta k - \beta}{l^*} + \frac{\beta}{l^*} \quad \frac{1}{1 + S/\lambda} \right] P_r$$

$$(2)\quad \delta_k = \alpha (T_f - T_{fo})$$

$$(3)\quad W_f C_f \frac{d T_f}{dt} = P_r - A_{fs} U_{fs} (T_f - T_{sr})$$

$$(4)\quad W_{sr} C_s \frac{d T_{sr}}{dt} = A_{fs} U_{fs} (T_f - T_{sr}) + w_s C_s (T_{slr} - T_{sor})$$

$$(5)\quad T_{sor} = 2 T_{sr} - T_{slr}$$

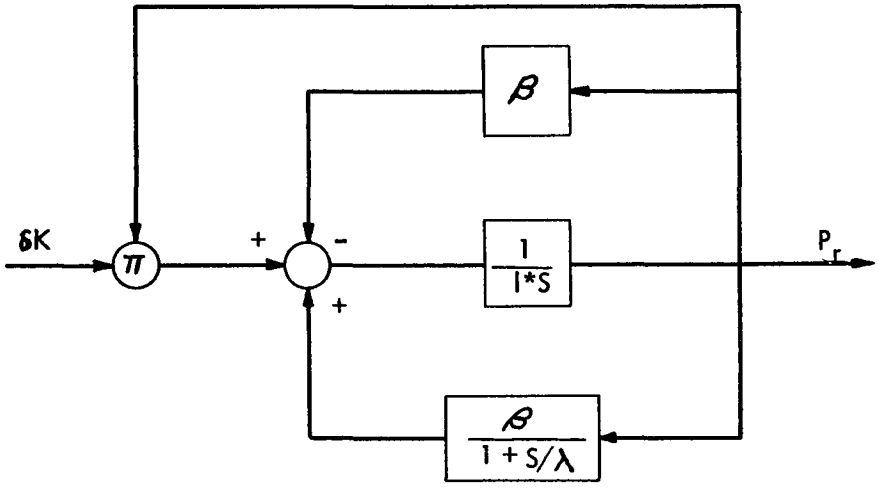

FIG. 2 BLOCK DIAGRAM - REACTOR KINETICS

that only one distance variable need be considered. The total length will be considered as a single cell. This concept may be modified if additional information shows that the difference interval selected leads to errors larger than anticipated. Equations (3), (4), and (5) describe the heat transfer in the reactor and Figure 3 shows the block diagram. The overall computer diagram for reactor kinetics and thermodynamics is shown in Figure 4.

B. Heat Exchanger

A change in mercury phase is accomplished in a sodium-to-mercury heat exchanger constructed of concentric tubes with mercury flowing in the inner tube and sodium in the annulus. The effective heat transfer source is considered to be the sodium and associated walls since the sodium-to-wall heat transfer resistance is much lower than the wall-to-mercury or wall-to-insulation resistances. The heat exchanger can be divided into three regions: preheat, boiling, and super heat. The heat transfer characteristics in all regions are expressed by partial differential equations. The assumption of flow in a single direction allows reduction to ordinary differential equations with the distribution of section lengths accounted for in difference equations.

The heat transfer coefficient is considered constant along the length of the preheater section. The net heat flow from the sodium to the preheater results in a change in average temperature of the sodium. The heat transferred to the mercury is proportional to the difference in average temperature of the two fluids. Excess heat absorbed by the mercury results in a rise in the average mercury temperature in this section or a change in preheater length required to bring the mercury to boiling temperature.

Equations (6) through (14) describe the heat transfer in the preheater. The block diagram is shown in Figure 5 and the computer diagram in Figure 6. Figure 7 shows the preheater exit temperature as a function of pressure as used in the simulation.

The center section of the heat exchanger, in which mercury is changed from liquid to vapor, may be divided into several sections if there exists a wide variance in heat transfer coefficient. Since steady state calculations show that a single boiling section representation closely approximates the heat transfer effects of a multiple section consideration, a single section is herein presented for simulation.

The heat transfer between the sodium and the mercury is based on the difference between the average sodium temperature of the boiling section and the mercury temperature at the superheater end of the same section. The heat transfer coefficient is also a function of this temperature difference. The length of the section is established by the heat transfer coefficient and temperature difference between sodium and mercury.

The effect of the boiler walls is accounted for by combining the sodium and walls to form an equivalent heat capacitance. Heat energy transferred into the mercury section results in a state change or a time rate of change in the temperature of enclosed

BLOCK DIAGRAM - REACTOR THERMODYNAMICS

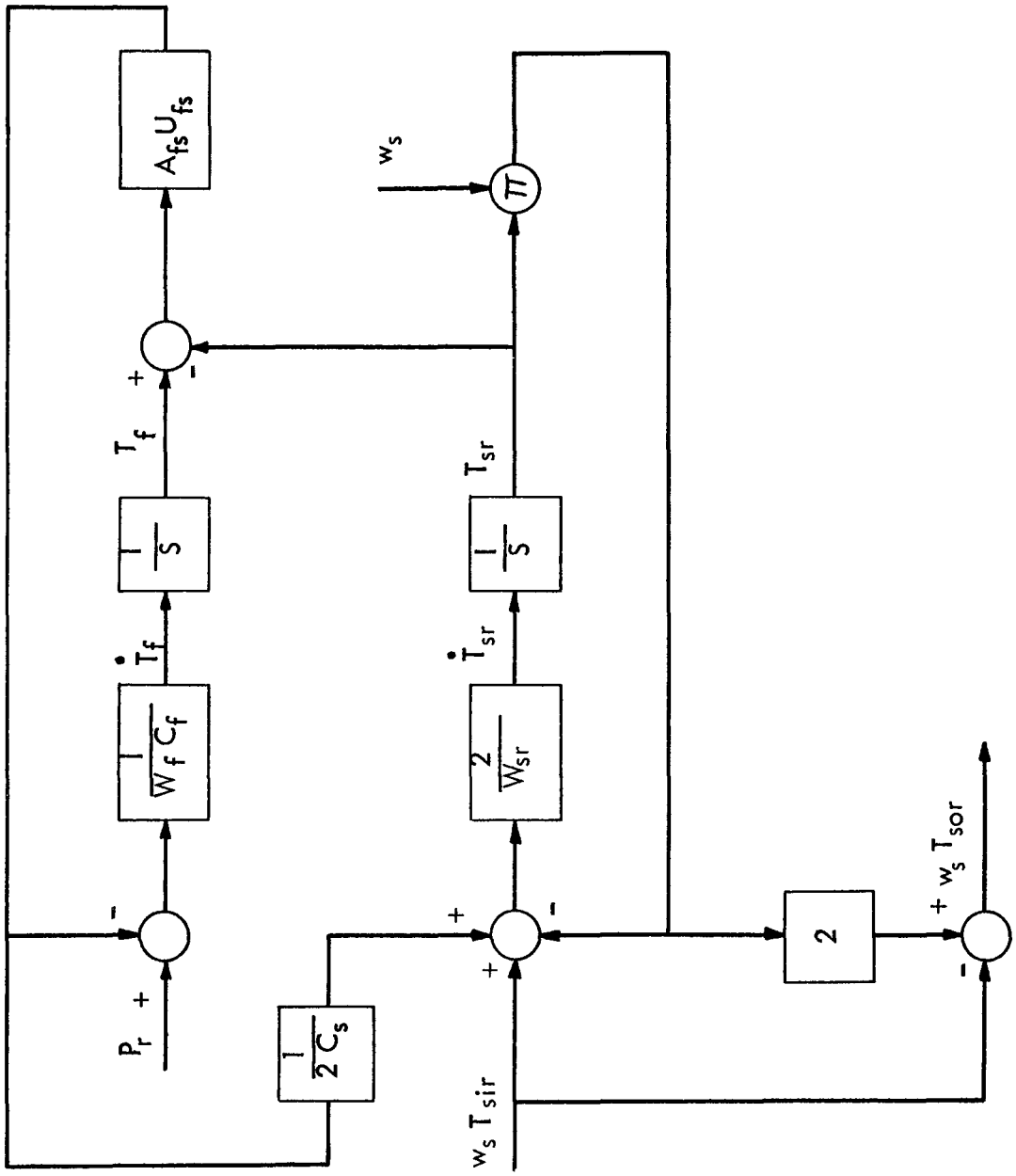

FIGURE 3

COMPUTER DIAGRAM - REACTOR

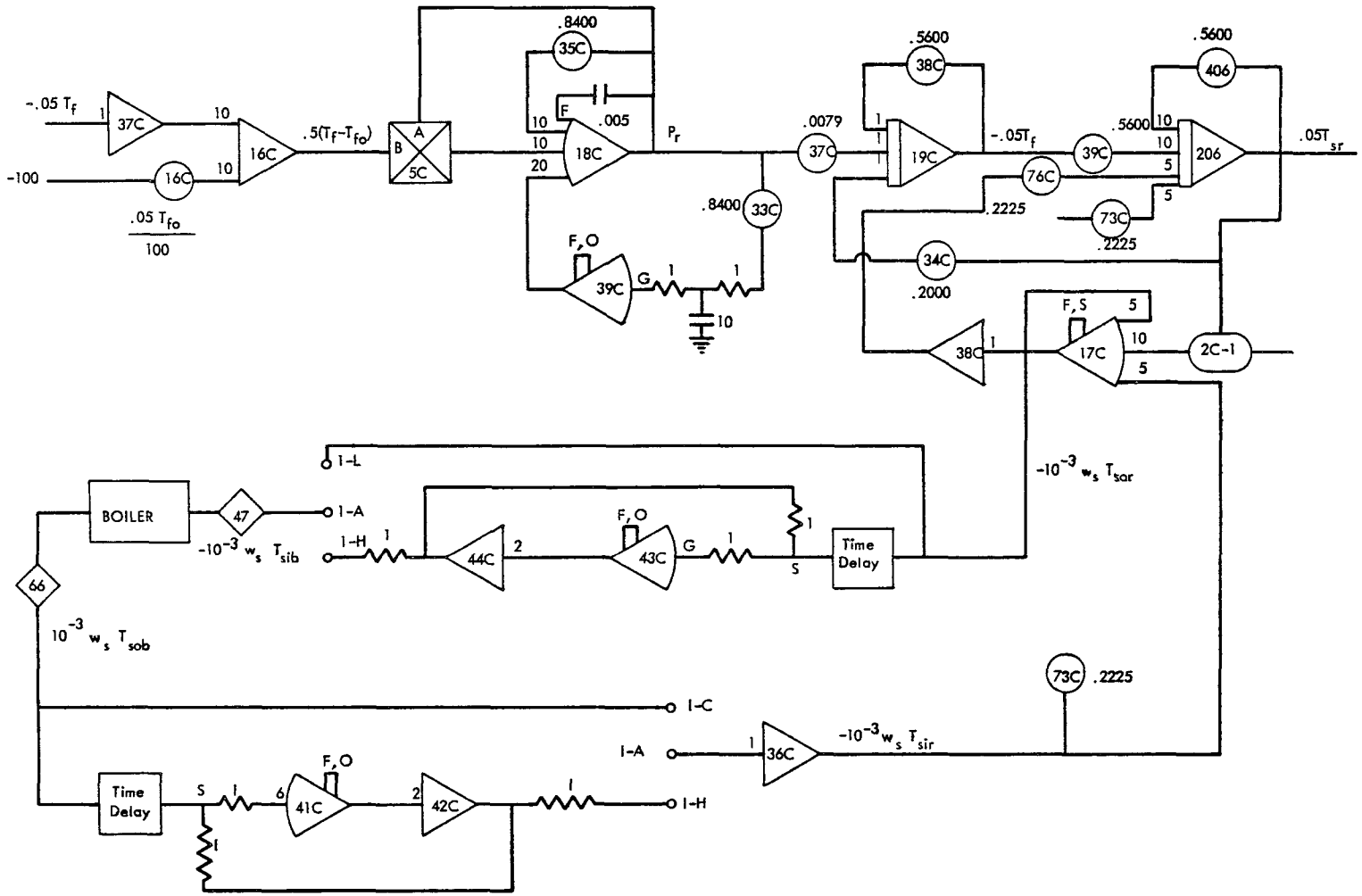

PREHEATER EQUATIONS

(6) $$w_s C_s T_{s_{32}} - w_s C_s T_{sob} = A_2 U_2 (T_{s_2} - T_{m_2}) + W_{s_2} C_{s_2} \frac{d T_{s_2}}{dt}$$

(7) $$W_{s_2} C_{s_2} = \frac{V_{s_2}}{V_s} W_w C_w + W_s C_s$$

(8) $$T_{s_2} = \frac{T_{s_{32}} + T_{sob}}{2}$$

(9) $$V_{s_2} = A_2 \frac{V_s}{A_t}$$

(10) $$w_2 C_m T_{m_{23}} - w_a C_m T_{mib} = A_2 U_2 (T_{s_2} - T_{m_2}) - W_{m_2} C_m \frac{d T_{m_2}}{dt}$$

(11) $$W_{m_2} = \frac{w_a - w_2}{S}$$

(12) $$A_2 = \frac{W_{m_2} A_t}{\rho_m V_{mt}}$$

(13) $$T_{m_{23}} = f P_{m23}$$

(14) $$T_{m_2} = \frac{w_2 T_{m_{23}} + w_a T_{mib}}{w_2 + w_a}$$

BLOCK DIAGRAM - PREHEATER

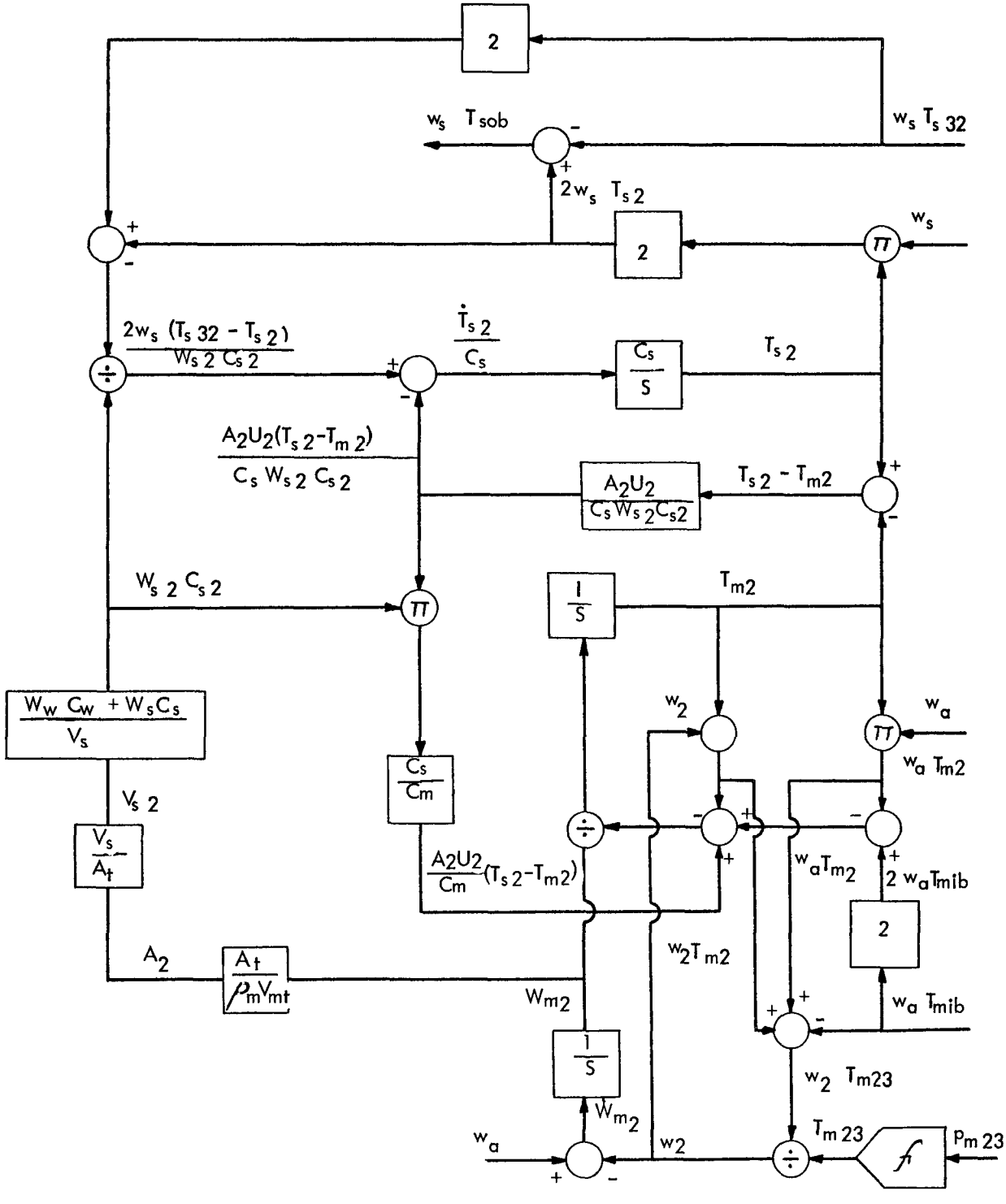

FIGURE 5

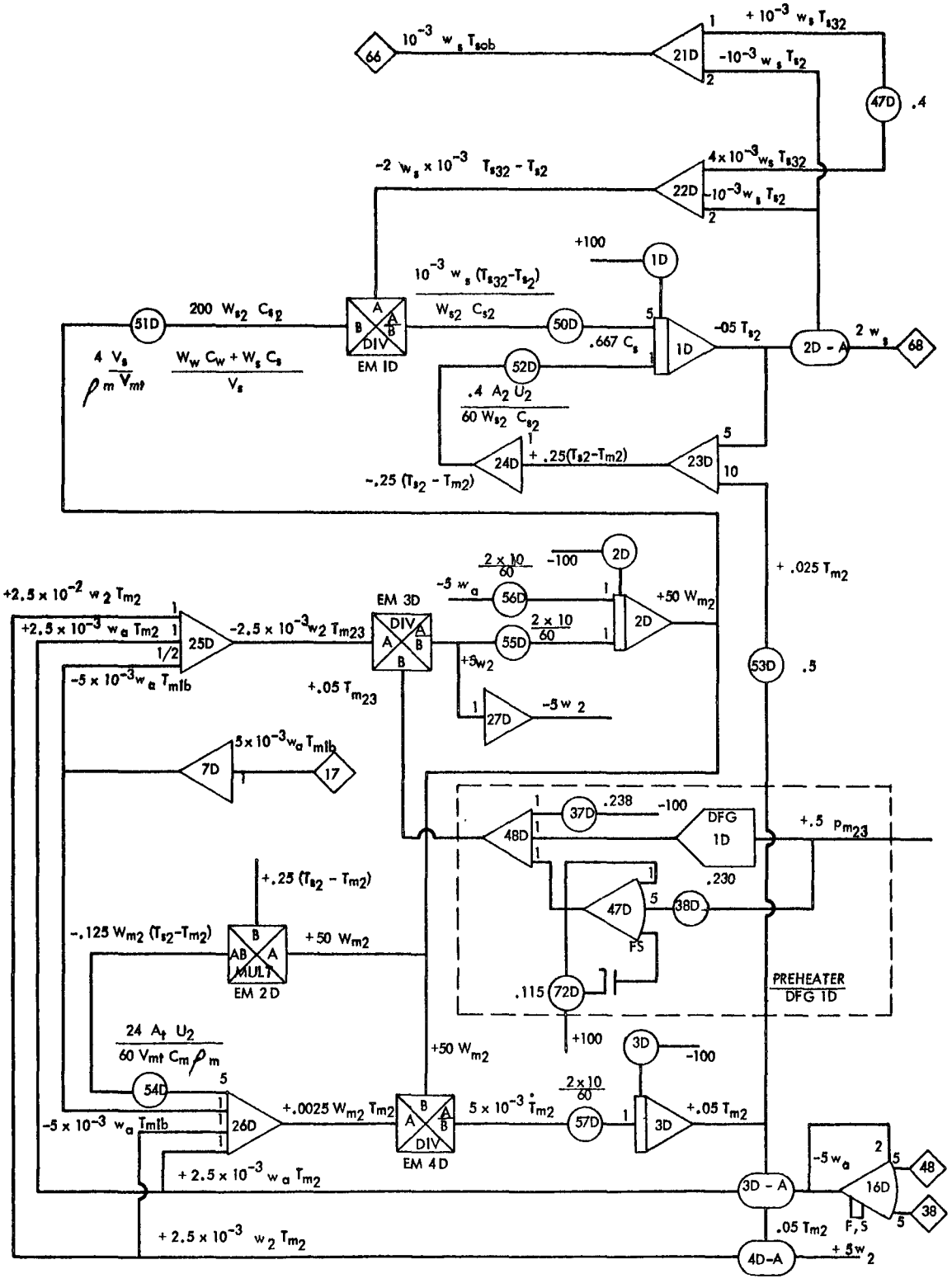

COMPUTER DIAGRAM–PREHEATER

FIG. 7 PREHEATER DFG 1-D
PRESSURE - TEMPERATURE RELATIONSHIP FOR
SATURATED MERCURY LIQUID

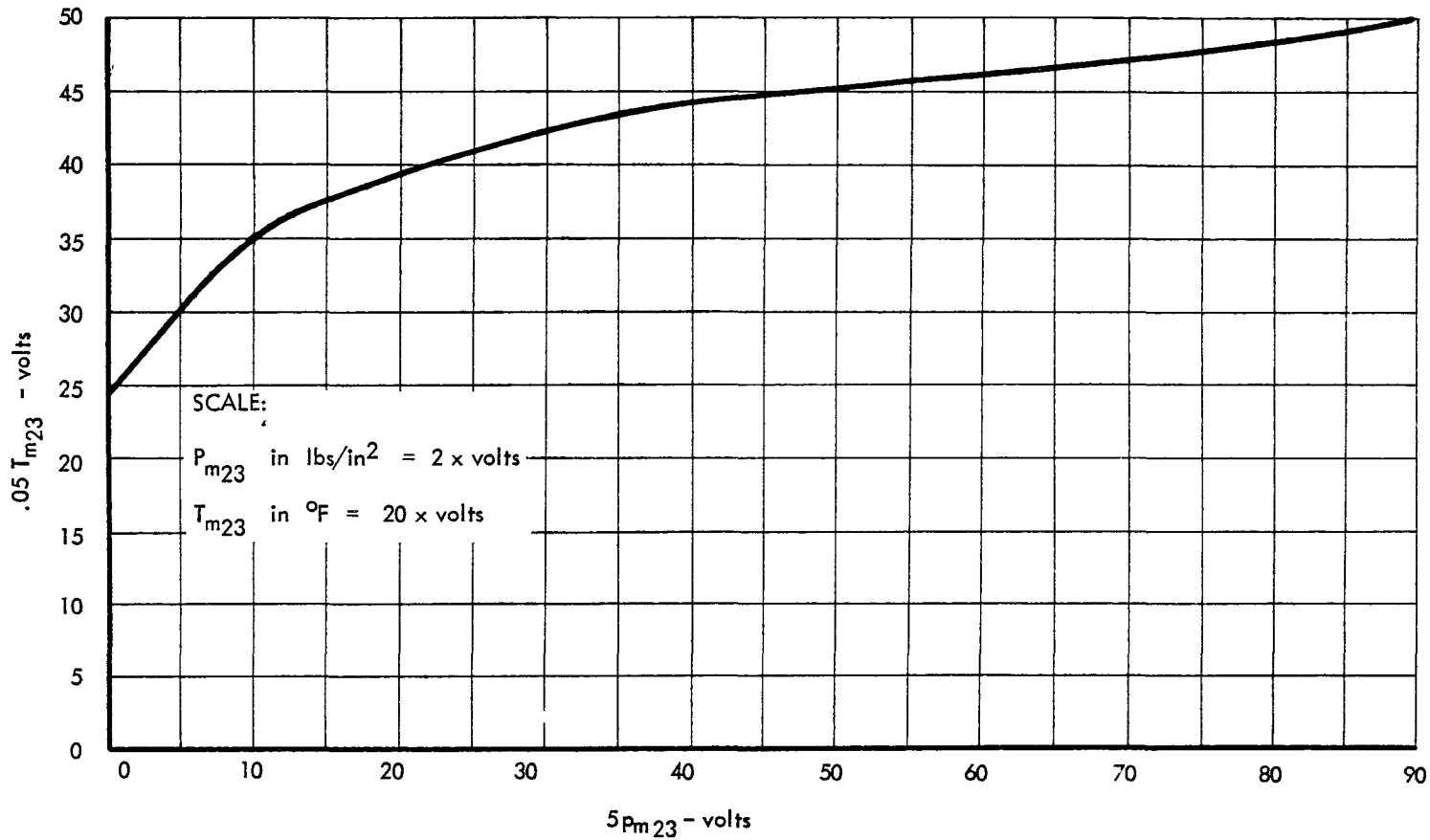

FIGURE 7

mercury. Since the mercury is boiling, the differential of temperature will be proportional to the time rate of change of pressure. The remainder of the heat input results in the state change from liquid to vapor.

Equations (15) to (25) describe the boiling section. Block diagram and computer diagram are shown in Figures 8 and 9. The simulation curves, describing the heat transfer coefficient and pressure-temperature relationship are presented in Figures 10 and 11.

The superheater consists of that section of the boiler not associated with preheating or boiling. Superheated vapor flows into the turbine at a rate determined by the pressure and temperature at the exit of the heat exchanger. A very small pressure drop is associated with flow in the region where quality is 100 percent, so vapor pressure within the superheater is considered uniform. The heat balance equation considers the input from the last section of the boiler and that from the associated sodium loop. Weight flow through the superheater is that taken by the turbine. The equations (26) through (37) are listed and the block diagram and computer diagram are shown in Figures 12 and 13.

C. Turbine

A two stage axial flow impulse turbine is used to convert the available energy of the mercury vapor into rotating mechanical energy. The entrance conditions to the turbine are dictated by the performance of the heat exchanger section. It is assumed that no pressure drop occurs between the superheater exit and the turbine entrance.

For simulation purposes, turbine performance may be considered as governed by entrance conditions and speed-efficiency characteristics. Mathematically, this results in turbine discharge conditions being dependent variables relative to the turbine but does not alter the true inter-dependency of variables in the overall system. Equations (38) through (43) and Figures 14 through 19 describe the turbine.

D. Condenser-Radiator

Mercury vapor flows from the turbine into the condenser, where it is reduced to a liquid state. The condenser is defined as that portion of the radiator assembly which contains mercury in the vapor state as opposed to the intercooler-subcooler which comprises that portion of the radiator containing mercury in the liquid state. Heat input to the condenser is determined by the turbine weight flow and its exit enthalpy. Heat of condensation is rejected, through the walls and fins by radiation at a rate proportional to the effective condenser area and the Stefan-Boltzmann temperature relationship. Heat also leaves the condenser in the form of saturated liquid into the intercooler.

The volume of the condenser plus the volume of the intercooler is a constant. However, unbalanced heat flow encountered during transient operation may cause the respective volumes, and, therefore, inventories to vary. Rate of condensation and

BOILING SECTION EQUATIONS

(15) $$w_s C_s T_{s43} - w_s C_s T_{s32} = A_3 U_3 (T_{s3} - T_{h34}) + W_{s3} C_{s3} \frac{d T_{s3}}{dt} + P_l$$

(16) $$W_{s3} C_{s3} = \frac{V_{s3}}{V_s} \left[W_w C_w + W_s C_s \right]$$

(17) $$T_{s3} = \frac{T_{s43} + T_{s32}}{2}$$

(18) $$V_{s3} = \frac{V_s}{A_t} A_3$$

(19) $$U_3 = f (T_{s3} - T_{m34})$$

(20) $$w_3 h_g - w_2 C_m T_{m23} = A_3 U_3 (T_{s3} - T_{m34}) - W_{m3} C_m \frac{d T_{m34}}{dt} - h_{fg} (w_2 - w_3)$$

(21) $$W_{m3} = \frac{w_2 - w_3}{S}$$

(22) $$T_{m34} = f (p_{m34})$$

(23) $$h_g = \text{constant}$$

(24) $$l_3 = \frac{A_3}{\pi d}$$

(25) $$p_{m23} - p_{m34} = \left(\frac{w_2 + w_3}{2 A_{bc}} \right)^2 \frac{1}{g} \left[v_{fg} + K_v l_3 \left(v_f + v_{fg} \right) \right]$$

BLOCK DIAGRAM - BOILING SECTION

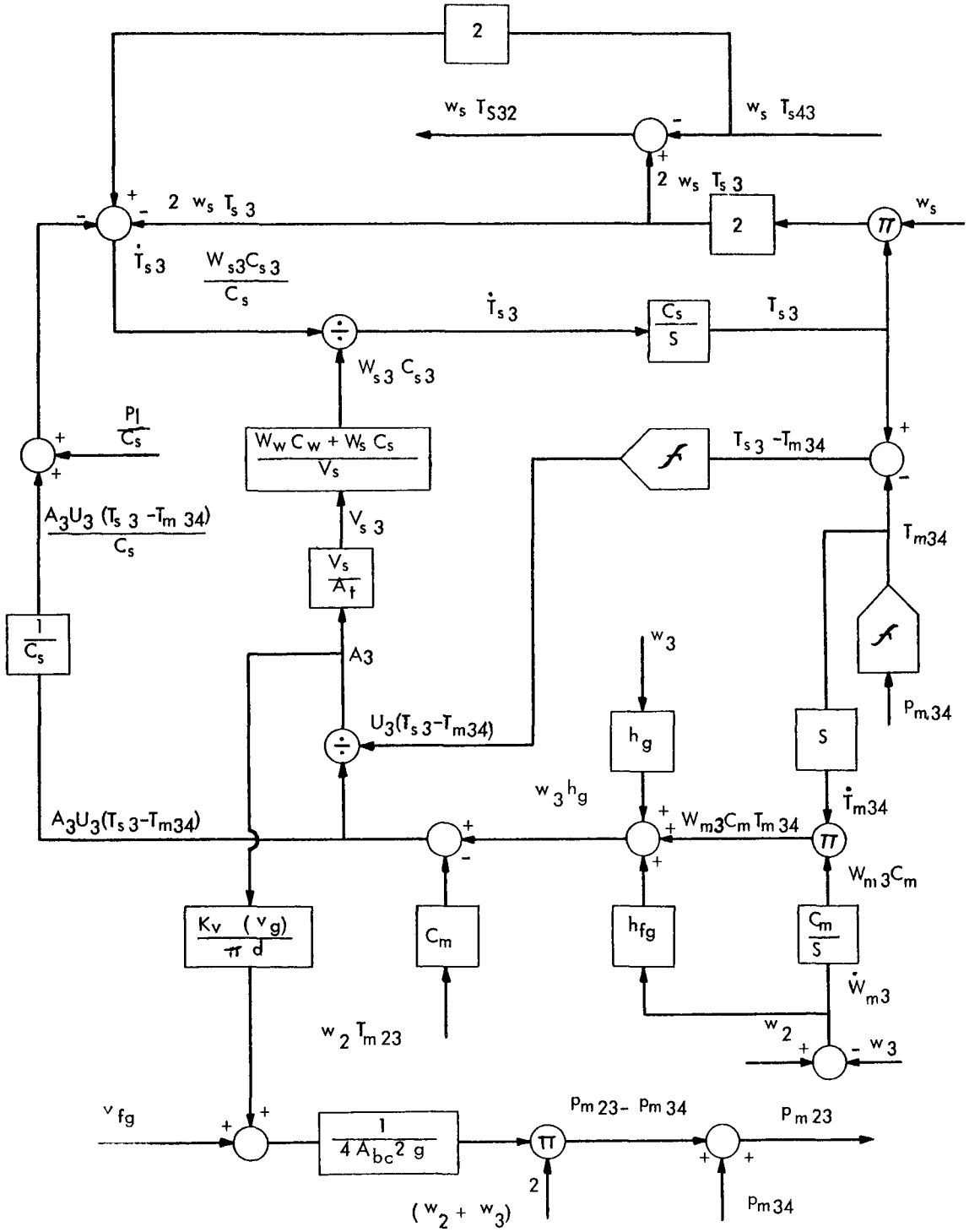

FIGURE 8

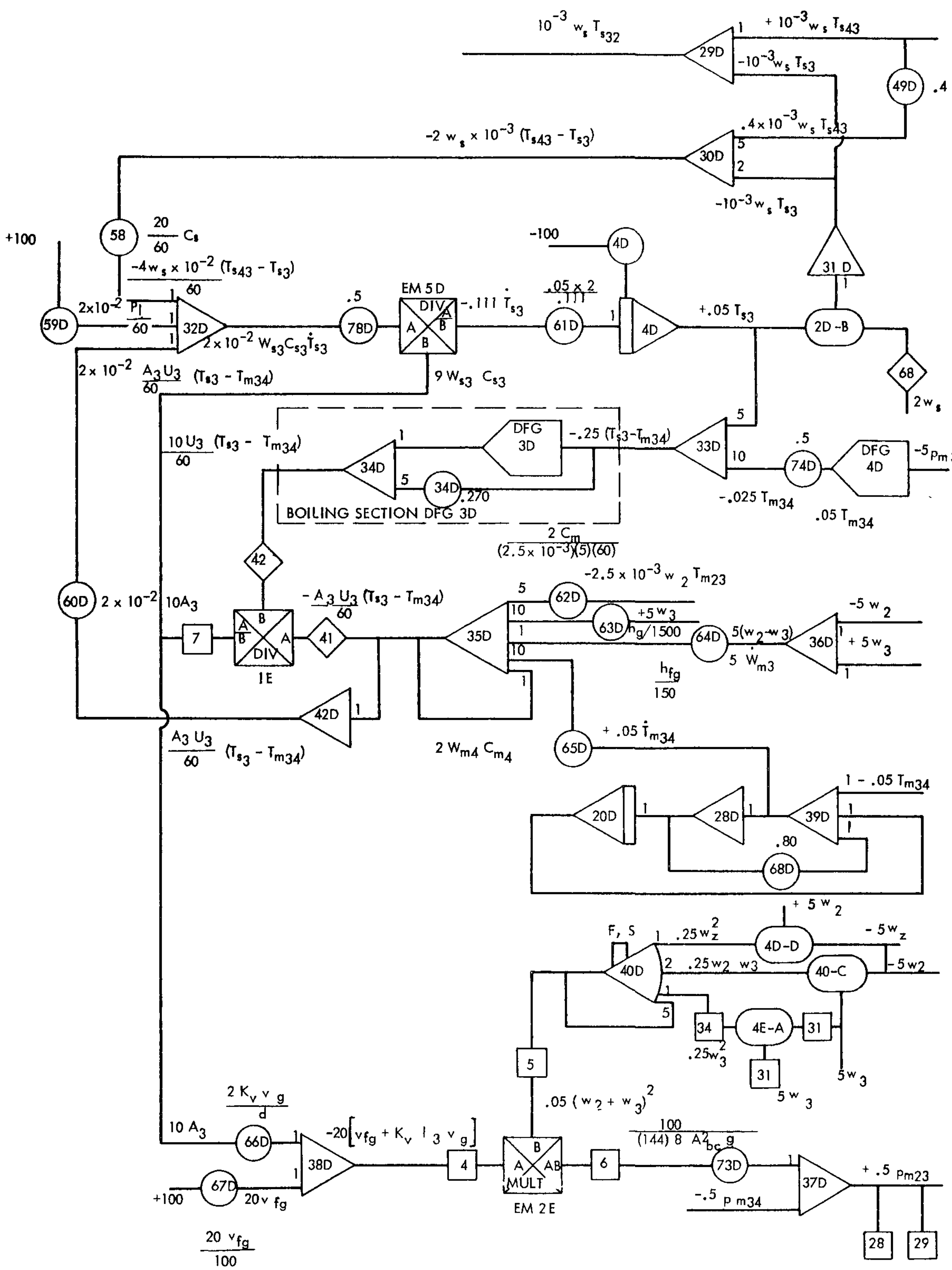

COMPUTER DIAGRAM - BOILING SECTION

FIG. 10 BOILING SECTION DFG 3D

HEAT TRANSFER - TEMPERATURE RELATIONSHIP IN BOILING SECTION

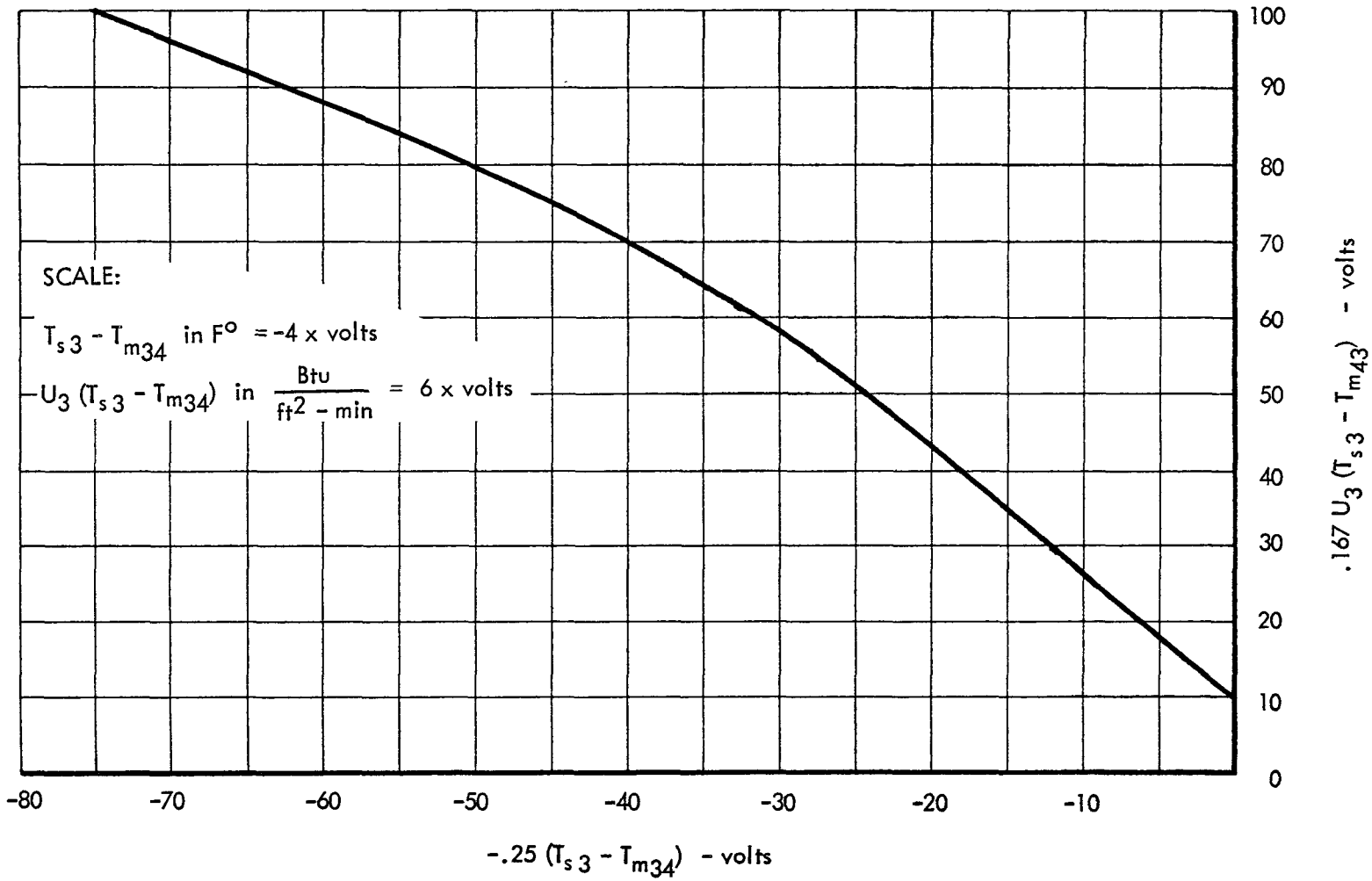

PRESSURE - TEMPERATURE RELATIONSHIP FOR SATURATED MERCURY VAPOR

FIG. 11 BOILING SECTION DFG 4D

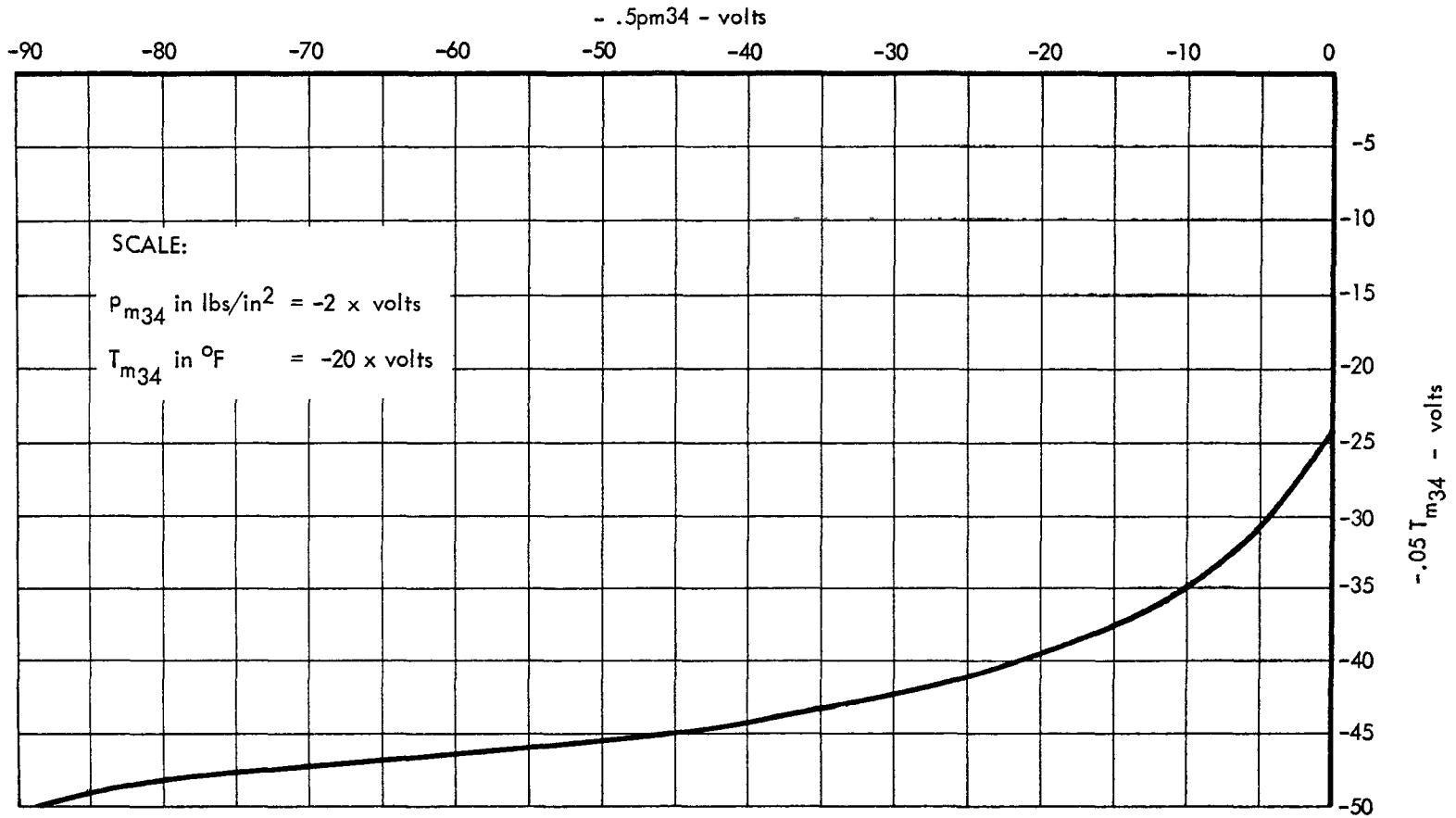

SUPERHEATER EQUATIONS

(26) $$w_s C_s T_{sir} - w_s C_s T_{s43} = A_4 U_4 (T_{s_4} - T_{m_4}) + W_{s4} C_{s4} \frac{d T_{s4}}{dt}$$

(27) $$W_{s4} C_{s4} = \frac{V_{s4}}{V_s} \left[W_w C_w + W_s C_s \right]$$

(28) $$T_{s_4} = \frac{T_{sib} + T_{s43}}{2}$$

(29) $$V_{s4} = A_4 \frac{V_s}{A_t}$$

(30) $$A_4 = A_t - A_2 - A_3$$

(31) $$w_4 C_{m_4} T_{mbt} - w_3 C_{m_4} T_{m34} = A_4 U_4 (T_{s_4} - T_{m_4}) - W_{m4} C_{m4} \frac{d T_{m4}}{dt}$$

(32) $$W_{m_4} = \frac{V_m \rho_{m4}}{A_t} A_4$$

(33) $$w_3 = \frac{d W_{m4}}{dt} + w_4$$

(34) $$p_{m4} = \rho_{m4} R (T_{m_4} + 460)$$

(35) $$p_{m_4} = p_{m34}$$

(36) $$w_4 = w_t$$

(37) $$T_{m_4} = \frac{w_4 T_{mbt} + w_3 T_{m34}}{w_3 + w_4}$$

BLOCK DIAGRAM - SUPERHEATER

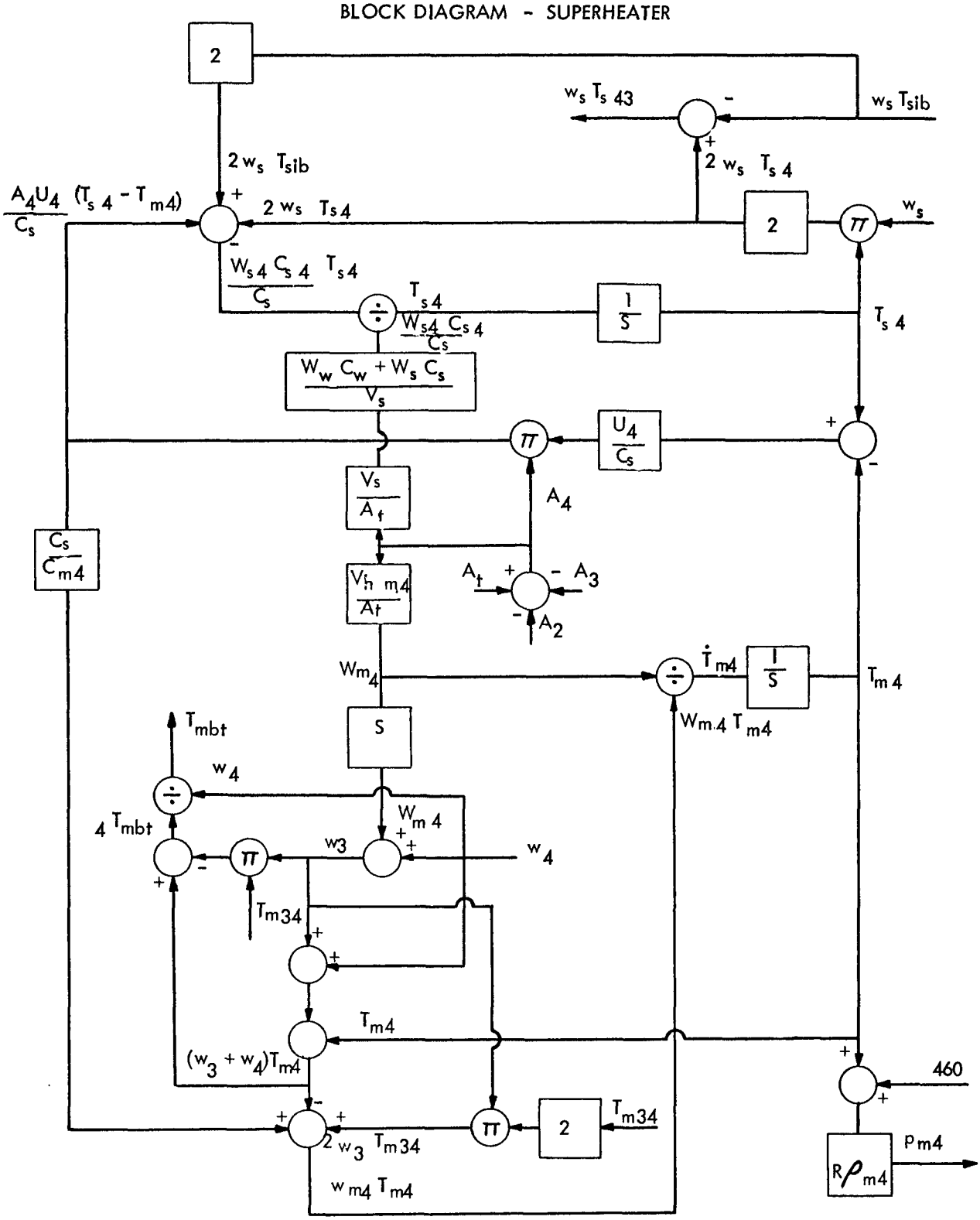

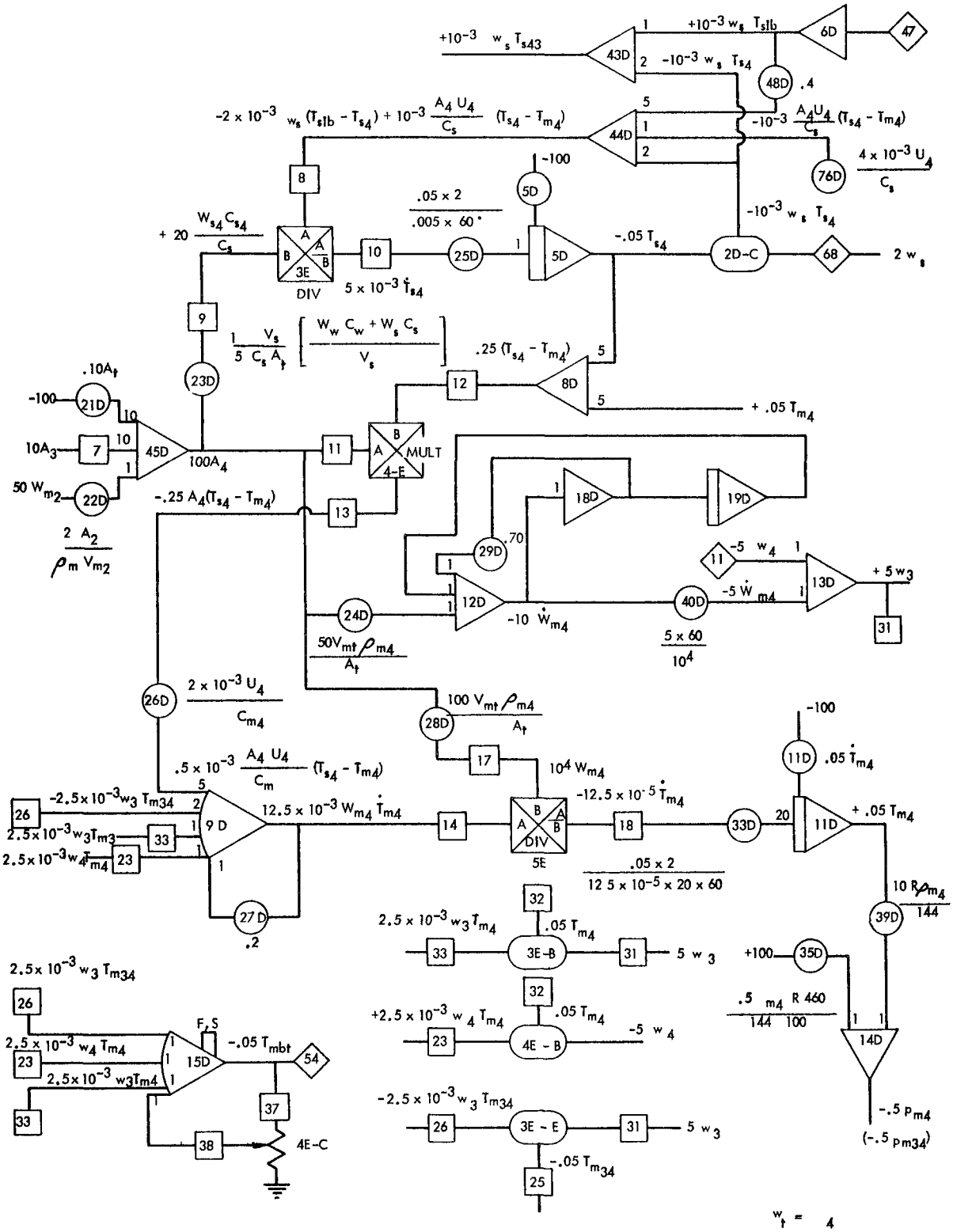

COMPUTER DIAGRAM - SUPERHEATER

TURBINE EQUATIONS

(38) $P_t = K_{t3} \; w_t \; \eta \; \Delta h_t$

(39) $\eta \, \Delta h_t = f(N, R)$

(40) $\eta = f(\nu)$

(41) $\nu = \dfrac{K_{t1} \; N}{\sqrt{R \, \Delta h_t}}$

(42) $h_i = f(T_{mbt})$

(43) $h_t = h_i - \nu \, \Delta h_t$

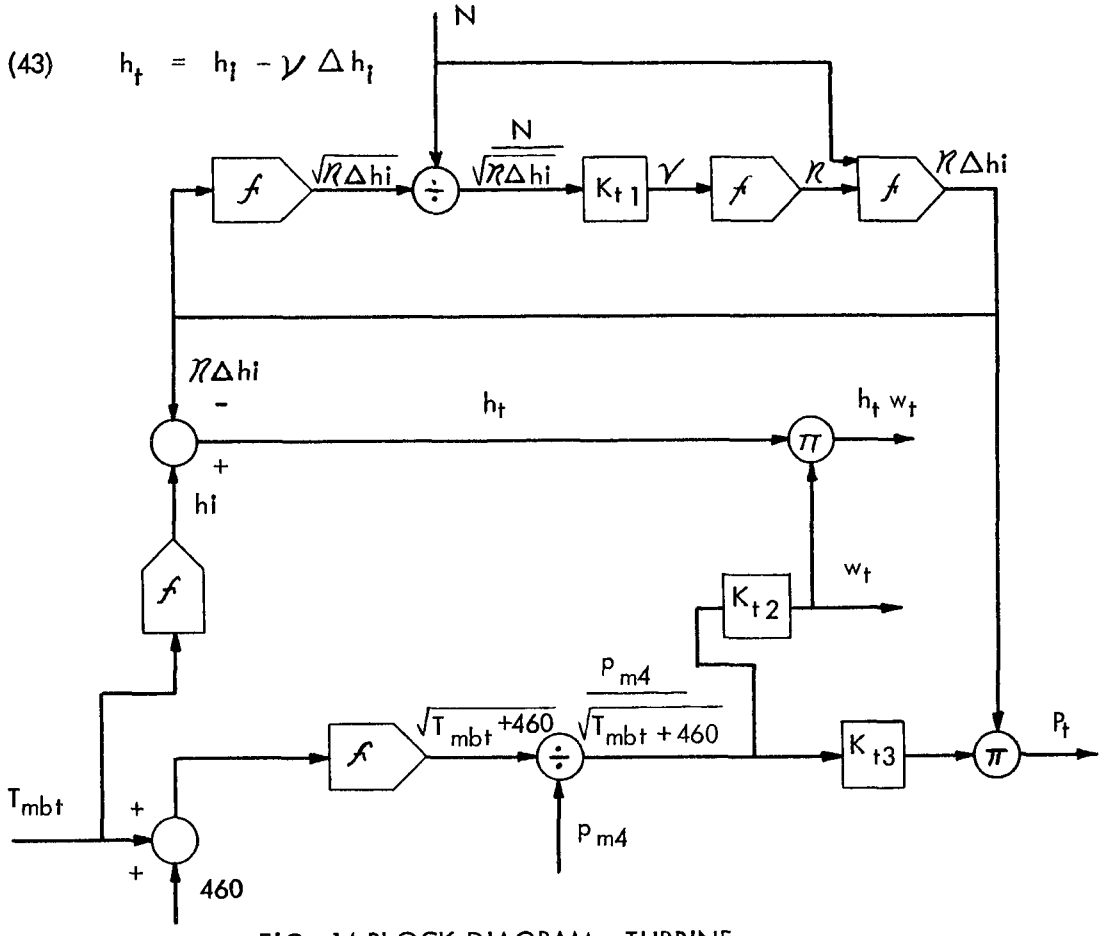

FIG. 14 BLOCK DIAGRAM - TURBINE

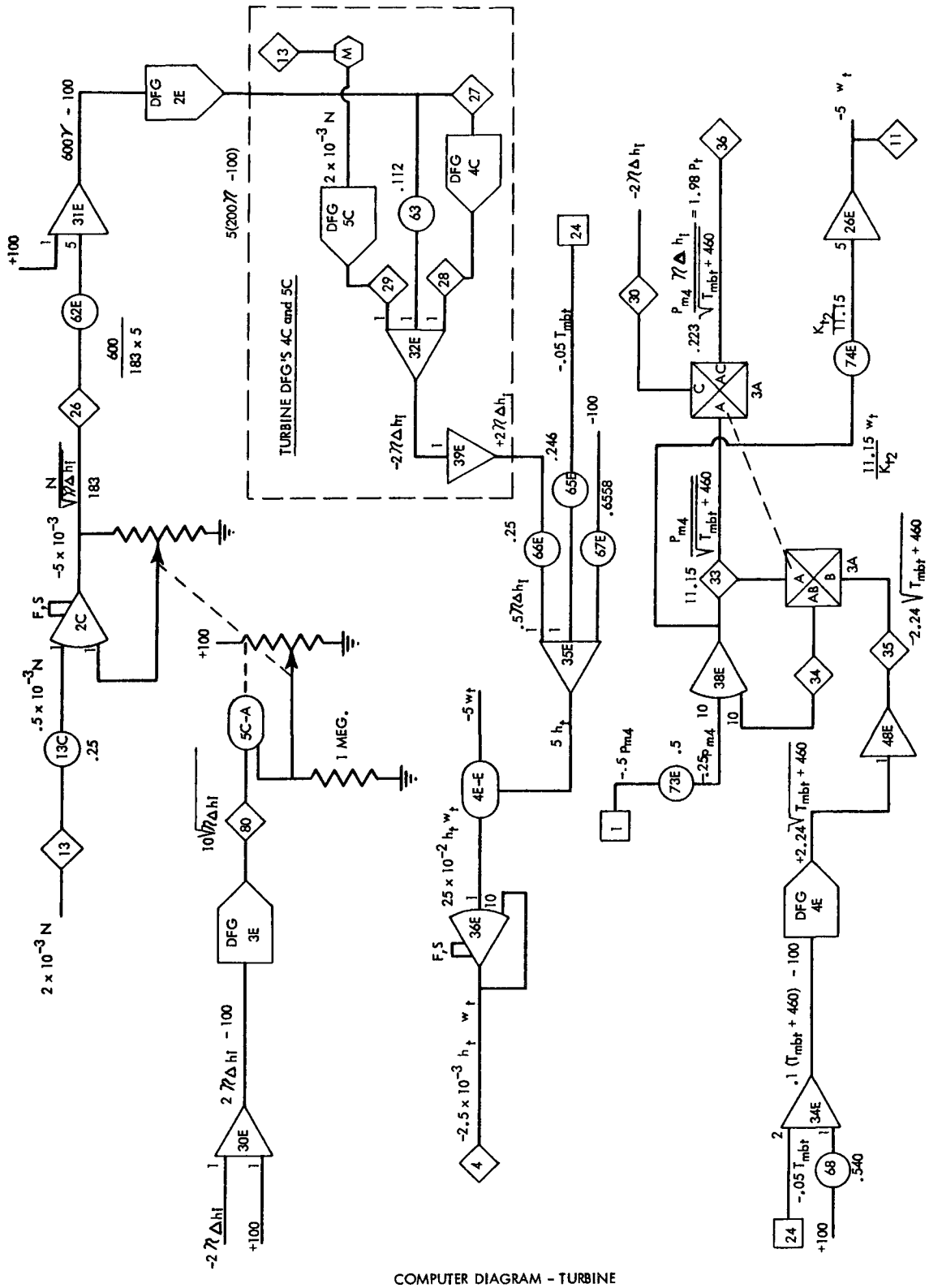

COMPUTER DIAGRAM - TURBINE

TURBINE DFG 2E

TURBINE SPEED RATIO-EFFICIENCY RELATIONSHIP

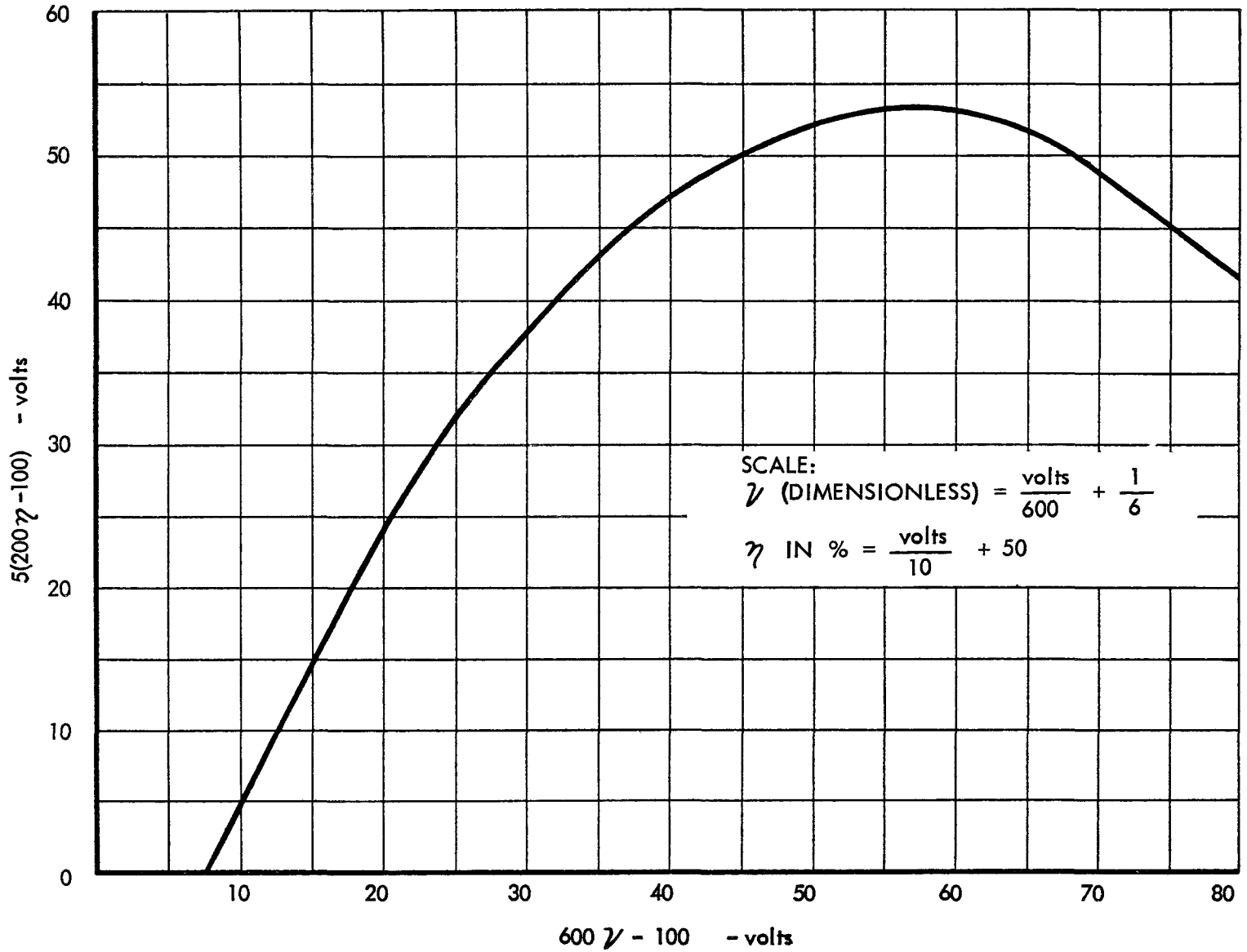

FIGURE 16

FIG. 17 TURBINE DFG'S 4C and 5C
TURBINE EFFICIENCY - IDEAL ENTHALPY RELATIONSHIP
WITH LINES OF CONSTANT SPEED

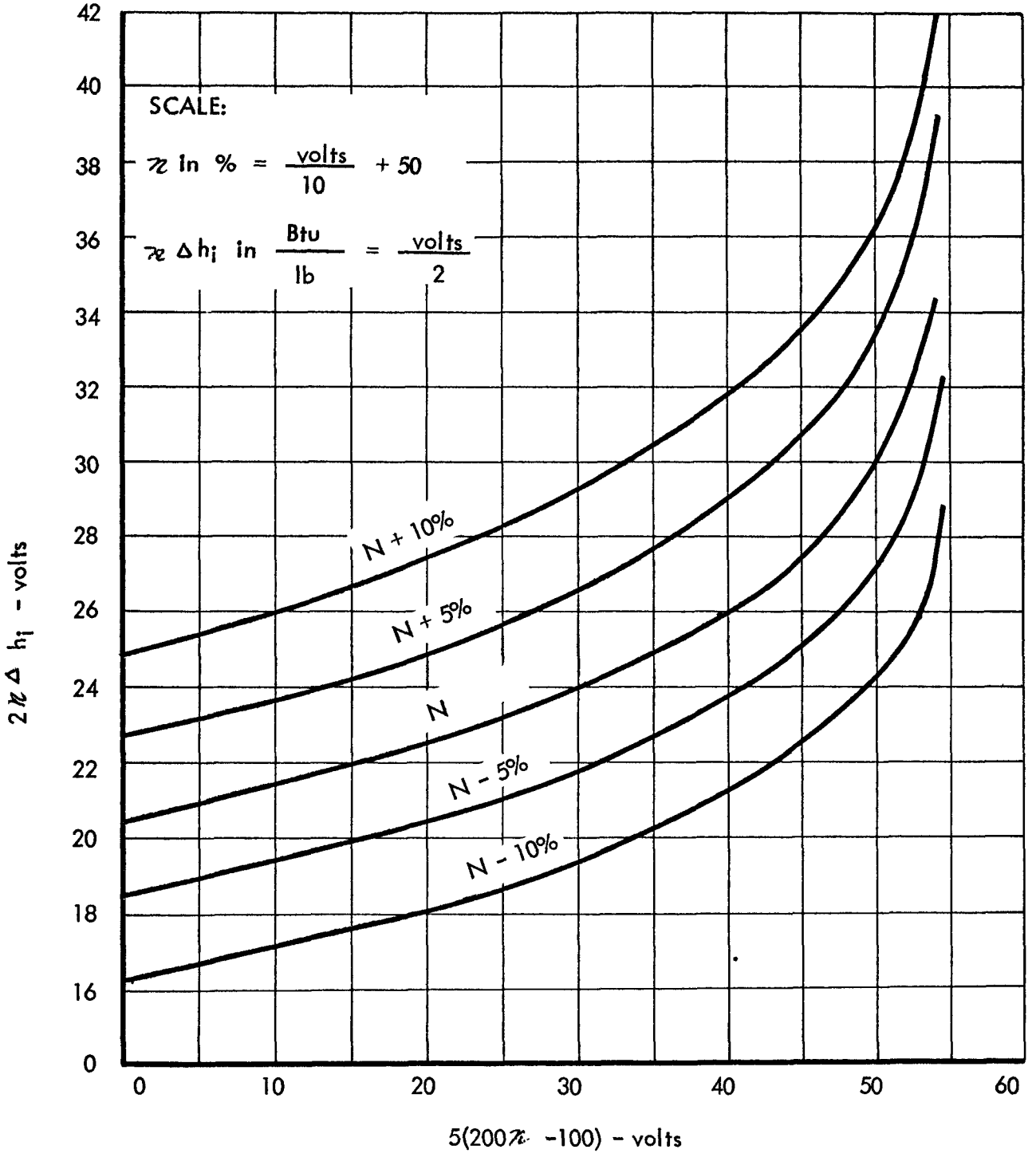

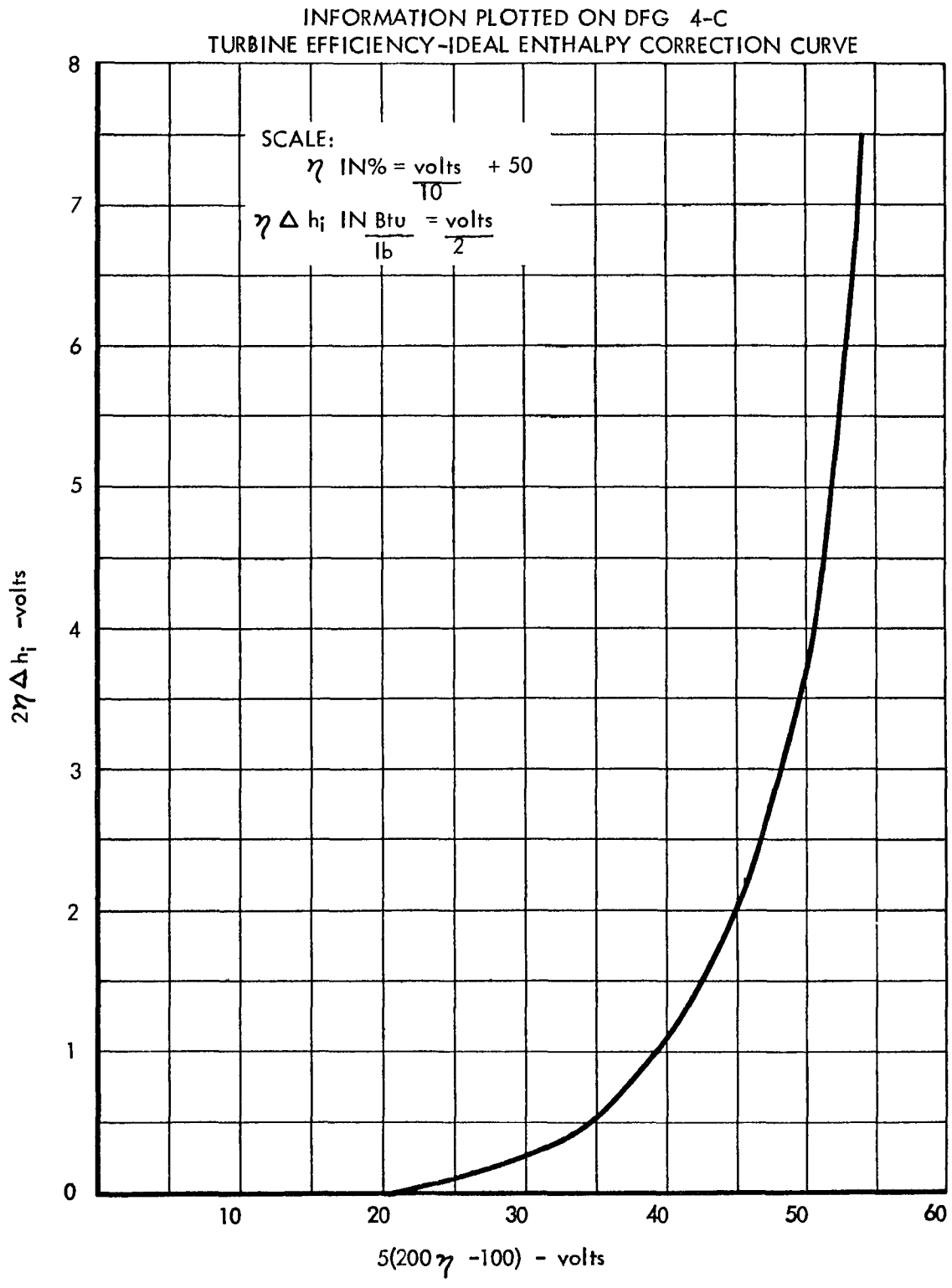
INFORMATION PLOTTED ON DFG 4-C
TURBINE EFFICIENCY-IDEAL ENTHALPY CORRECTION CURVE
SCALE:
η IN% = volts/10 + 50
η Δ hi IN Btu/lb = volts/2
2η Δ hi -volts
0
1
2
3
4
5
6
7
8
10
20
30
40
50
60
5(200η -100) - volts

FIGURE 18

INFORMATION PLOTTED ON DFG 5-C

SPEED CORRECTION CURVE FOR FIGURE 17

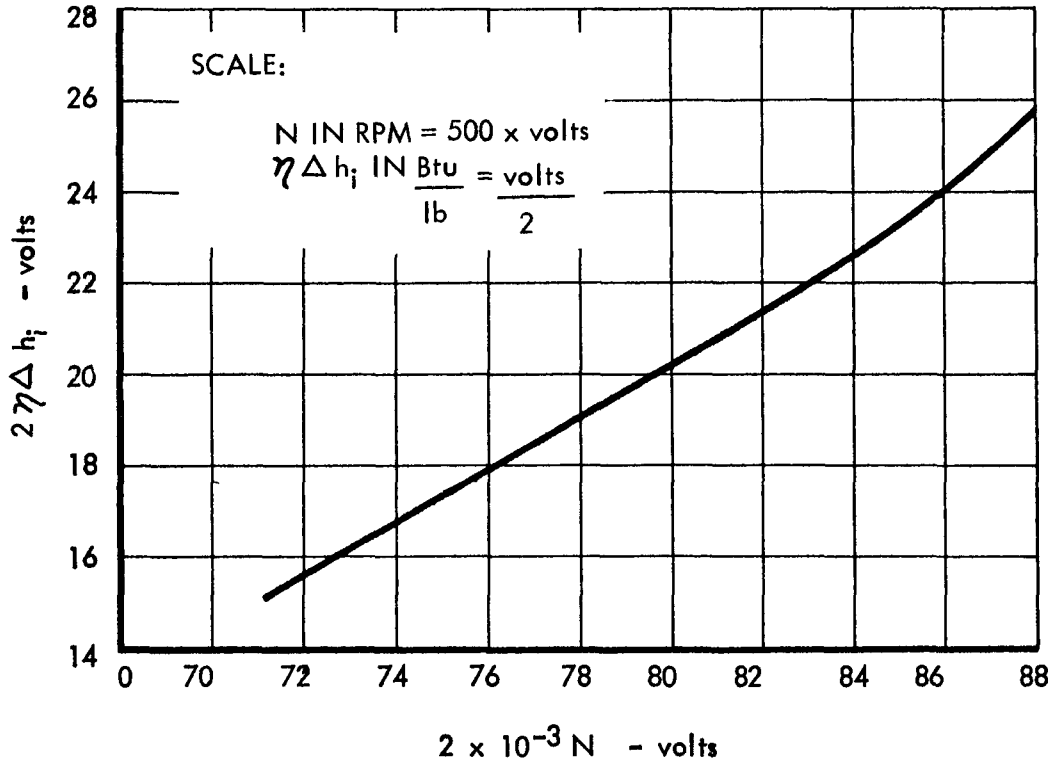

FIGURE 19

condensing temperature are the two variables that change to account for the difference within the condenser portion.

Equations (44) through (52) describe the performance of the condenser. The block diagram and computer diagram are shown in Figures 20 and 21. The temperature and specific weight relationships used in the condenser simulation are shown in Figures 22 and 23.

E. Intercooler-Radiator

The intercooler consists of that portion of the radiator which is occupied with liquid mercury. The rate of mercury entering the intercooler is determined by the vapor condensation in the condenser and the moisture flow from the turbine. Due to continued radiation, the mercury traveling through the intercooler will exit as a subcooled liquid. The rate of which this mercury is drawn from the intercooler is that amount which when added to the bearing flow will be the quantity needed by the pump in order to satisfy system requirements.

During system transient performance, the mercury inventory and hence the area of the intercooler will fluctuate, thus accounting for changes in the average intercooler temperature. This change in inventory will also change the effective heat capacitance of the intercooler. The equations describing intercooler action are (53) through (61). Figures 24 and 25 show the block diagram and computer diagram. Figure 26 shows the temperature relationship while 27 shows the effect of changing inventory on the area and heat capacitance.

At design conditions the system will be operating at the break point on this plot. This is caused by the physical design of the condenser and intercooler. The condenser is made up of vertical tubes placed around the circumference of the vehicle while the intercooler is an annular tube completely filled with liquid mercury at design conditions. As the mercury inventory in the intercooler changes, either rising up the vertical tubes or lowering in the annular ring, the weight to area relationships will change as shown in Figure 27.

F. Subcooler

Subcooler inlet flow is a mixture of the subcooled liquid from the intecooler plus bearing flow. Heat energy is radiated through the vehicle surface and temperature of the combined mass flow is reduced. The mercury and subcooler walls are assumed to be at the same temperature; the heat capacity of the subcooler is an effective value considering these two masses. Equations (62) through (65) describe the actions of the subcooler. The block diagram and computer diagram are shown in Figures 28 and 29.

CONDENSER EQUATIONS

(44) $T_c = T_{mc}$

(45) $h_t\ w_t - w_2 C_m T_c - A_c E_{ff}\ e \left[\sigma (T_c + 460)^4 - P_l\right] = W_c C_c \frac{dT_s}{dt} + h_{fg}(w_t - w_c)$

(46) $W_c C_c = V_c \left[\frac{W_{w2} C_{w2} + W_f C_f}{V_t}\right] + W_{mc} C_m$

(47) $A_c = A_{tr} - A_i$

(48) $W_{mc} = V_c \rho_{mc}$

(49) $\rho_{mc} = f(T_{mc})$

(50) $w_t - w_c = S\ W_{mc}$

(51) $p_c = \rho_{mc}\ R\ (T_c + 460)$

(52) $V_c = A_c \frac{V_c}{A_c}$

BLOCK DIAGRAM - CONDENSER

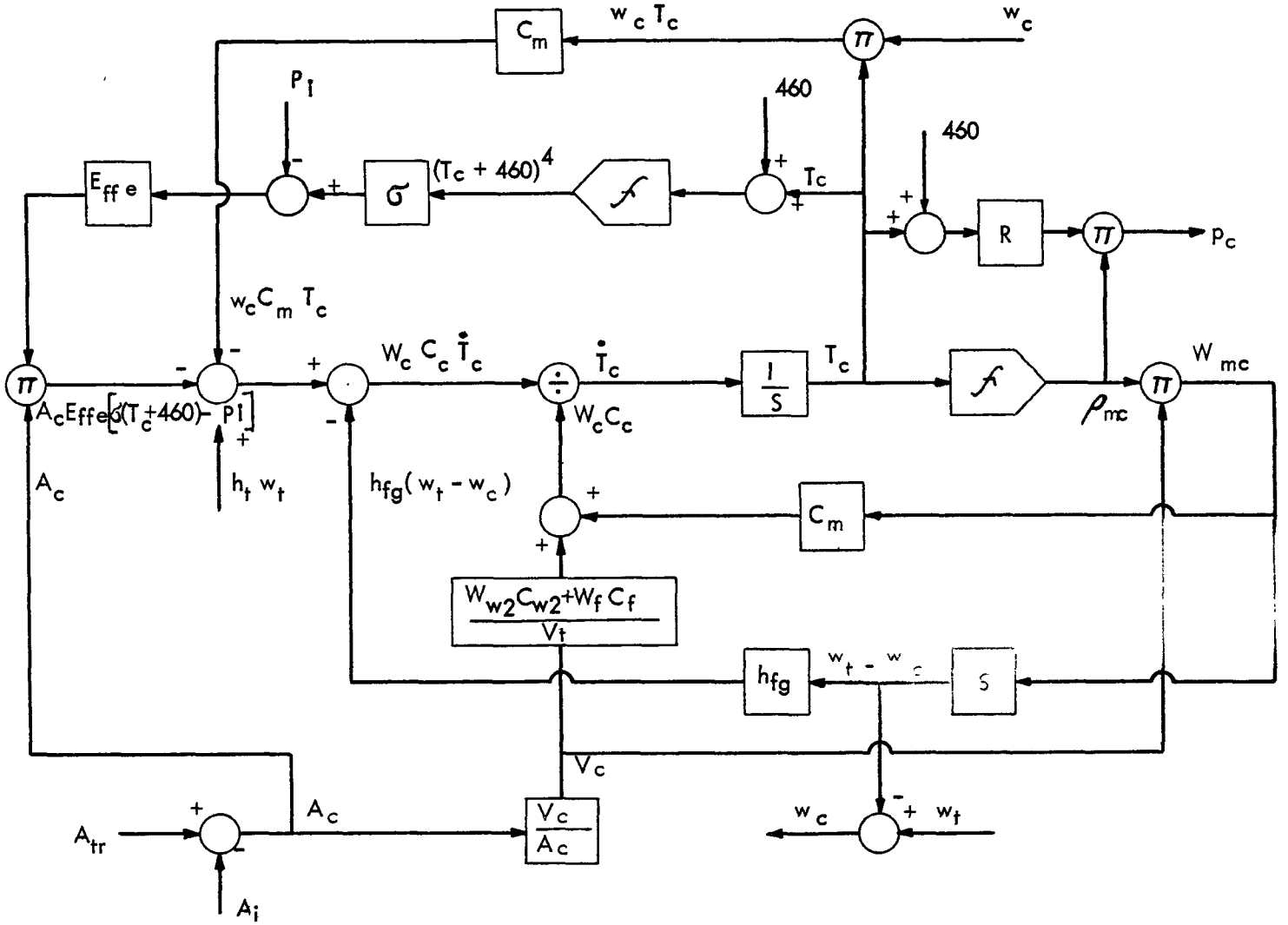

FIGURE 20

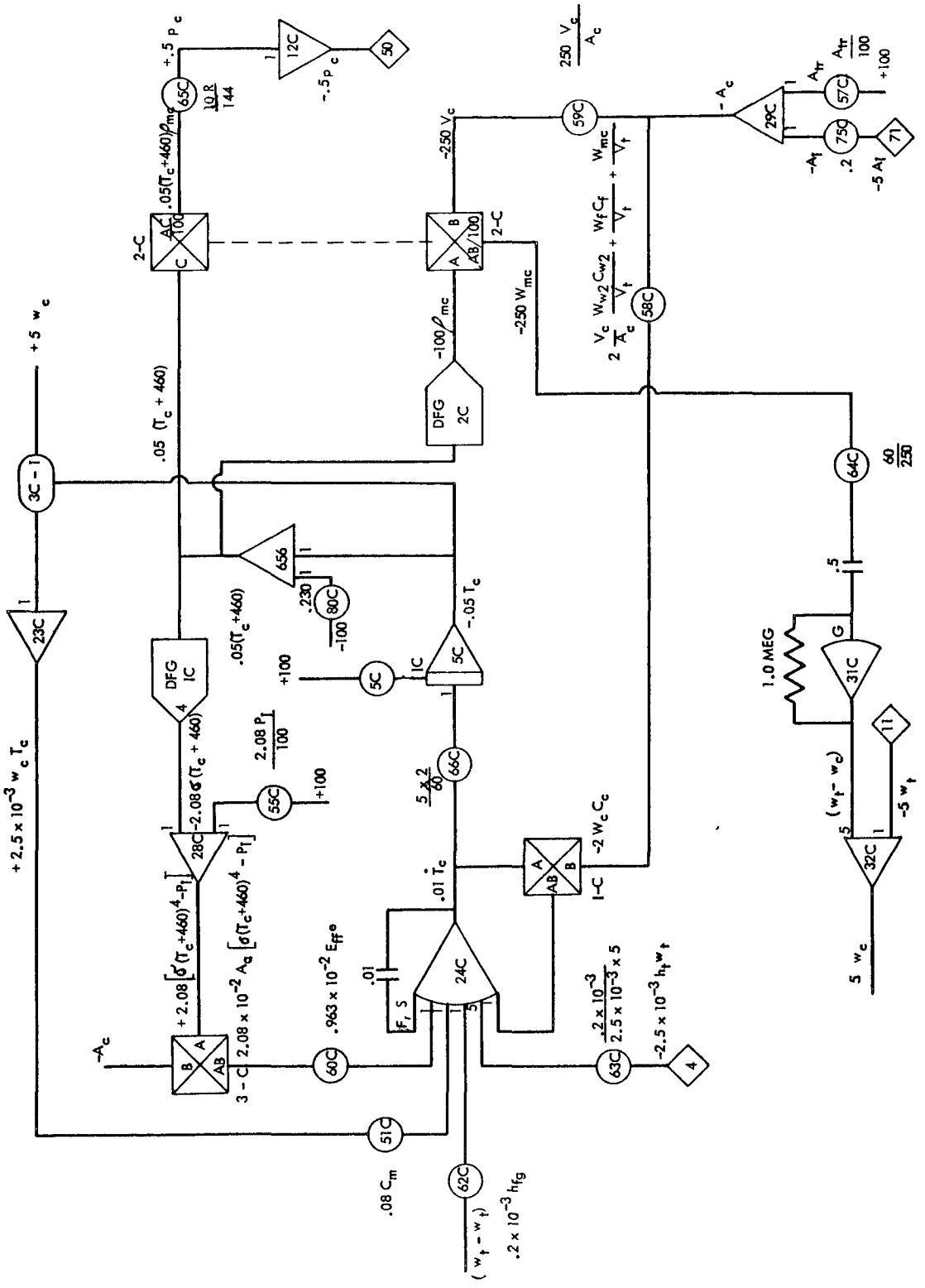

COMPUTER DIAGRAM - CONDENSER

STEFAN-BOLTZMANN-TEMPERATURE RELATIONSHIP

CONDENSER DFG 1C

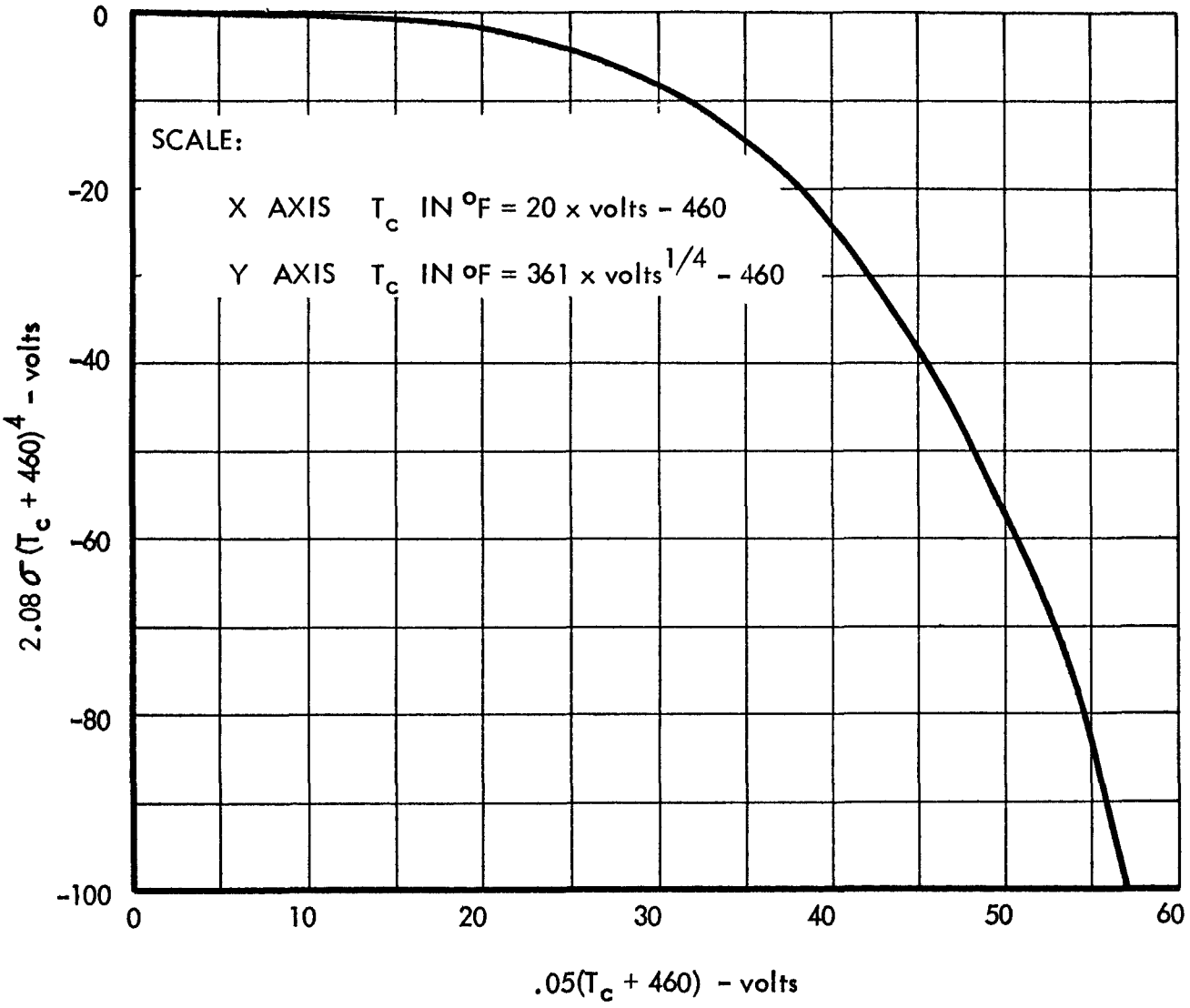

FIGURE 22

SPECIFIC WEIGHT-TEMPERATURE RELATIONSHIP FOR SATURATED MERCURY VAPOR

CONDENSER DFG 2C

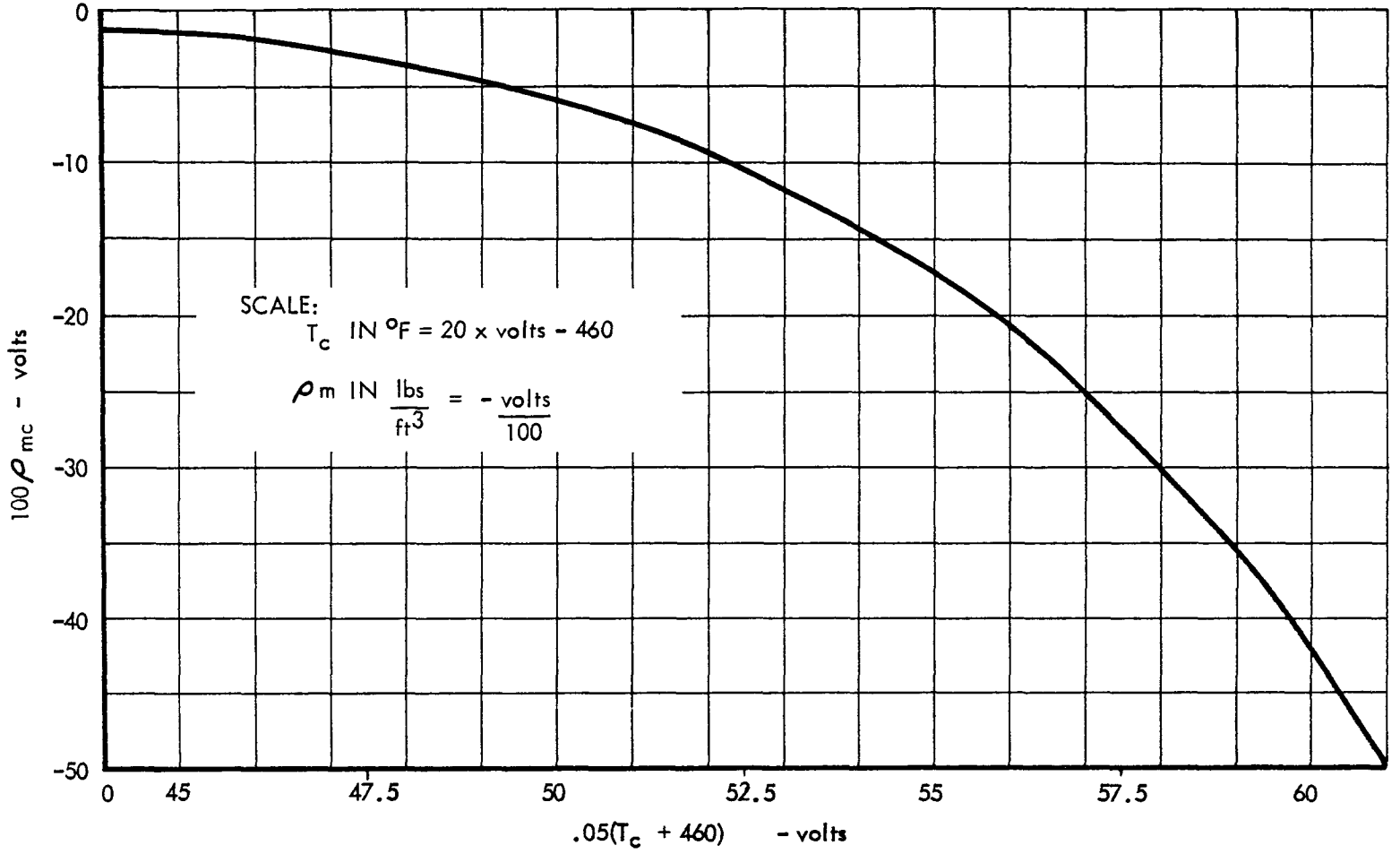

FIGURE 23

INTERCOOLER EQUATIONS

(53) $$T_{mi} = T_i$$

(54) $$W_{mi} = \frac{w_c - w_i}{S}$$

(55) $$V_i = \frac{W_{mi}}{\rho_m}$$

(56) $$A_i = f(W_{mi})$$

(57) $$w_c C_m T_{mc} - w_i C_m T_{mis} - A_i E_{ff} e \left[\sigma (T_{mi} + 460)^4 - P_i\right] = W_i C_i \frac{dT_i}{dt}$$

(58) $$W_i C_i = V_i \left[\frac{W_{w2} C_{w2} + W_f C_f + W_{mi} C_m}{V_t}\right]$$

(59) $$V_i \left[\frac{W_{w2} C_{w2} + W_f C_f + W_{mi} C_m}{V_t}\right] = f(A_i)$$

(60) $$T_{mis} = T_{mi} + (T_{mi} - T_{mc})$$

(61) $$w_i = w_a$$

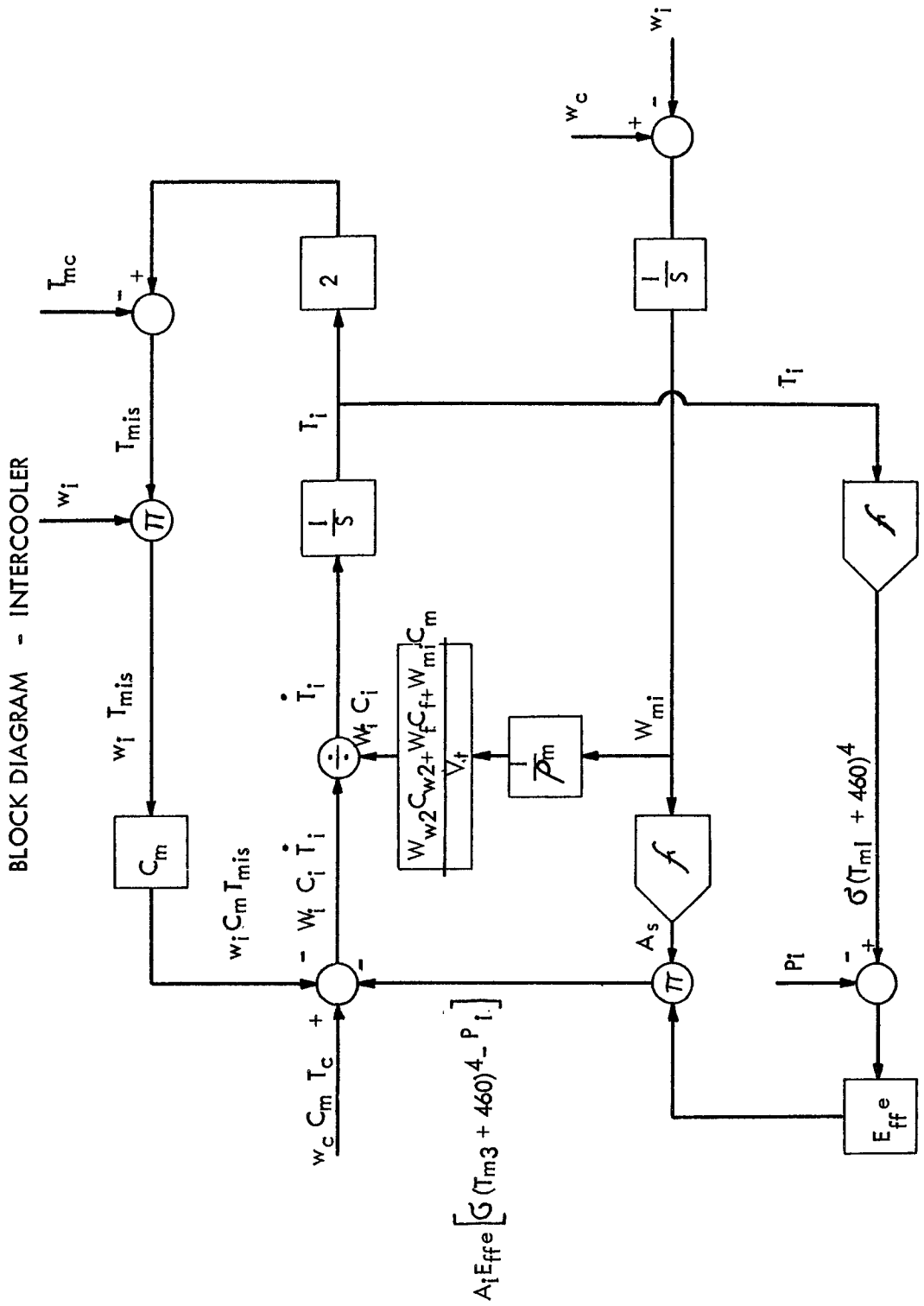
BLOCK DIAGRAM - INTERCOOLER
T_{mc}
T_{mis}
w_i
$w_i T_{mis}$
C_m
$w_i C_m T_{mis}$
$w_c C_m T_c$
w_c
w_i
2
$\frac{1}{S}$
T_i
$\dot{T}_i$
$W_i C_i$
$W_i C_i \dot{T}_i$
$W_{w2} C_{w2} + W_f C_f + W_{mi} C_m$
V_{it}
$\frac{1}{\rho_m}$
W_{mi}
A_s
P_t
$G(T_{mI} + 460)^4$
E_{ff}^e
$A_i E_{ff}^e \left[G(T_{m3} + 460)^4 - P_t \right]$

FIGURE 24

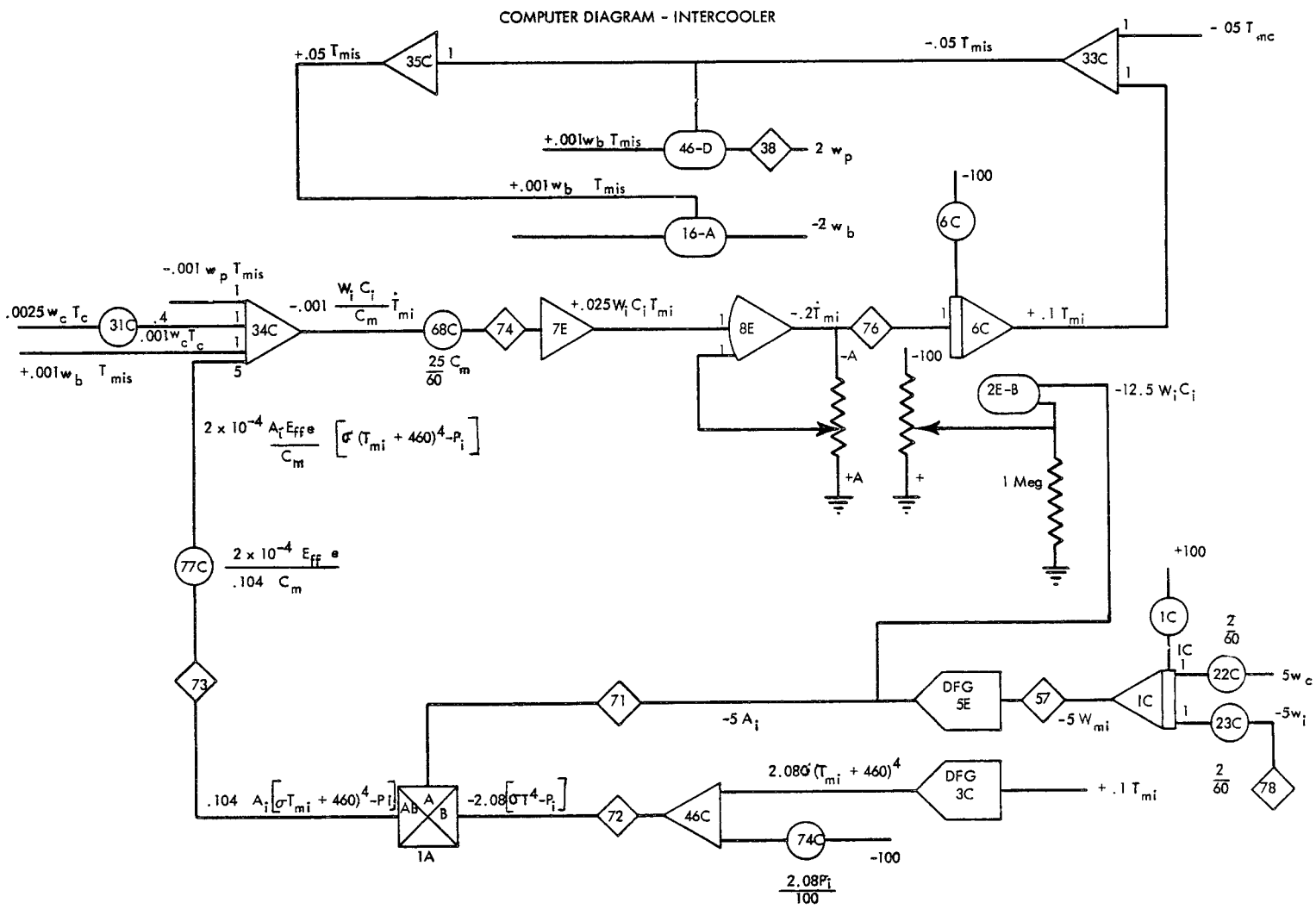
COMPUTER DIAGRAM - INTERCOOLER
+.05 T_mis
35C
-.05 T_mis
33C
- 05 T_mc
+.001w_b T_mis
46-D
38
2 w_p
+.001w_b T_mis
16-A
-2 w_b
-100
6C
-.001 w_p T_mis
.0025 w_c T_c
31C
.4
.001w_c T_c
34C
-.001 W_i C_i / C_m Ṫ_mi
68C
25/60 C_m
74
7E
+.025 W_i C_i T_mi
8E
-.2Ṫ_mi
76
6C
+.1 T_mi
+.001w_b T_mis
5
2 x 10^-4 A_i E_ff e / C_m [σ (T_mi + 460)^4 - P_i]
-A
+A
-100
+
2E-B
-12.5 W_i C_i
1 Meg
77C
2 x 10^-4 E_ff e / .104 C_m
+100
1C
2/60
IC
22C
5w_c
23C
-5w_i
73
71
-5 A_i
DFG 5E
57
-5 W_mi
IC
2/60
78
.104 A_i [σT_mi + 460)^4 - P_i]
AB
A
B
1A
-2.08 [σT^4 - P_i]
72
46C
2.08σ (T_mi + 460)^4
DFG 3C
+.1 T_mi
74C
-100
2.08P_i / 100

INFORMATION PLOTTED ON DFG 3-C
STEFAN-BOLTZMANN TEMPERATURE RELATIONSHIP

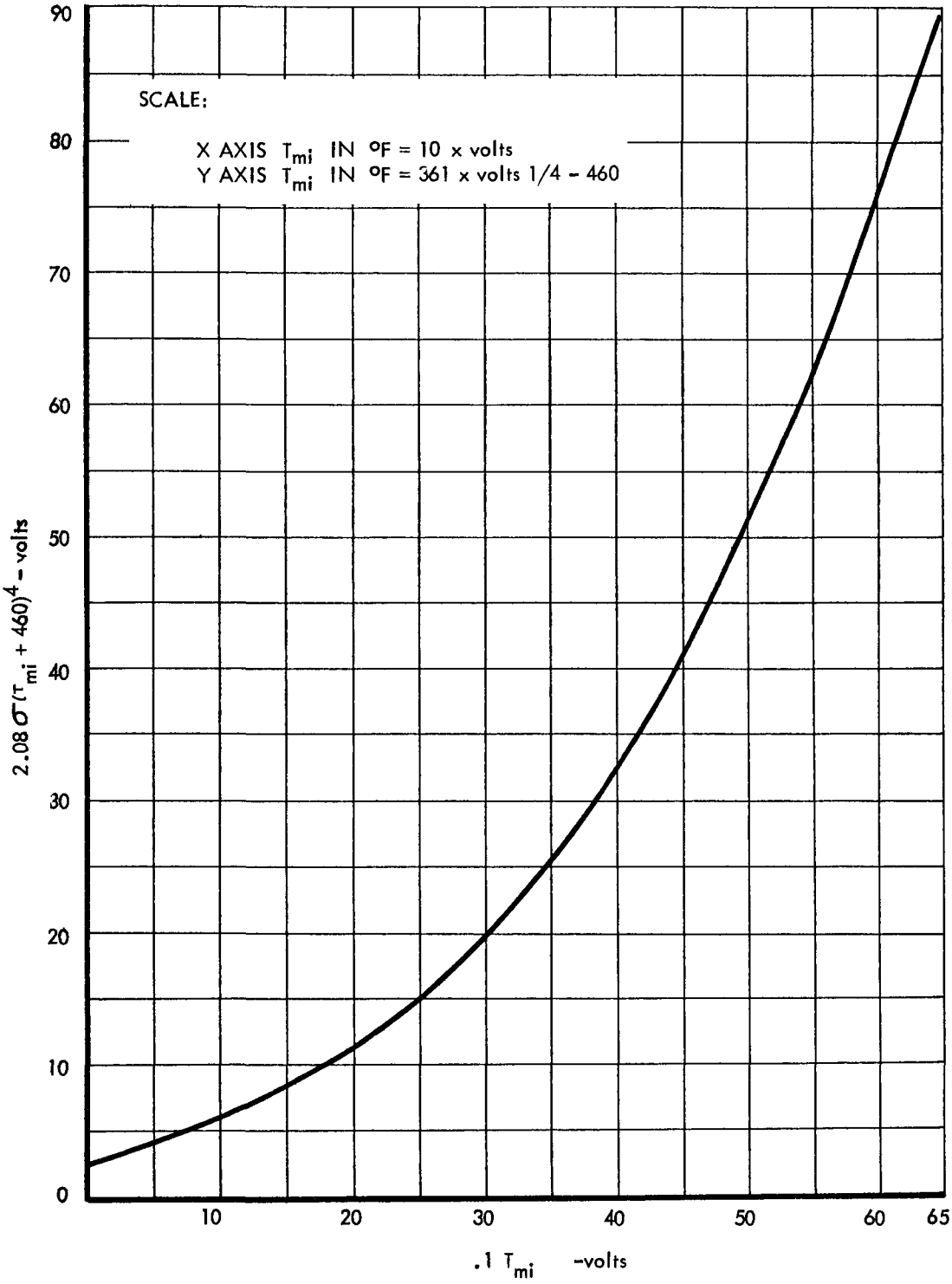

FIGURE 26

INTERCOOLER DFG 5E

INTERCOOLER INVENTORY-AREA-HEAT CAPACITANCE RELATIONSHIP

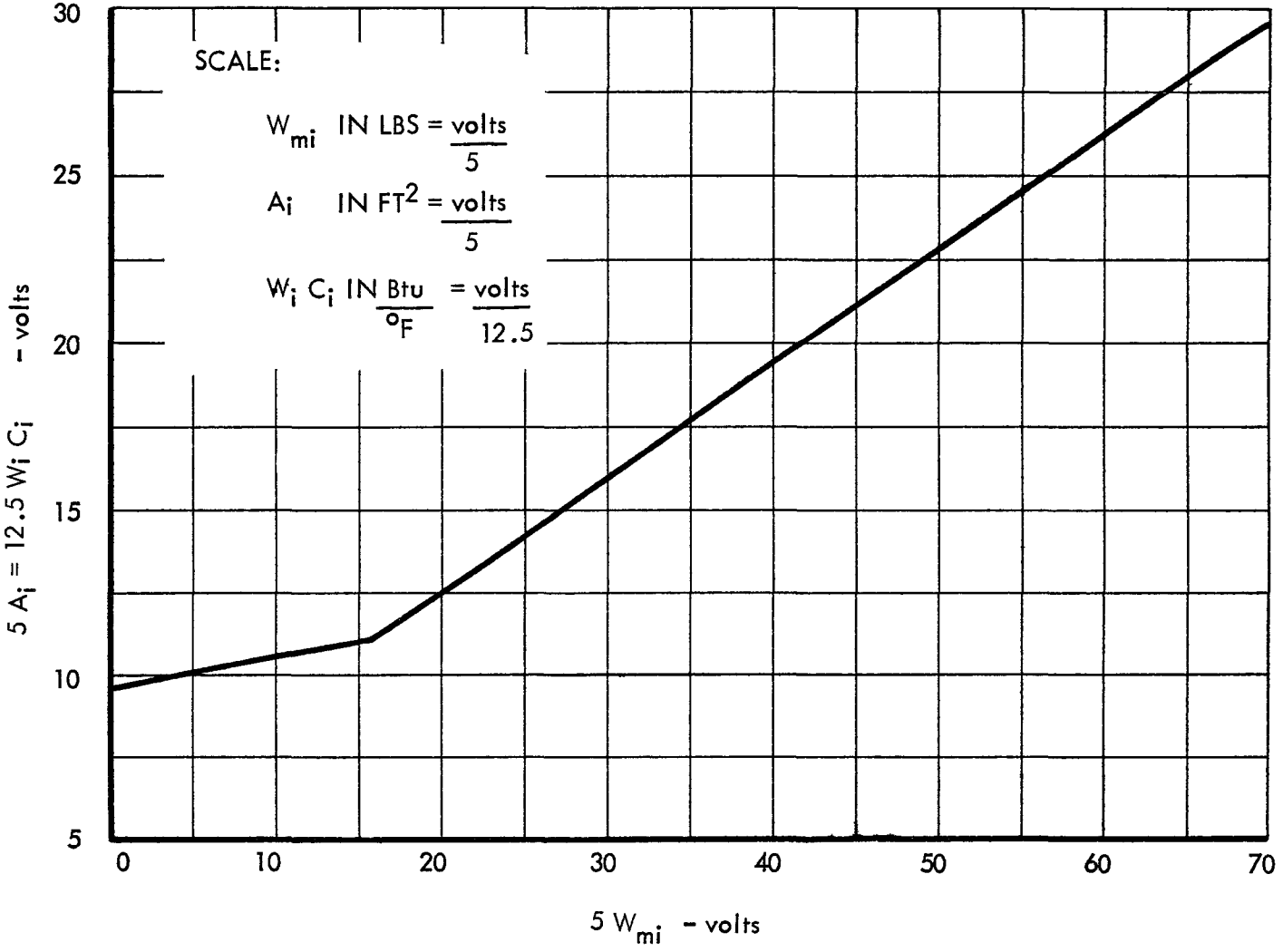

FIGURE 27

SUBCOOLER EQUATIONS

(62) $T_{ms} = T_s$

(63) $w_i C_m T_{mis} + w_b C_m T_{mbs} - A_s E_{ffe} \left[\sigma (T_{ms} + 460)^4 - P_i\right] - w_p C_m T_{msp} = W_{su} C_{su} \frac{d T_{ms}}{dt}$

(64) $W_{sm} C_{su} - W_{ms} C_m + W_{ws} C_{ws} + W_{fs} C_{fs}$

(65) $T_{msp} = T_{ms} + (T_{ms} - \frac{w_b}{w_p} T_{mbs} - \frac{w_i}{w_p} T_{mis})$

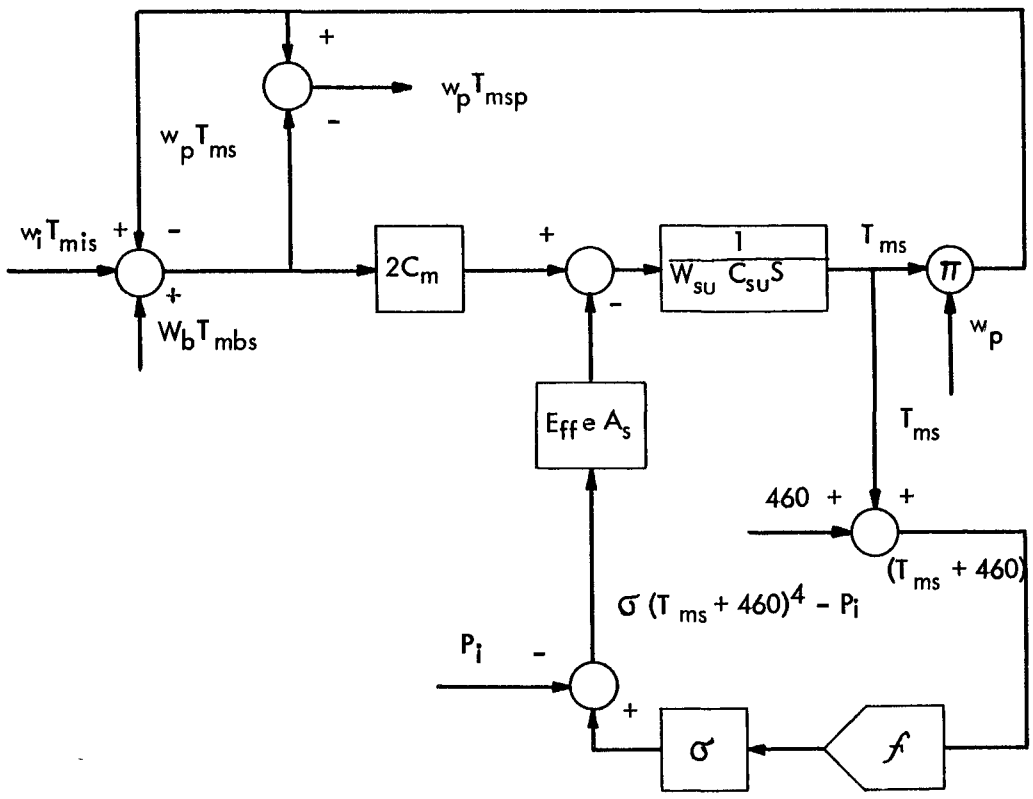

FIG. 28 BLOCK DIAGRAM - SUBCOOLER

COMPUTER DIAGRAM - SUBCOOLER

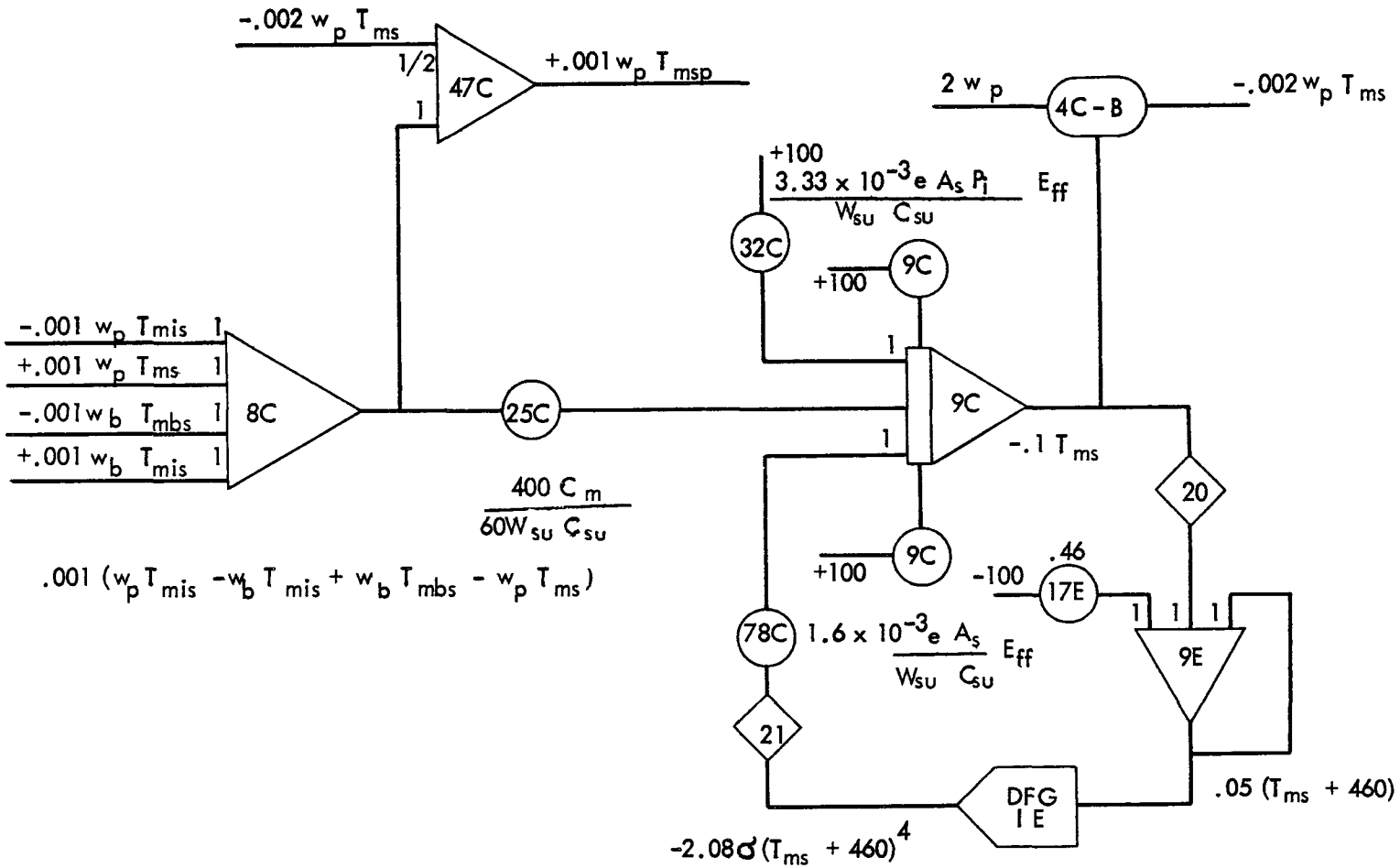

FIGURE 29

G. Mercury Pump

A centrifugal type pump is used in the mercury system. The useful power loss increases the pump outlet temperature. Any difference between the system pressure requirements and the head developed provides an acceleration force on the fluid stream. Equations (66) through (74) describe the pump performance while the block diagram and computer diagram are shown in Figures 30 and 31. The pump characteristics defining head pressure as a function of rotor speed and weight flow are shown in Figure 32.

H. Bearings

Two journal bearings are used to support the rotating mass. Mercury serves as the lubricating medium and absorbs the heat energy generated by friction losses. Mercury enters the bearings at pump outlet pressure and is assumed to exit at condenser pressure since no pressure drop other than the bearing losses occur in this fluid branch. Equations (75), (76) and (77) describe the fluid action in the bearings. Figures 33 and 34 give the block and computer diagrams.

I. Sodium Pump

The sodium pump is an electromagnetic device which has performance characteristics similar to those of a centrifugal type pump. The shaft power taken by the pump is accounted for in the external system flow losses, internal pump losses, and fluid stream acceleration. A difference in pressure head and load pressure drop provides an accelerating force on the fluid stream. The pump head pressure is assumed to be a function of only rotor speed. The pump performance is given by equation (78) through (82). Block and computer diagrams are shown in Figures 35 and 36.

J. Alternator

The alternator converts mechanical shaft power to electrical load power. The power losses are proportional to the square of the generated frequency. The power losses in the alternator, the actual load power, and the parasitic power constitute the total electrical load on the shaft. Equations (83) through (86) define the alternator characteristics. The block and computer diagrams are shown in Figures 37 and 38.

K. Parasitic Load Control

Figure 38 presents the parasitic load control. The load control is a proportional type of control that senses the speed error and varies the electrical load to maintain rotor speed at 40,000 RPM $\pm$ 1%.

MERCURY PUMP EQUATIONS

(66) $$P_{mpt} = N_3 \left[K_{mp1} \; w_p + K_{mp2} \right]$$

(67) $$P_{mph} = w_p \; v_m \; p_{mh}$$

(68) $$p_{ma} = p_{mh} - p_{ms}$$

(69) $$\frac{d \; w_p}{dt} = K_{ma} \; p_{ma}$$

(70) $$T_{mib} = T_{msp} + \frac{P_{mpt} - P_{mph}}{J \; C_m \; w_p}$$

(71) $$p_{mh} = f(N, \; w_p)$$

(72) $$p_{ms} = p_2 - p_c$$

(73) $$p_{mip} = p_c - \frac{K_2}{K_{1t} \; K_2} \; p_{ma}$$

(74) $$p_{mop} = p_2 + \frac{K_1}{K_1 + K_2} \; p_{ma}$$

BLOCK DIAGRAM - MERCURY PUMP

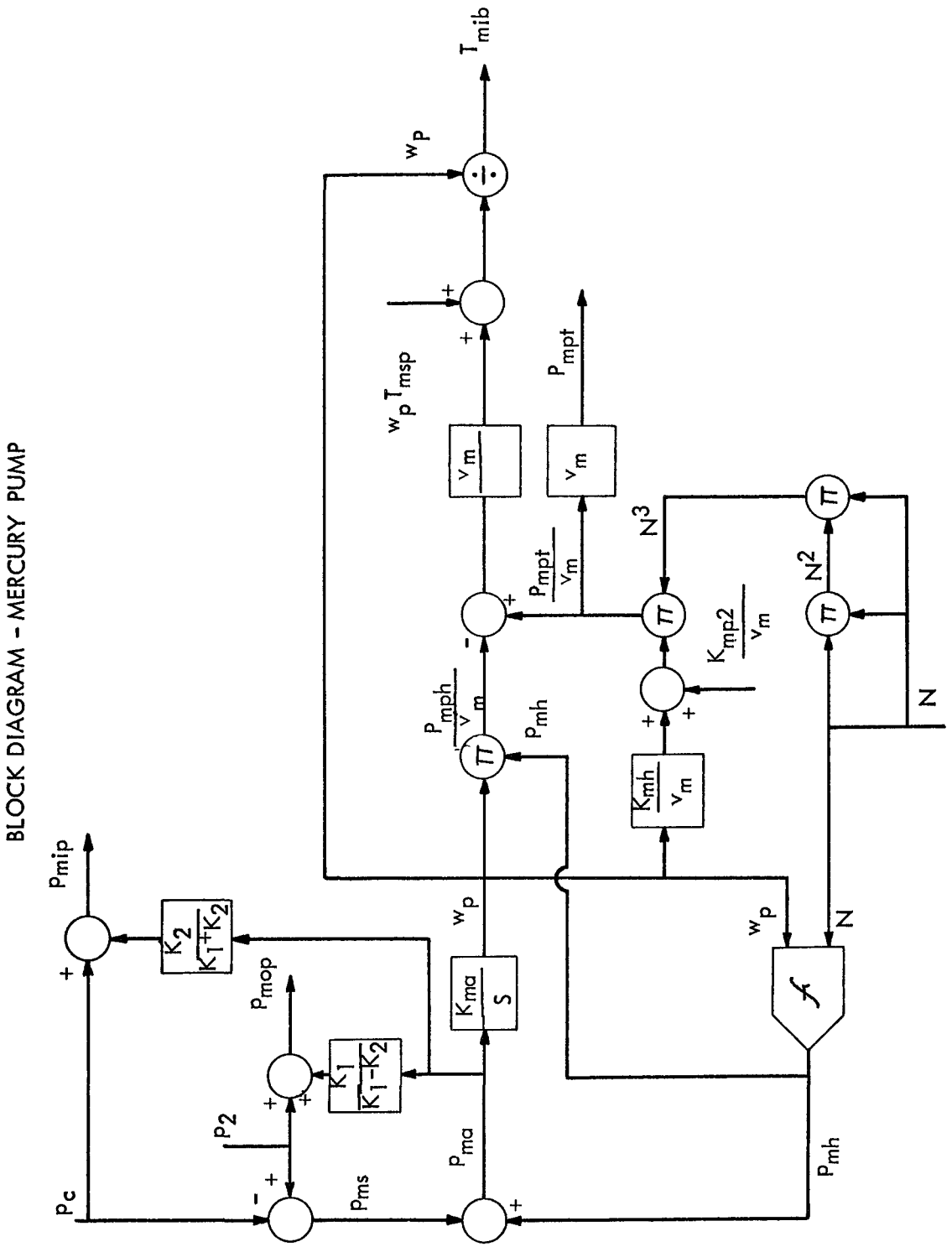

FIGURE 30

COMPUTER DIAGRAM - MERCURY PUMP

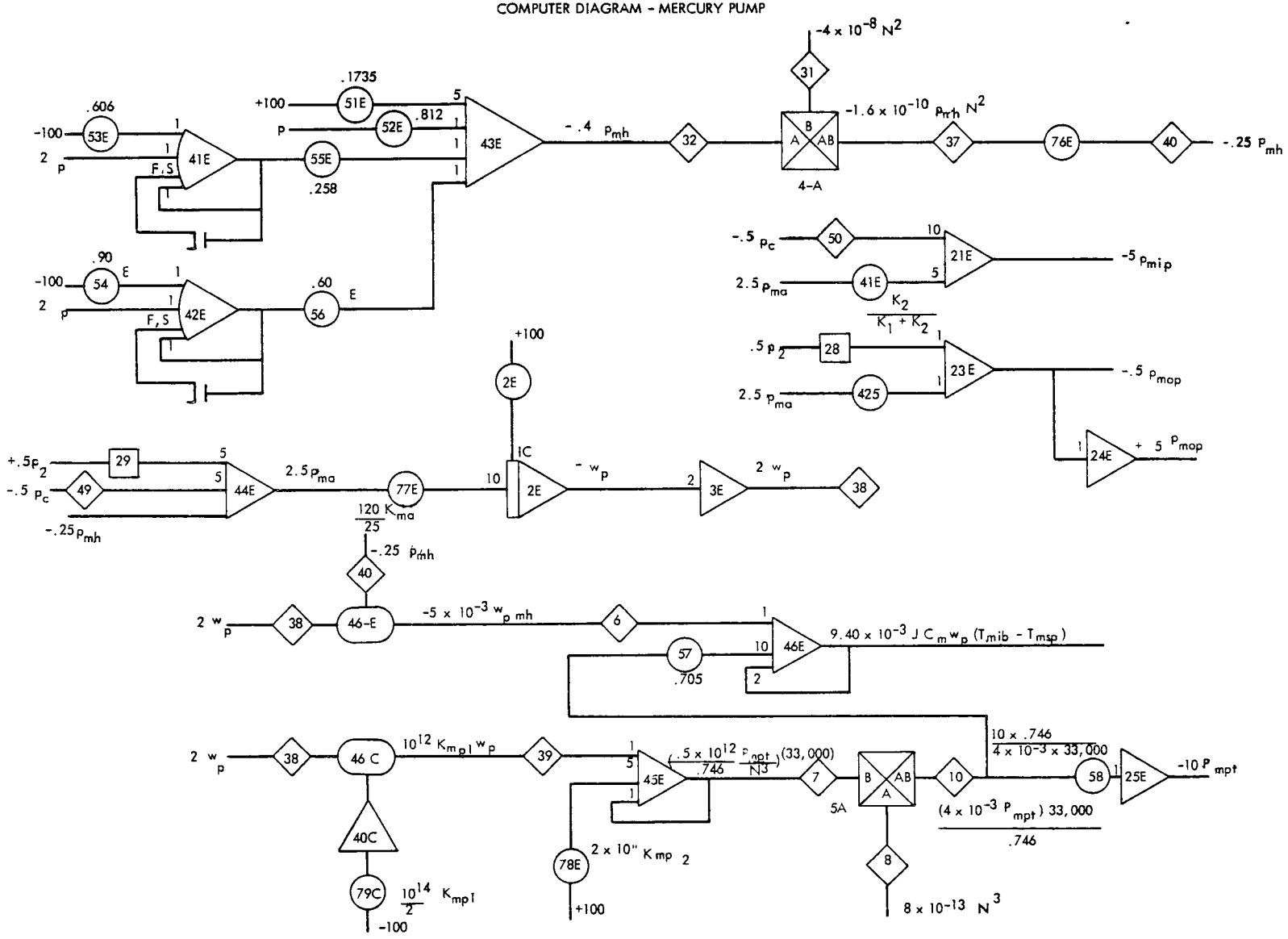

MERCURY PUMP CHARACTERISTICS

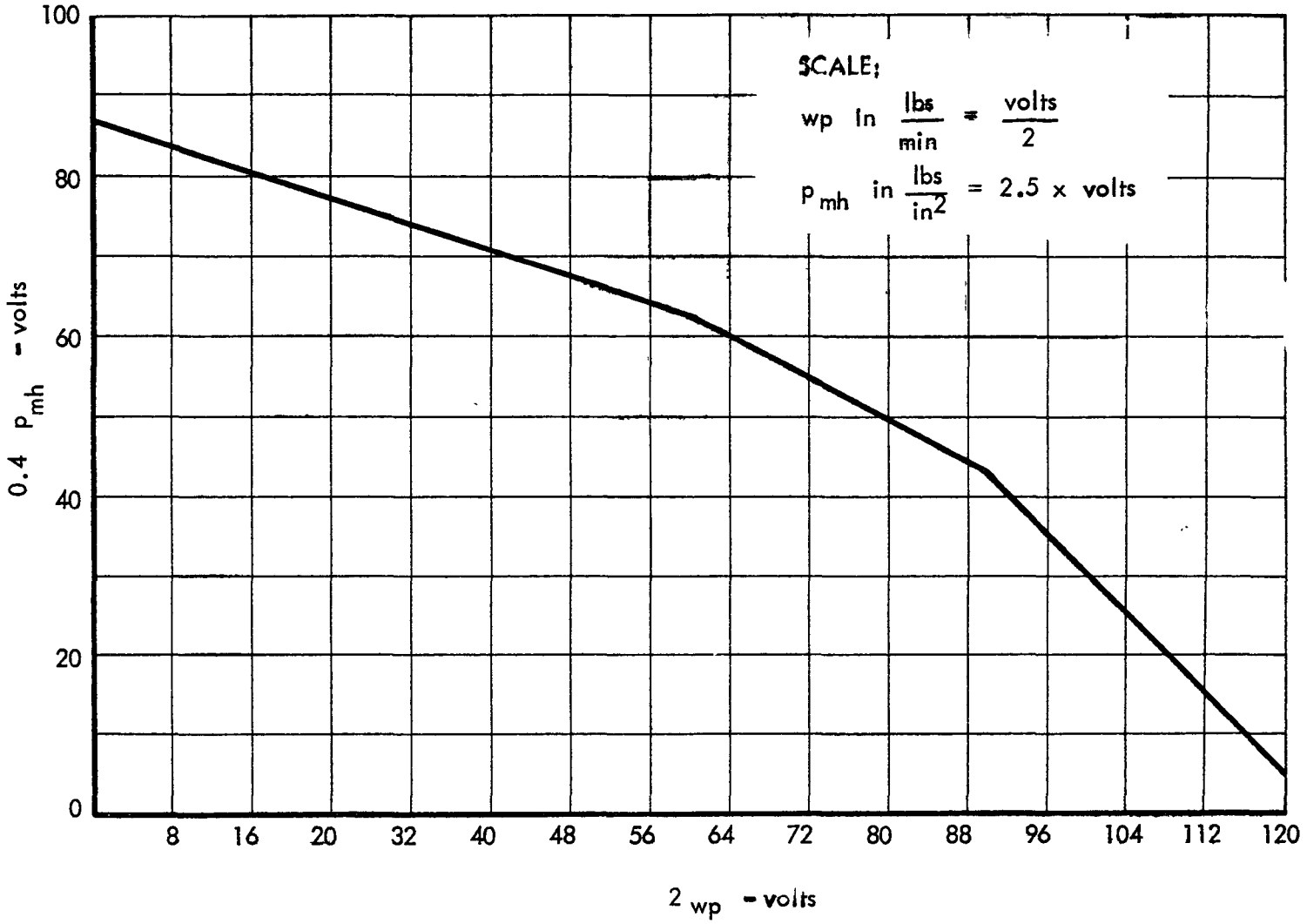

FIGURE 32

MERCURY BEARING EQUATIONS

(75) $w_b = K_b (p_{mop} - p_c)$

(76) $P_b = K_c N^2$

(77) $T_{mbs} = T_{mlb} + \dfrac{P_b}{w_b C_m J}$

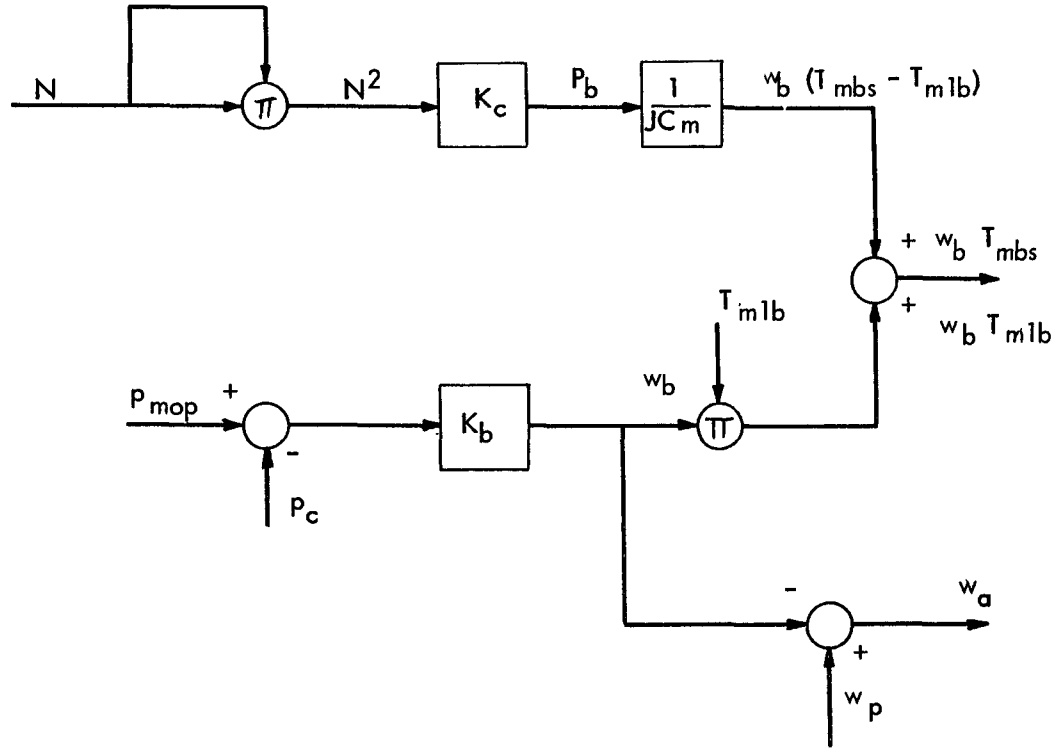

FIG. 33 BLOCK DIAGRAM - MERCURY BEARINGS

COMPUTER DIAGRAM-MERCURY BEARINGS

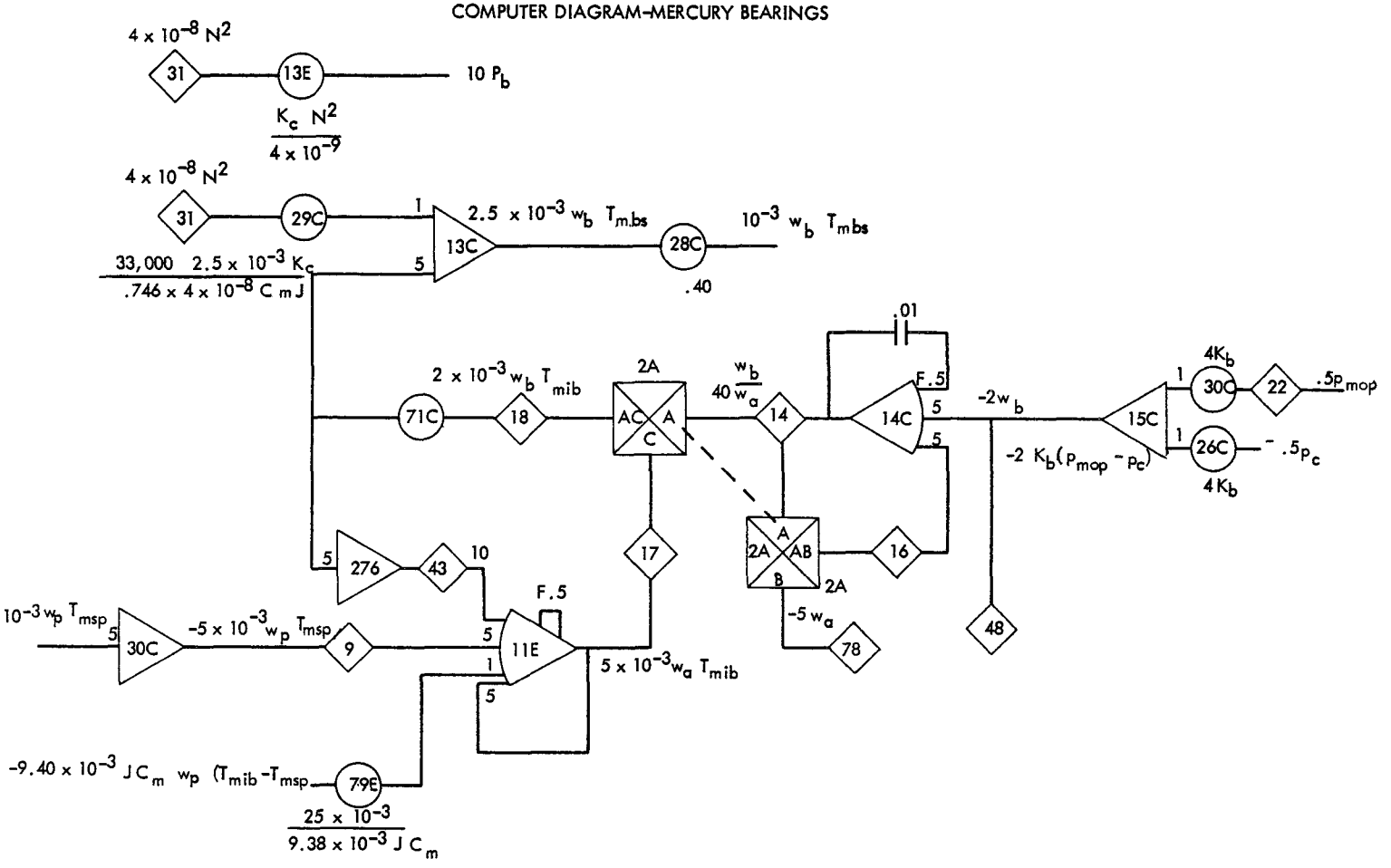

FIGURE 34

SODIUM PUMP EQUATIONS

(78) $$P_{spt} = \frac{w_s \; v_s \; p_{sm}}{e_s}$$

(79) $$p_{sa} = p_{sm} - p_{ss}$$

(80) $$\frac{dw_s}{dt} = K_{sa} \; p_{sa}$$

(81) $$p_{sh} = K_{sh} \; N^2$$

(82) $$p_{ss} = K_{ss} \; w_s^2$$

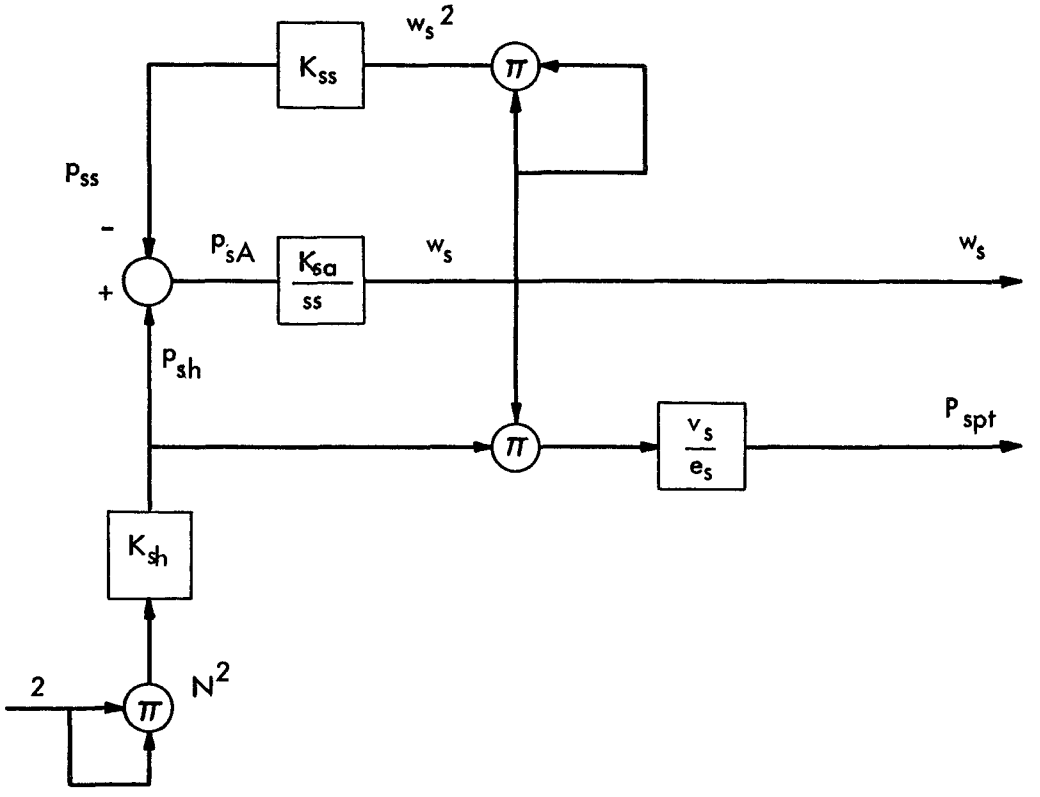

FIG. 35 BLOCK DIAGRAM - SODIUM PUMP

COMPUTER DIAGRAM - SODIUM PUMP

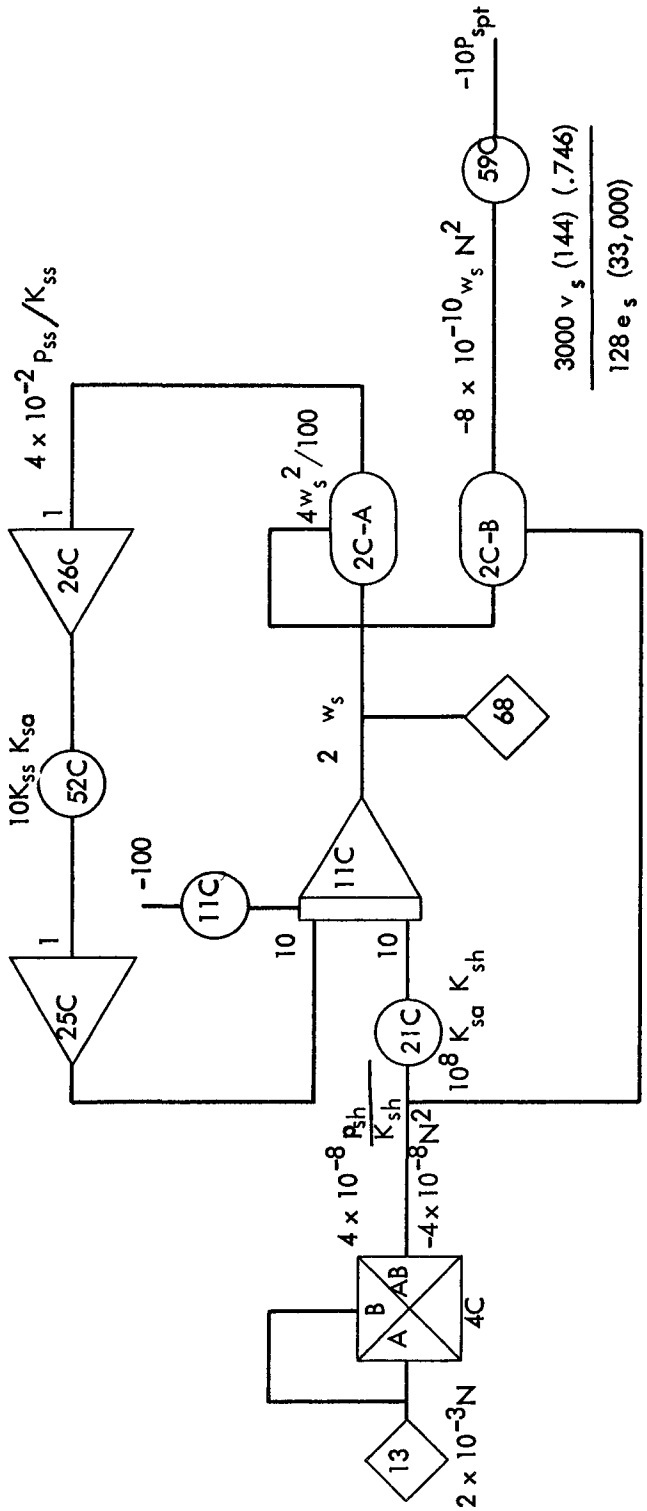

FIGURE 36

ALTERNATOR EQUATIONS

(83) $$P_{al} = E\ i_l \cos\Theta = \frac{E^2}{R_p}$$

(84) $$E = f(N)$$

(85) $$P_c = K_l\ N^2$$

(86) $$P_a = P_p + P_c + P_{al}$$

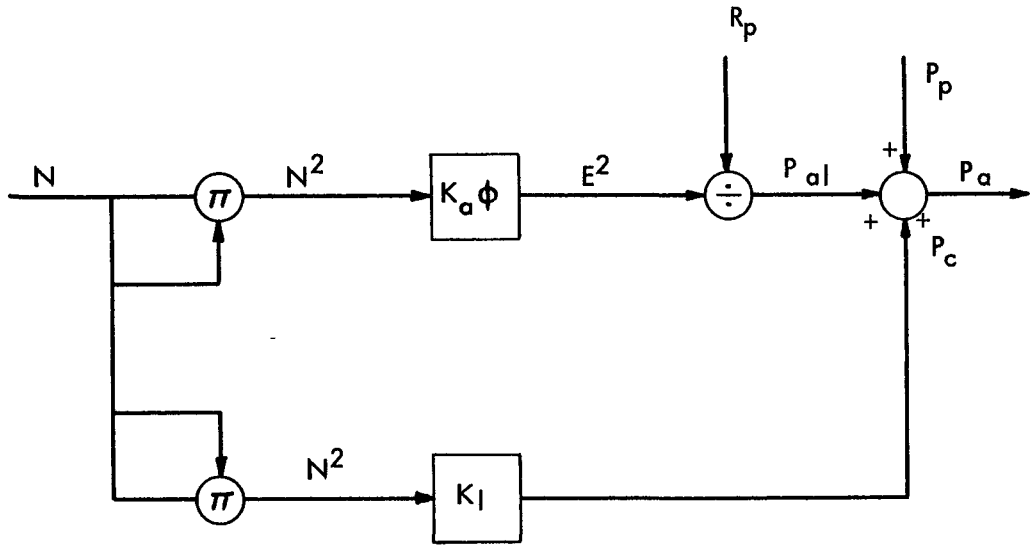

FIG. 37 BLOCK DIAGRAM - ALTERNATOR

COMPUTER DIAGRAM - ALTERNATOR AND CONTROL

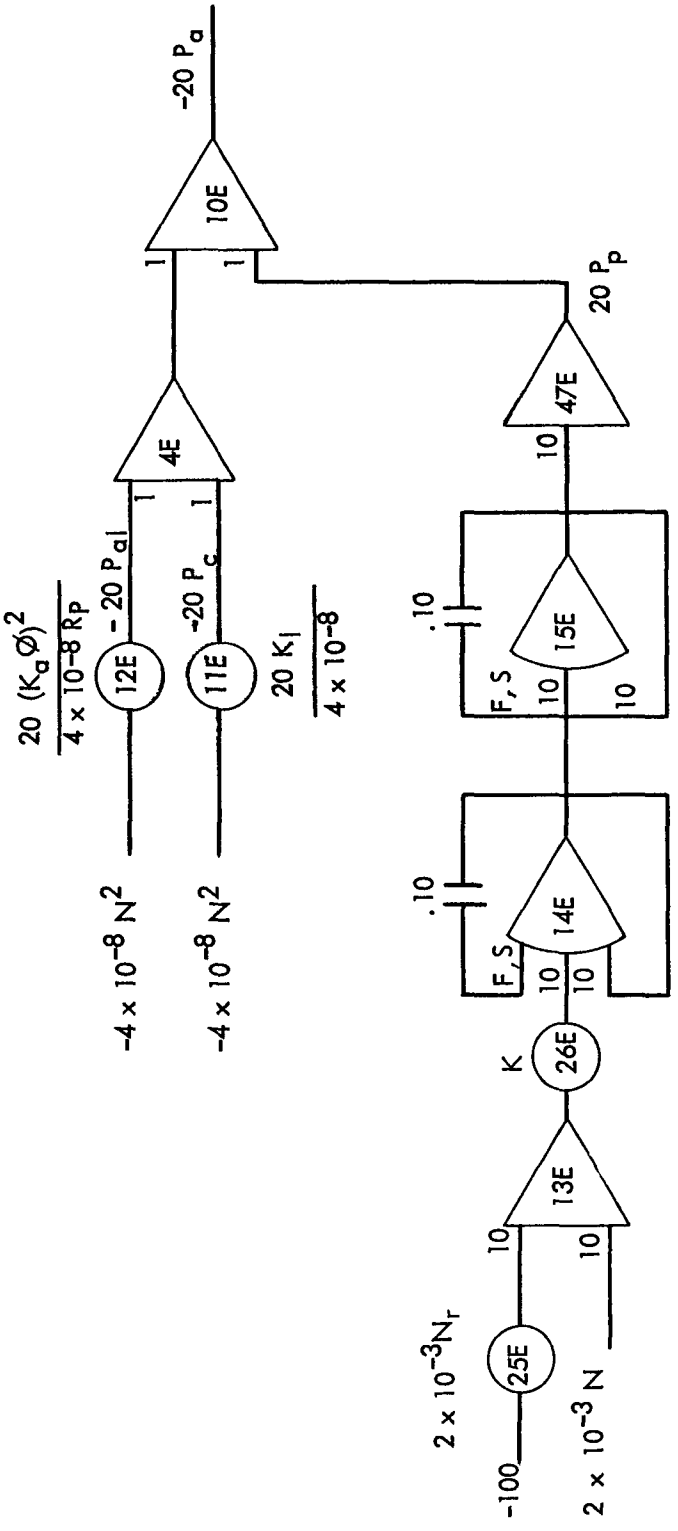

FIGURE 38

L. Rotor Dynamics

The rotor dynamics are described by a power balance between the turbine output and associated loads. Changes in this power balance exert an accelerating torque upon the rotor.

The components affecting the shaft power are the turbine, pumps, bearings, and electrical load. The power balance is shown in equation (87). The block and computer diagrams are presented in Figures 39 and 40.

IV. DYNAMIC ANALYSIS

In order to establish the dynamic performance of the power conversion system, a suitable control for the system was required, since the system is inherently unstable. For example, an increased power demand on the shaft of the combined rotating unit will cause rotor speed to decrease. The speed decrease lowers the mercury pump discharge pressure and consequently the turbine inlet pressure. The drop in turbine inlet pressure decreases turbine power which results in an even greater power unblance. This action will continue until the rotor speed decays to zero. Conversely, with a decrease in load, the rotor will increase in speed until a destructive critical speed is reached. A suitable control is therefore mandatory to satisfactorily operate the system.

The objectives of the control were as follows:

1. The control shall provide complete stability for the system under all operating conditions.

2. The control shall provide maximum reliability of system operation.

3. The control shall maintain the system output within the specified tolerances of $\pm$ 1% on frequency or speed.

4. The control shall maintain reactor power relatively constant to avoid temperature cycling of the reactor and heat exchanger.

A large number of conceivable control parameters were evaluated for each component. The following table illustrates the possible controls considered:

ROTOR DYNAMICS EQUATIONS

(87) $$P_t - P_a - P_b - P_{spt} - P_{mpt} = K_r N I \frac{d N}{dt}$$

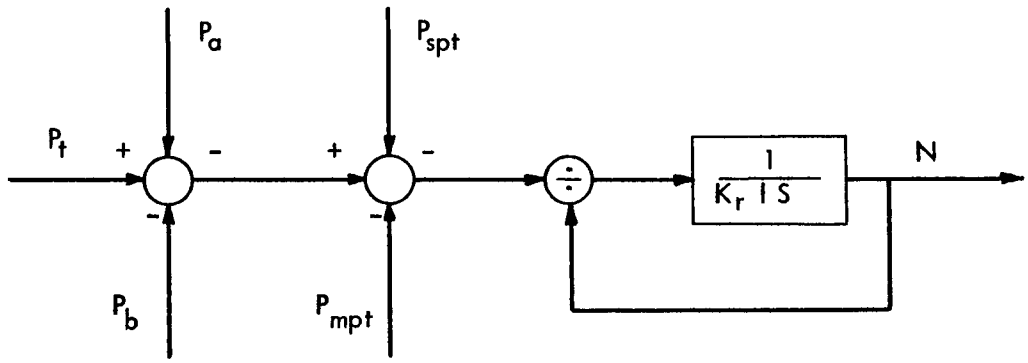

FIG. 39 BLOCK DIAGRAM - ROTOR DYNAMICS

COMPUTER DIAGRAM-ROTOR DYNAMICS

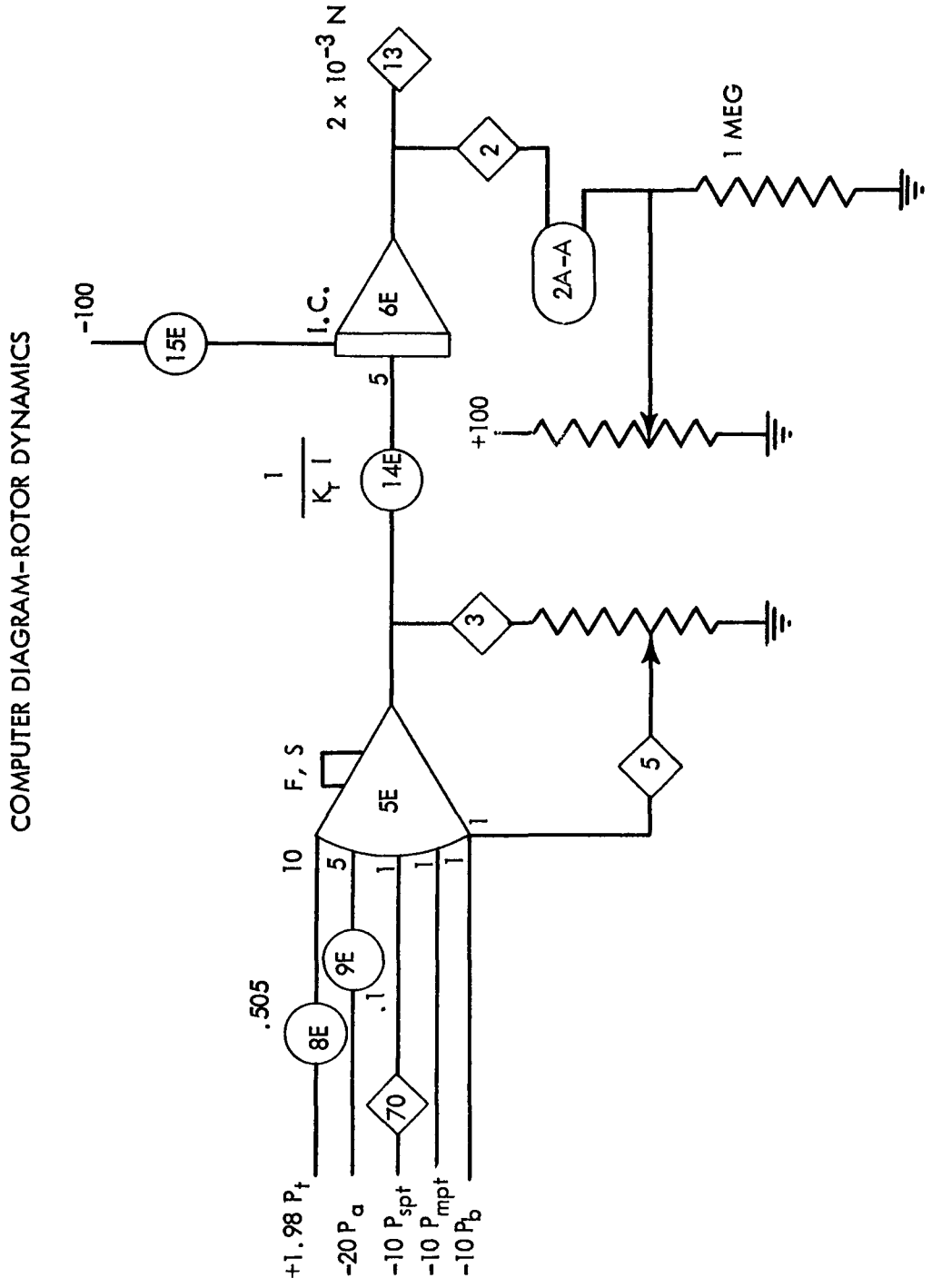

FIGURE 40

	Input Variables	Controlled Variables
1. Boiler	Reactor power	Pressure out of boiler
	Mercury inlet temperature	Temperature out of boiler
	Mercury inlet pressure	Temperature out of boiler
	Mercury weight flow	Temperature out of boiler
2. Turbine	Inlet pressure	Turbine power
	Inlet temperature	Turbine power
	Exhaust pressure	Shaft speed
3. Shaft Mechanical Load	Turbine power	Alternator shaft power
	Bearing power	Alternator shaft power
	Pump power	Alternator shaft power
4. Load	System load power	Alternator electrical load
	Parasitic power	Alternator electrical load

Analysis of the possible control parameters reduces the number of control possibilities. For the boiler, reactor power variations are undesirable because of the attendant temperature cycling. Variations in inlet mercury temperature produce little effect on boiler operation. Variation in boiler inlet pressure by means of control valve is a conceivable control method which is employed in the SNAP I mercury power conversion system. Because of the larger SNAP II boiler, however, a control of boiler inlet pressure would have a poor response characteristic in controlling boiler outlet conditions. Mercury weight flow through the boiler could be controlled by a turbine bypass valve. A high temperature, high response mercury vapor valve with suitable reliability, weight and seal characteristics is a difficult development effort, however.

For the turbine, control of inlet pressure by means of a throttle valve is a possible means of controlling turbine power output. The combination of a bypass valve and a turbine throttle valve could be utilized to maintain constant boiler conditions while varying turbine inlet pressure. This control technique is commonly used in commercial power plant systems. The valve development disadvantage, however, remains. Variation of turbine inlet temperature does not vary the turbine power sufficiently to serve as a good control parameter. Variation of turbine discharge pressure only affects the last stage of the turbine performance and consequently is also a poor control variable. A relatively large control valve would be required for turbine discharge pressure control with the added disadvantage of considerable weight.

A practical control for variation of shaft mechanical power would exclude pump and bearing power variations because of their small magnitude. A parasitic alternator has been utilized for control of shaft mechanical power, but such a device would complicate the design of the combined rotating unit in the SNAP II system.

The only remaining independent control parameter is a parasitic load device which can control the output of the alternator. This proportional type of control is comprised of a frequency sensing device, a magnetic amplifier, and a resistive load. This type of control was selected because of its simplicity, low weight, and ability to meet the control objectives.

Detailed parasitic load control studies were performed with a constant heat input to the conversion system. Since the output power from the turbine is greater than the power required from the various components, the rotor would accelerate unless parasitic load power is carried by the system. For the large power transients shown in Figures 41 and 42, it was assumed that sufficient parasitic load was carried by the system to account for the changing demands. For the remainder of the system analysis, the parasitic load was assumed to be the power developed by the turbine in excess of that demanded by the pumps, bearings, and alternator. This amounted to approximately 300 watts which proved sufficient for all transients.

The use of a proportional control system necessitates a steady state speed error. The optimum control gain was chosen as 4.65 watts/RPM with a dynamic response of approximately 0.2 seconds. The maximum speed error obtained with a 50% electrical load disturbance is within the ± 1% speed limits. In this case, sufficient parasitic power must be available, as previously mentioned. Subsequent studies were performed with a control loop gain of 4.65 watts/RPM.

Figure 41 shows the control performance with a 50% step increase in electrical load requirement. The steady state speed decrease 0.75%, and system stability is obtained within 0.2 seconds. Since the control performance is fast as compared to the system, the remainder of the system is not subjected to transients. However, due to the decrease in steady state speed, the system operates slightly off design, consequently the turbine inlet temperature increases by 30°F. This is due to the fact that the mercury pump flow decreases, thus requiring less heat to maintain the 1150°F turbine inlet temperature level. Since the heat input to the boiler remained constant, the outlet temperature must increase. Figure 42 shows a corresponding step decrease of 50% in electrical load requirement. The steady state speed increases by 0.75% and a decrease of 30°F is obtained for turbine inlet temperature.

Figures 43 and 44 show the chosen control performance for 10% changes in electrical load. The recordings indicate a speed change of approximately 0.15% off design speed or 60 RPM. It is assumed that for normal operating conditions, the power con-

version system will not experience load variations in excess of ± 10%. The recovery time is within 0.2 seconds. Figure 45 shows the control performance for a 10% electrical load change with increased control loop gain. The steady state error is reduced to less than 0.1% of design speed. However, a slight overshoot in rotational speed is obtained.

On the following pages the effects of component variations over a wide operating range are individually discussed. With the parasitic load control, the rotational speed was maintained with the limits of 40,000 RPM for all disturbances applied to the system. Some of the traces that follow exhibit random high frequency variations of small amplitude. This is noise due to the operation of the servo-multipliers and does not reflect system performance.

A. Reactor Temperature Transients

In order to determine the performance of the reactor, it was initially analyzed separately from the thermodynamic system. While operating the reactor open loop, the sodium flow, w_s, was held constant at 45.2 lbs/min. Since the reactor has a negative temperature coefficient, affording inherent control, the average temperature of the sodium within the reactor will tend to remain constant. Therefore if the temperature input, T_{sob}, to the reactor is increased, the temperature outlet, T_{sib}, will decrease with an associated drop in power level. Conversely, the reverse must hold true for a decrease in T_{sob}.

With the reactor operating at steady state conditions, T_{sob} was increased from 999°F to 1024°F. The results shown in Figure 46 indicate the action of the negative temperature coefficient. After the reactor had steadied out at this new off-design level, T_{sob} was decreased and the system brought back to design, Figure 47. This procedure was then reversed to obtain similar off-design data in the opposite direction. These runs are shown in Figures 48 and 49. An important characteristic of the reactor is its extremely slow response. It is seen from these traces that for a step in T_{sob} of 25°F it takes approximately sixty five seconds for the heat source to change T_{sib} to its new operating level. This slowness indicates that hunting may occur when the reactor is coupled to the thermodynamic system.

B. Reactor Power Transients

It was desired to determine the system stability for increases in reactor power. With the complete system operating at steady state conditions, a ramp increase in reactivity was applied to the reactor bringing the power up at a rate of 0.5 KW/sec to approximately 130% of rated output. The additional heat output of the reactor was used to raise the average fuel temperature which in turn raised the sodium temperature levels. The mercury system will only accept essentially design power since the parasitic load by holding nearly constant speed, maintains mercury flow very near design point. At this flow and regardless of pressure, the heat of vaporization of mercury remains constant. This heat, along with the heat necessary to preheat the mercury, which remains con-

stant since the entering temperature to the heat exchanger remains essentially the same, constitute over 95% of the heat accepted by the boiler.

Any change in superheat temperature caused by sodium temperature variations will reflect only as small variations in total power absorption by the boiler. In fact, for mercury leaving the superheater at the physical maximum of 1200°F, the total power accepted by the boiler will increase less than 1 %. Therefore, the boiler forces the reactor, which is a load following device, to return to design power level. As Figures 50a, 50b, and 50c show, the inherent control feature of the reactor along with the time lag associated with sodium temperature and reactor power cause the system to converge on the new values very slowly. In fact, five to ten minutes pass before the system fluctuations subside to a reasonable value. This approaches the hunting effect that was mentioned earlier. These traces also point out the sensitivity of mercury turbine inlet temperature, T_{mbt}, to a change in temperature of the sodium entering the heat exchanger, T_{sib}. This suggests that a reactor control based on temperature would be helpful in maintaining system performance constant.

Controlling on either sodium temperature at the heat exchanger inlet, T_{sib}, or mercury temperature at the turbine inlet, T_{mbt}, would seem logical in order to maintain constant system conditions. Controlling on T_{mbt} has the advantage that this temperature is the most sensitive in the system. Since relatively large T_{mbt} variations on the order of plus or minus fifty or seventy-five degrees, can be tolerated, an on-off type of control might be utilized. However, one large disadvantage is the corrosive action of mercury. If a thermocouple were installed in the mercury line, a sheath would be required. The sheath would slow down the thermocouple response, offsetting the advantage of using T_{mbt} as a signal. Since T_{sib} is a major factor in causing T_{mbt} to vary, it would seem an ideal control parameter. A control based on this temperature would have to be much more sensitive since this signal does not vary nearly as much as T_{mbt}. Small perturbations within the mercury loop, however, would not affect the system to any great extent. The sodium temperature sensor therefore appears to be the more practical control approach.

C. Pump Flow Transients

In the case where mercury pump flow was varied, not only was the system performance important, but also of special interest was the effect the increased flow demand would have on the pump inlet pressure. In order to satisfy the system demand for a step increase in flow, the pump inlet pressure must decrease rapidly, thus providing the force necessary to accelerate the mercury. Conversely, the reverse must hold true for a decrease in w_p. Figures 51a and 51b show that for an increase in pump flow of 4%, the pump inlet pressure must drop to 3.8 psi in order to supply the system demand. This indicates that larger step increases should be avoided in order to prevent pump cavitation problems. Also T_{mbt} decreases as expected because of the additional mercury flowing through the heat exchanger. From studying the traces it is apparent that the heat exchanger is very sensitive to small disturbances in w_p. However, the system responds very rapidly

to these disturbances, the time being in the neighborhood of one quarter to one half second. Figures 52a and 52b show system dynamics for a decrease in w_p. Again it is seen that rotor speed and parasitic load are unaffected.

D. Bearing Flow Transients

Figures 53a and 53b show the effect of an increase in mercury bearing flow. Since a greater portion of the pump flow is now used in the bearings, the flow through the heat exchanger must decrease. This in turn causes the turbine inlet temperature, T_{mbt}, to increase to some new steady state value. Shown in Figures 54a and 54b is the system response for a decrease in w_b. Here the trends reverse themselves as expected. The increased w_a causes T_{mbt} to decrease. Rotational speed and hence parasitic load indicate no apparent change in the power balance of the system.

E. Sun-Shade Operation

Figures 55a and 55b show the changes occurring in the system when the vehicle is traveling in the shade. Since shade operation enables the condensing portion to radiate at an increased rate, it follows that the subcooled mercury temperature must decrease. This is evident in T_{mib}. Even though this temperature decreases, the action of the parasitic load control, keeping the speed constant, tends to maintain design power level from the turbine. The recordings indicate that system performance will be virtually unaffected by the sun-shade transient.

V. CONCLUSIONS

As a result of the dynamic simulation of the SNAP II power conversion system, the following conclusions may be drawn:

A. The parasitic load control can maintain the speed of the combined rotating unit within the 40,000 RPM $\pm$ 1% specification. As a result of this speed control the mercury system demands essentially constant power from the reactor.

B. The system can withstand large power transients due to the action of the parasitic load control. The control will force the system to remain at essentially constant power and temperature levels.

C. A reactor temperature control based on the sodium temperature at the heat exchanger inlet is recommended.

D. System performance is not effected by 4% step increases in pump flow. Larger step increases could cause mercury pump cavitation. Pump pressure vs flow characteristics currently attainable are satisfactory for system performance.

E. Changes in bearing flow rate of $\pm$ 2 pounds do not adversely effect system performance.

F. Sun-shade transients are insignificant to the system performance.

G. Operation of a mercury power conversion system with a fixed mercury inventory does not adversely effect performance.

FIG 41 CONTROL ANALYSIS $\frac{P_{p(s)}}{N(s)} = \frac{4.65}{(1+.02s)^2} \frac{WATTS}{RPM}$

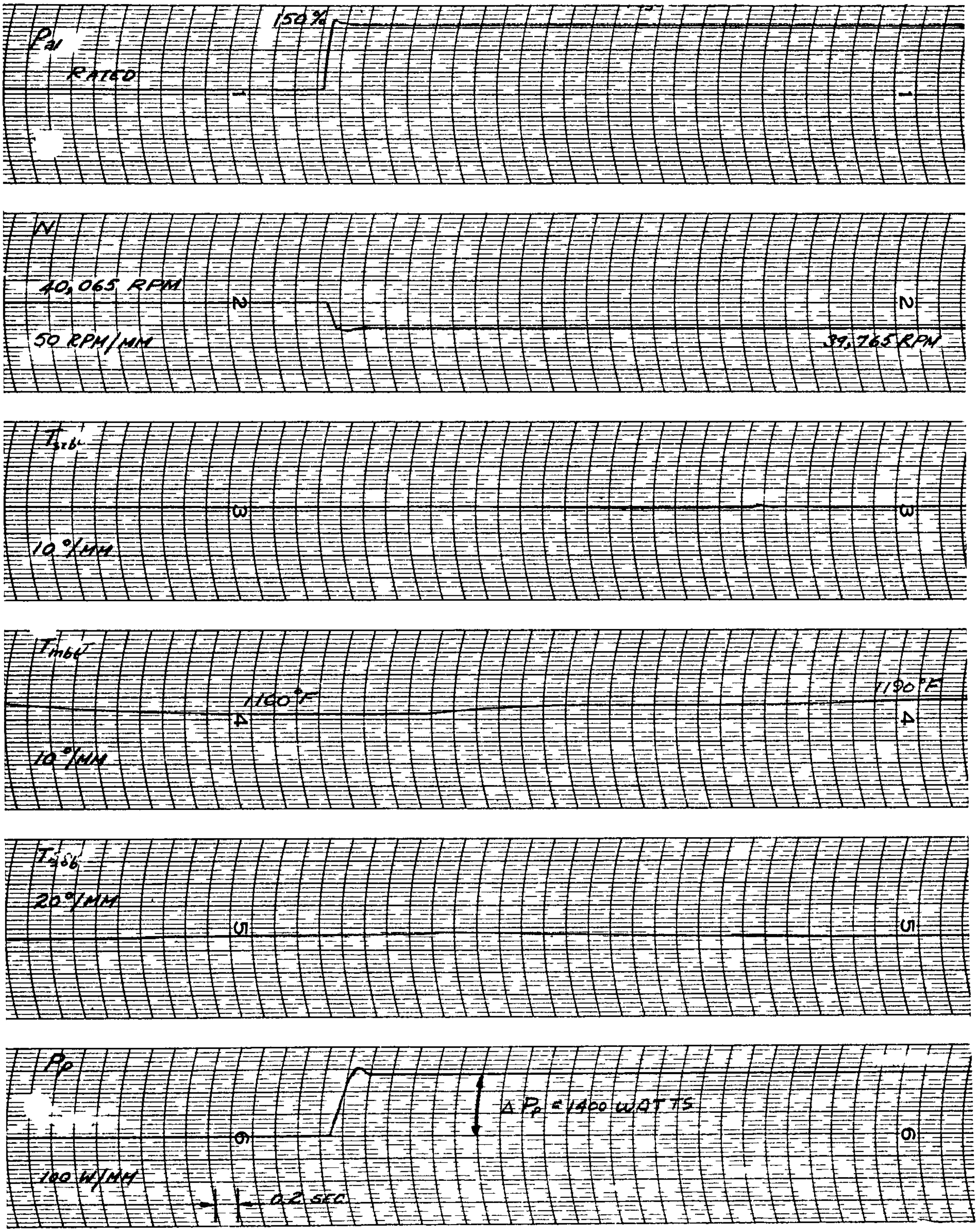

FIG 42 CONTROL ANALYSIS $\frac{P_{(s)}}{N(s)} = \frac{4.65}{(1+.025)^2}$ $\frac{\text{WATTS}}{\text{RPM}}$

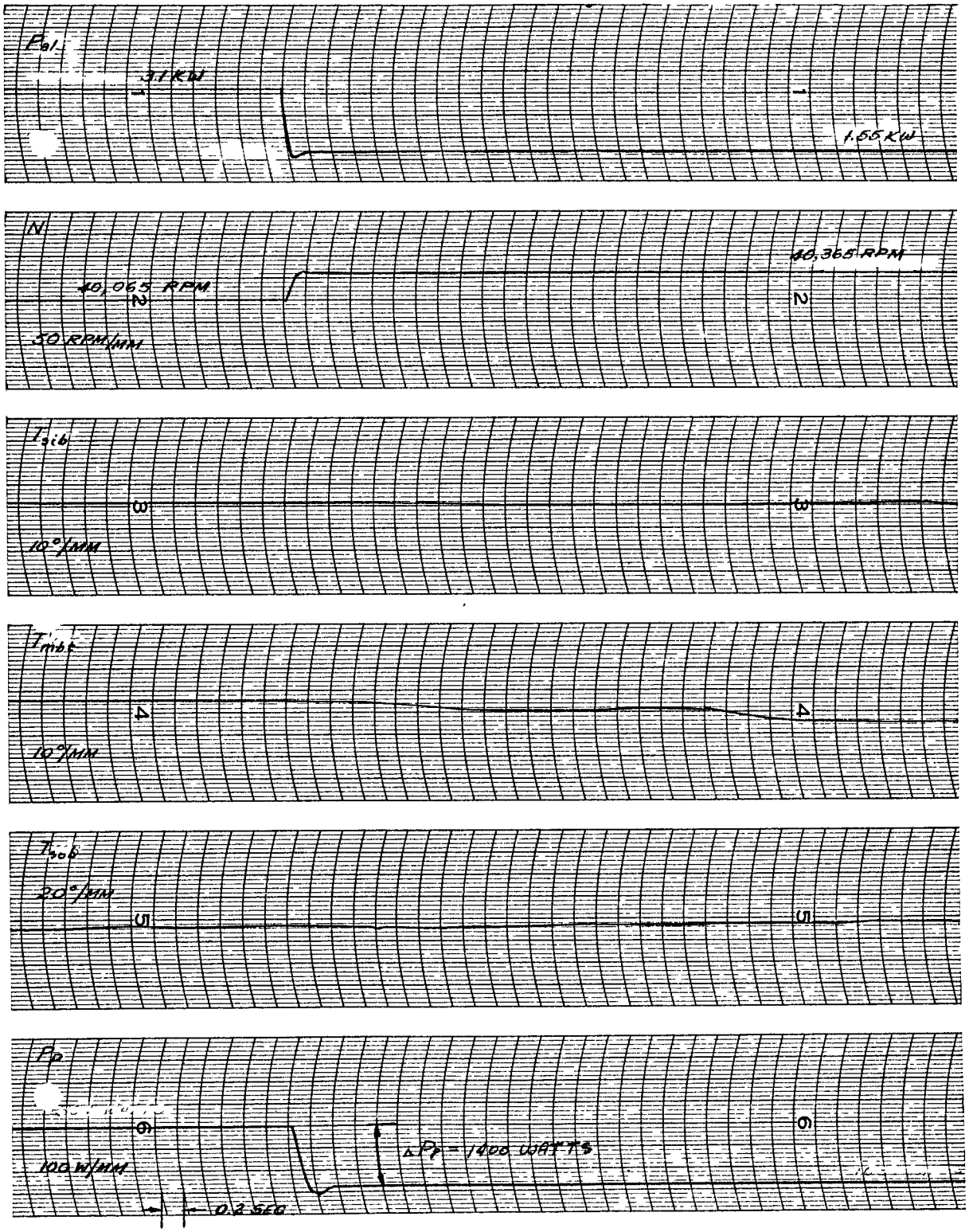

FIG 43 CONTROL ANALYSIS $\frac{P_B N}{N(\omega)} = \frac{4.65}{(1+.025)^2} \frac{\text{WATTS}}{\text{RPM}}$

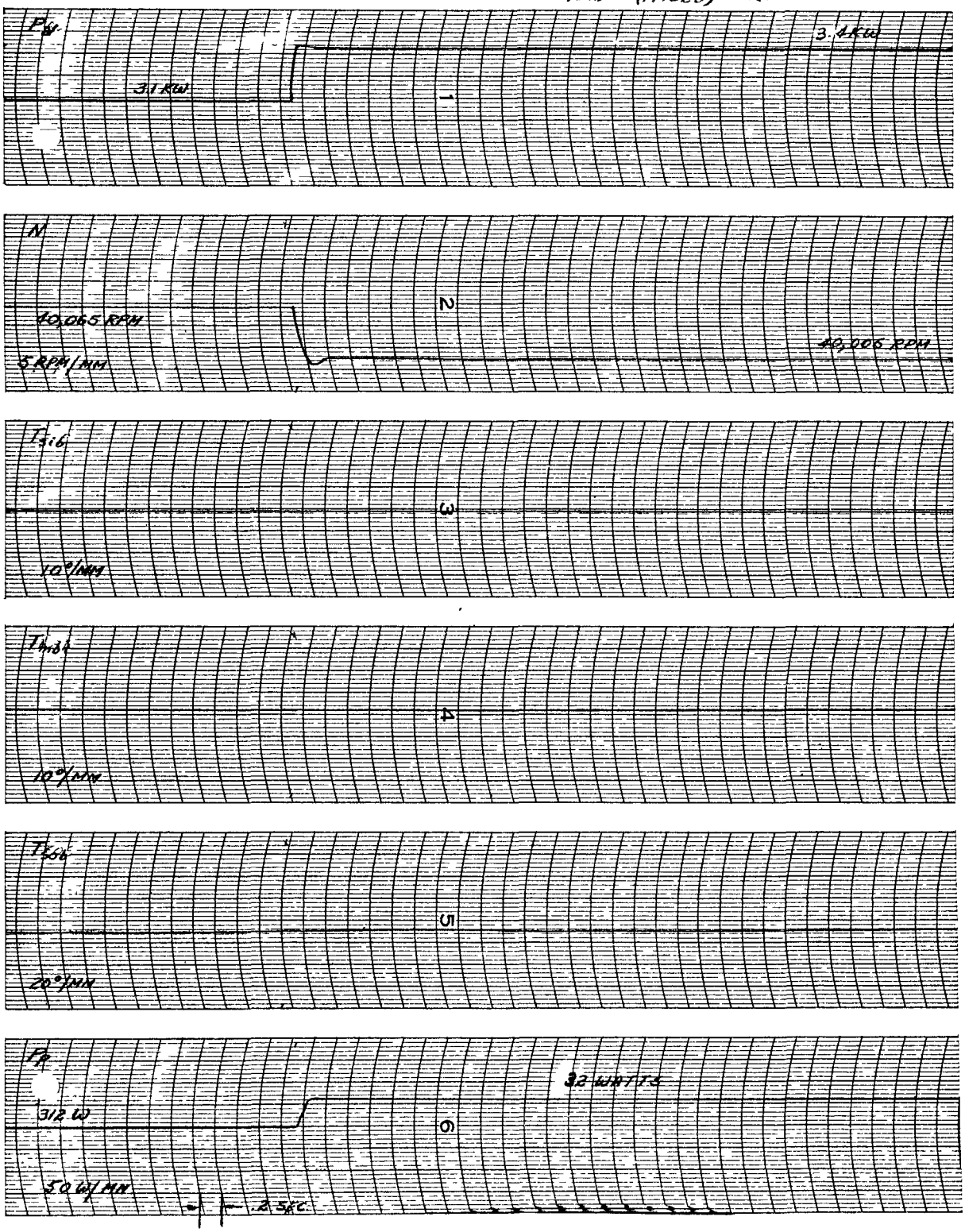

FIG 44 CONTROL ANALYSIS $\frac{P_{2(s)}}{N(s)} = \frac{4.65 \text{ watts}}{(1+.025)^2 \text{ RPM}}$

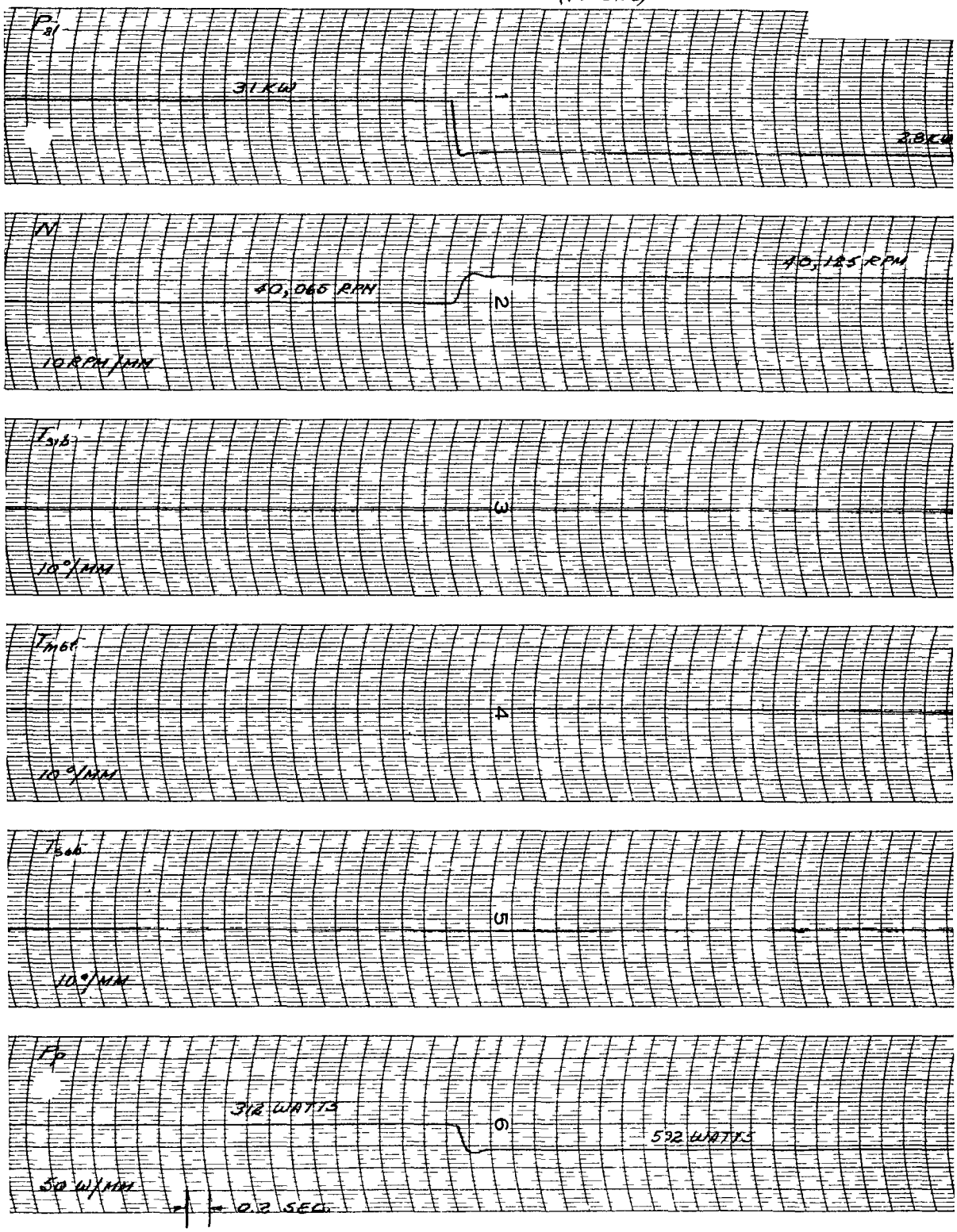

FIG 45 CONTROL ANALYSIS $\frac{P_{el}(s)}{N(s)} = \frac{10}{(1+.02S)^2}$ $\frac{WATTS}{RPM}$

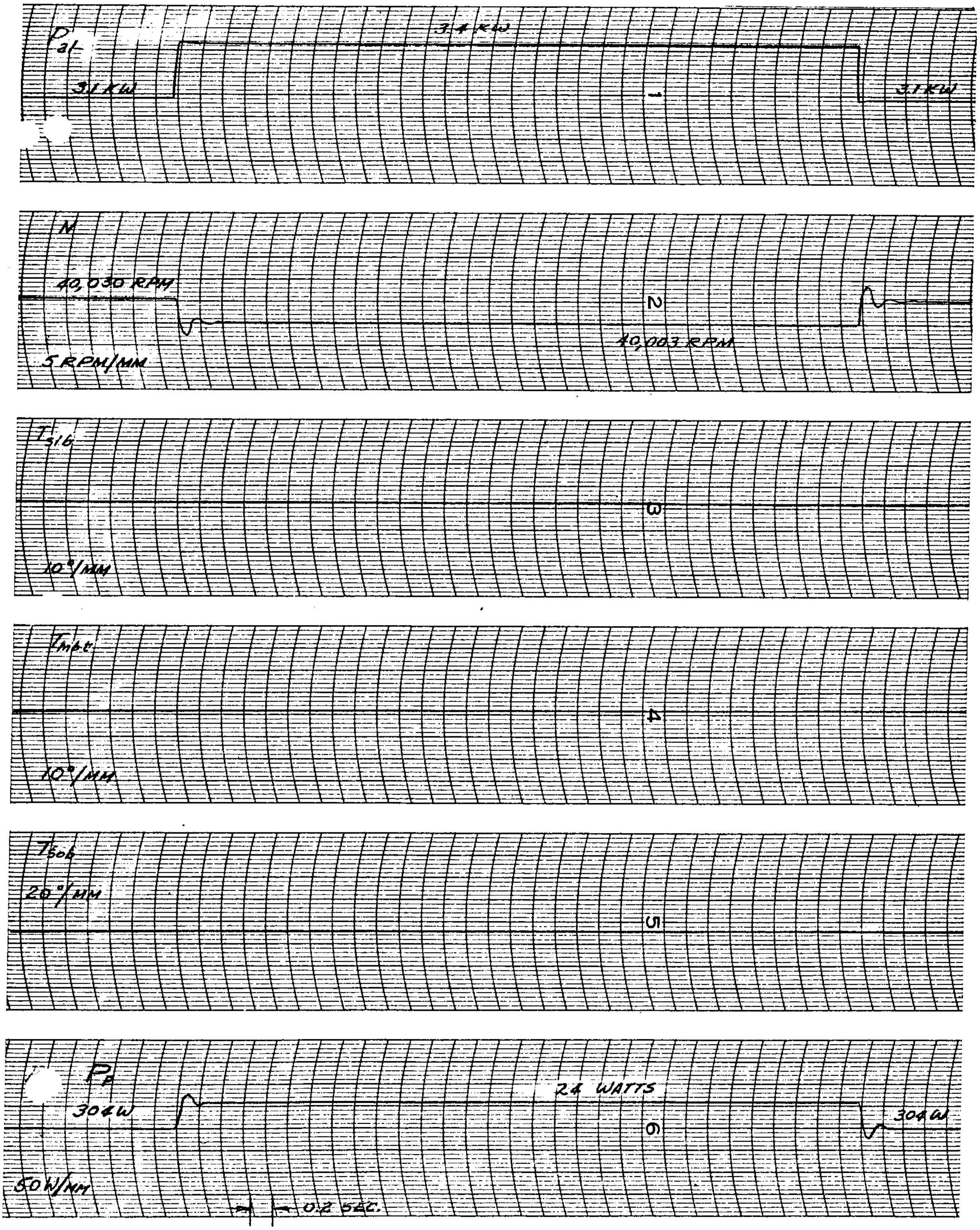

FIG 46

REACTOR RUNS
VARY T_{SOB}; W_S = CONSTANT

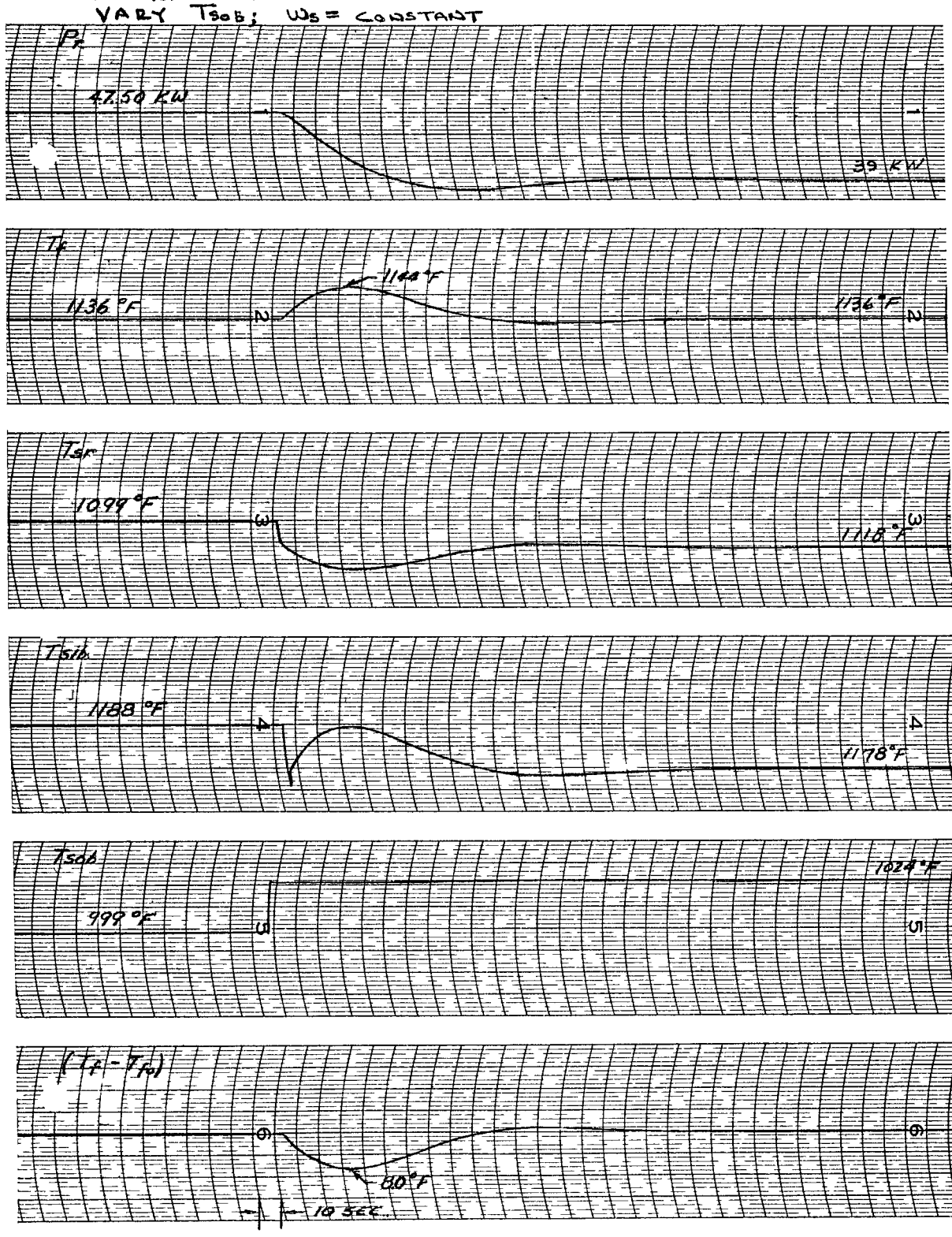

FIG 47

REACTOR RUNS
VARY T_{sob}; W_s = CONSTANT

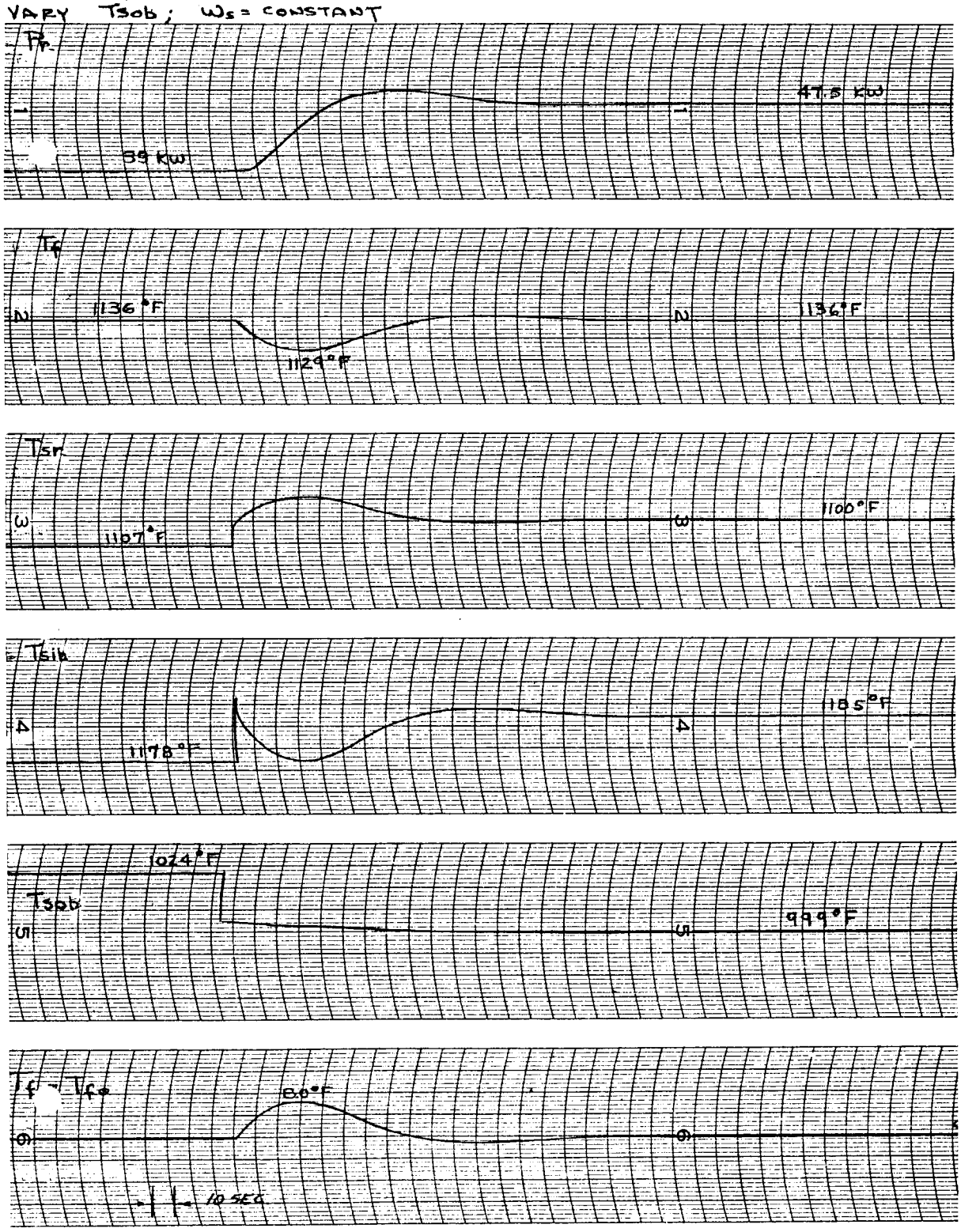

FIG 48

REACTOR RUNS
VARY T_{SOB} ; W_S = CONSTANT

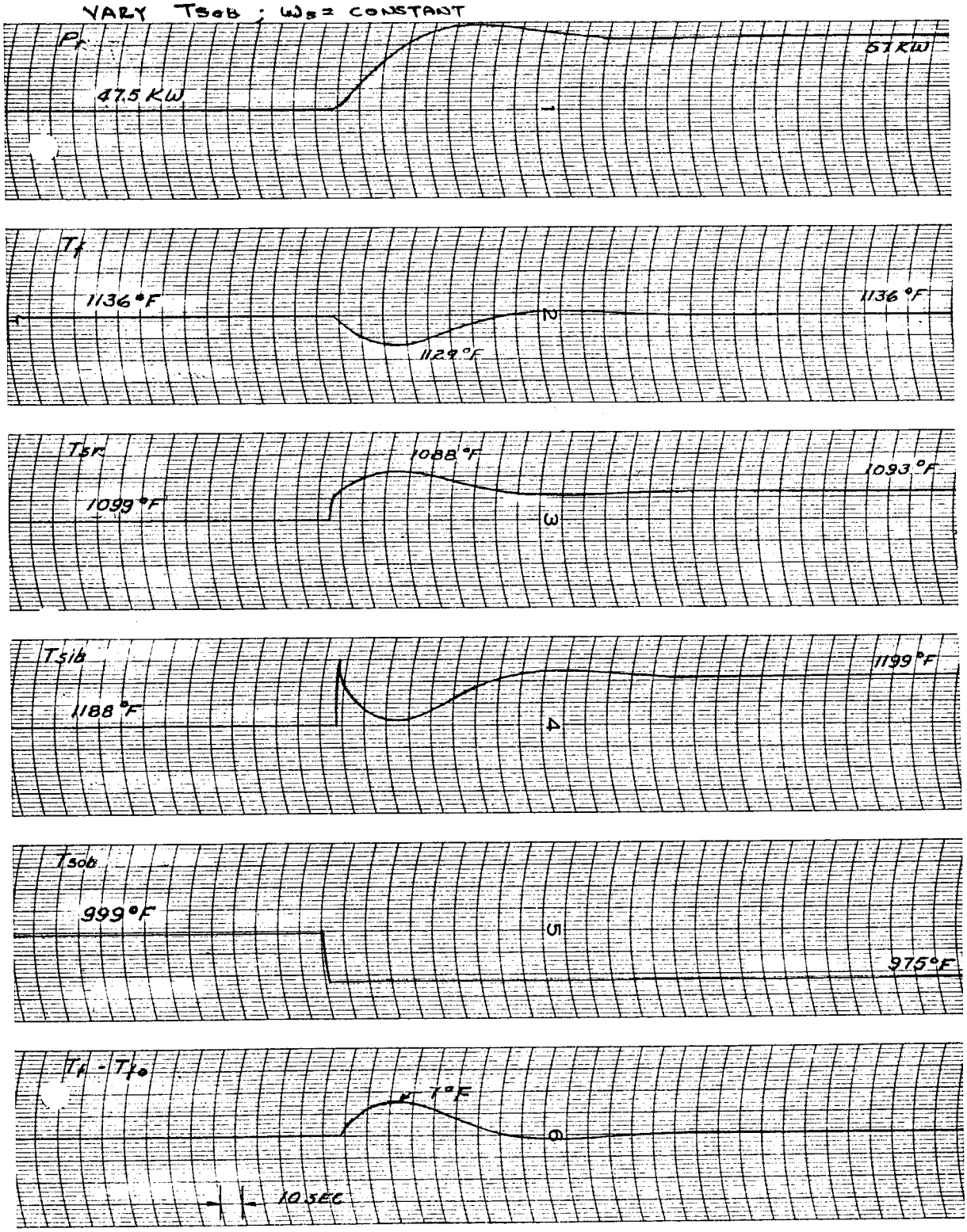

FIG 49

REACTOR RUNS
VARY T_{sob}; W_s = CONSTANT

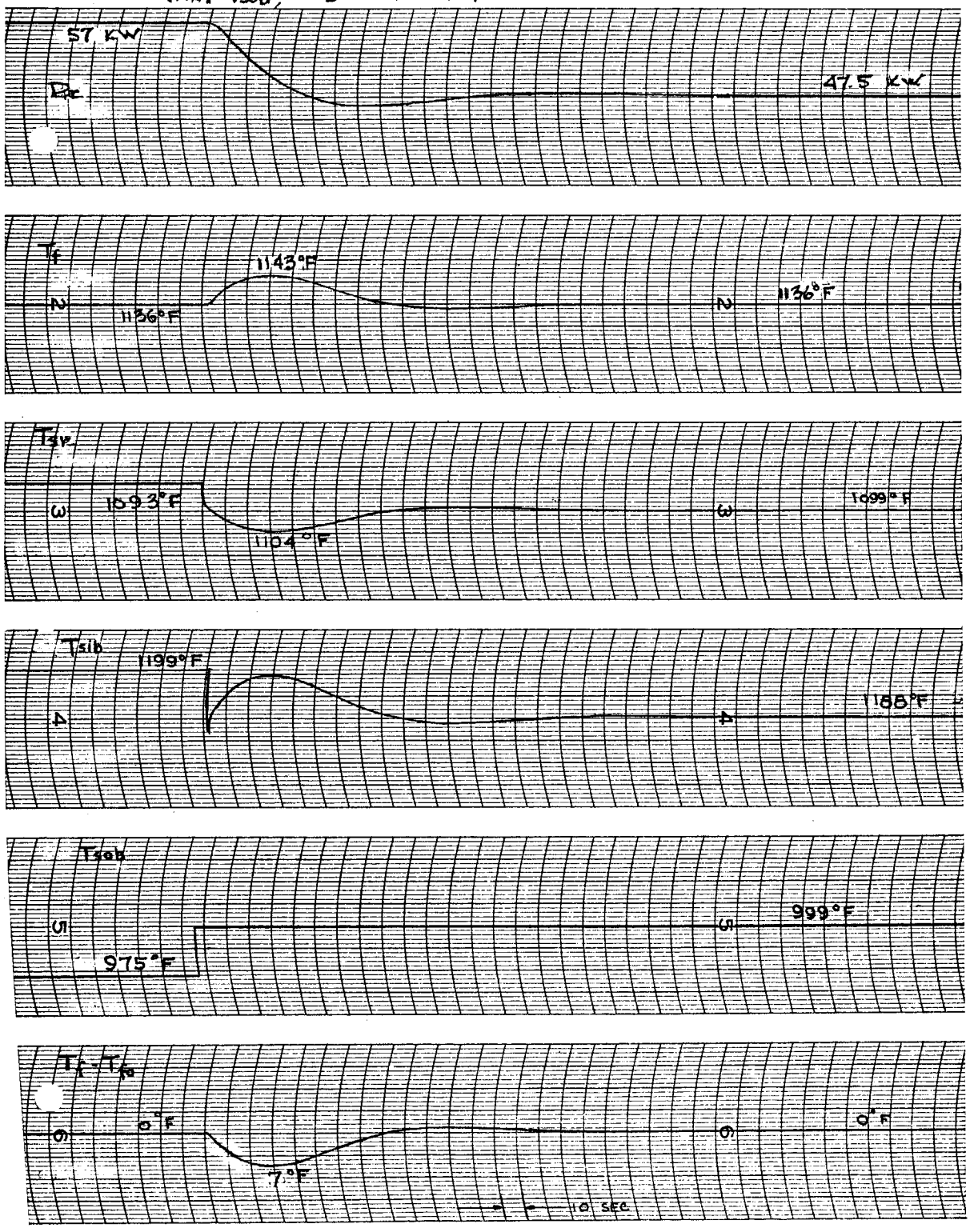

FIGURE 50 a POWER TRANSIENTS

RAMP IN P_n

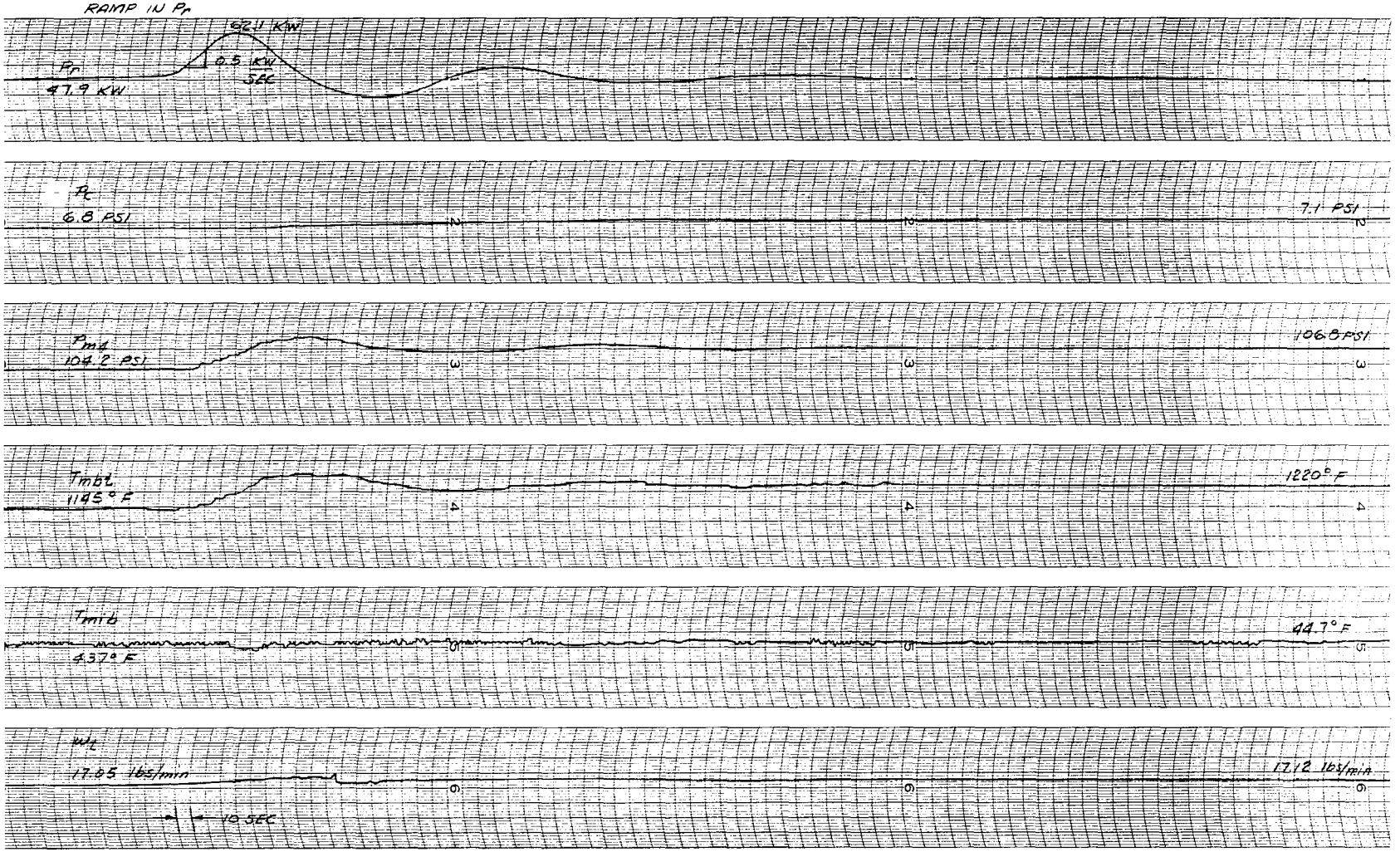

FIGURE 50b POWER TRANSIENTS

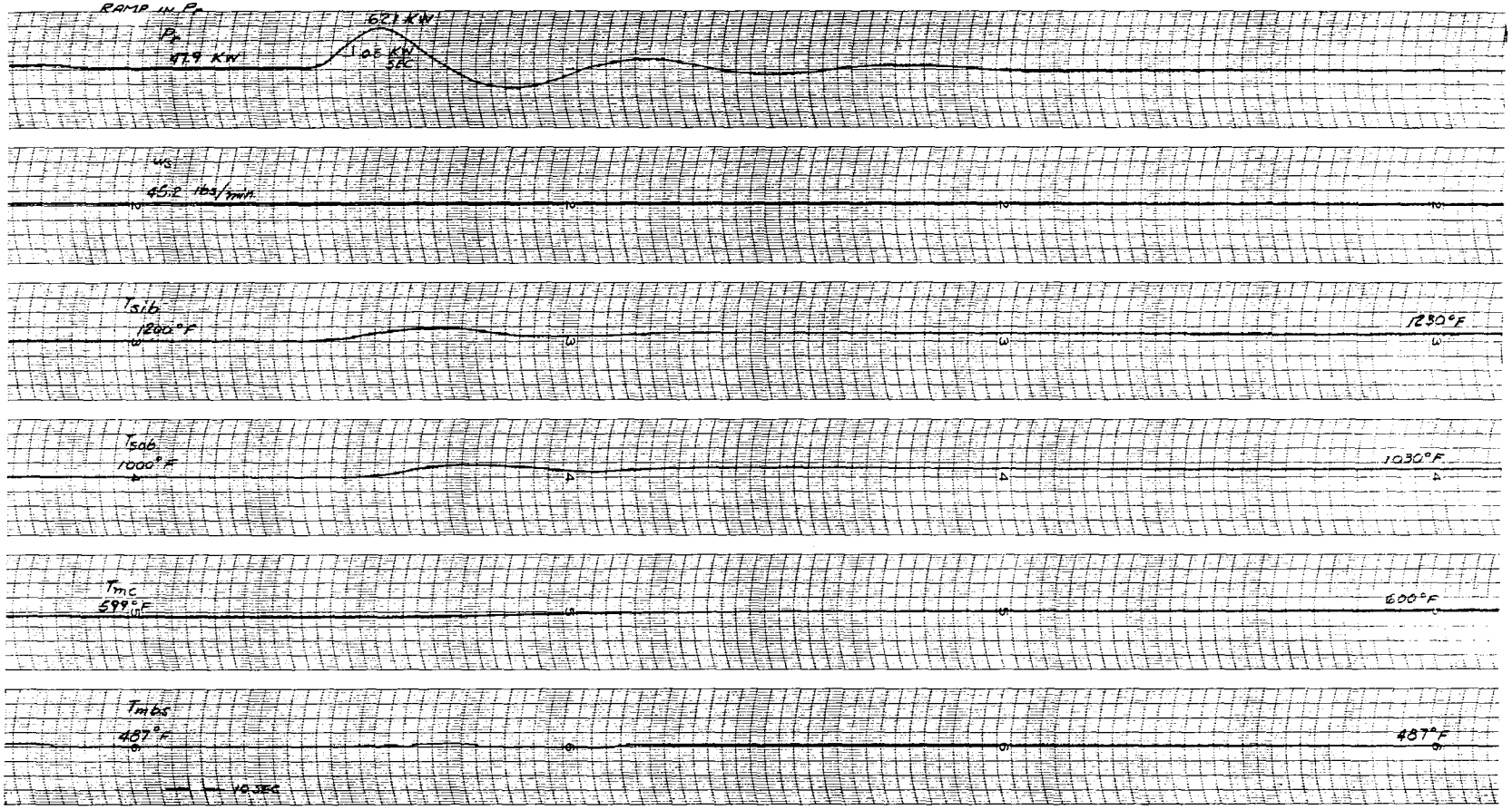

FIGURE 50c POWER TRANSIENTS

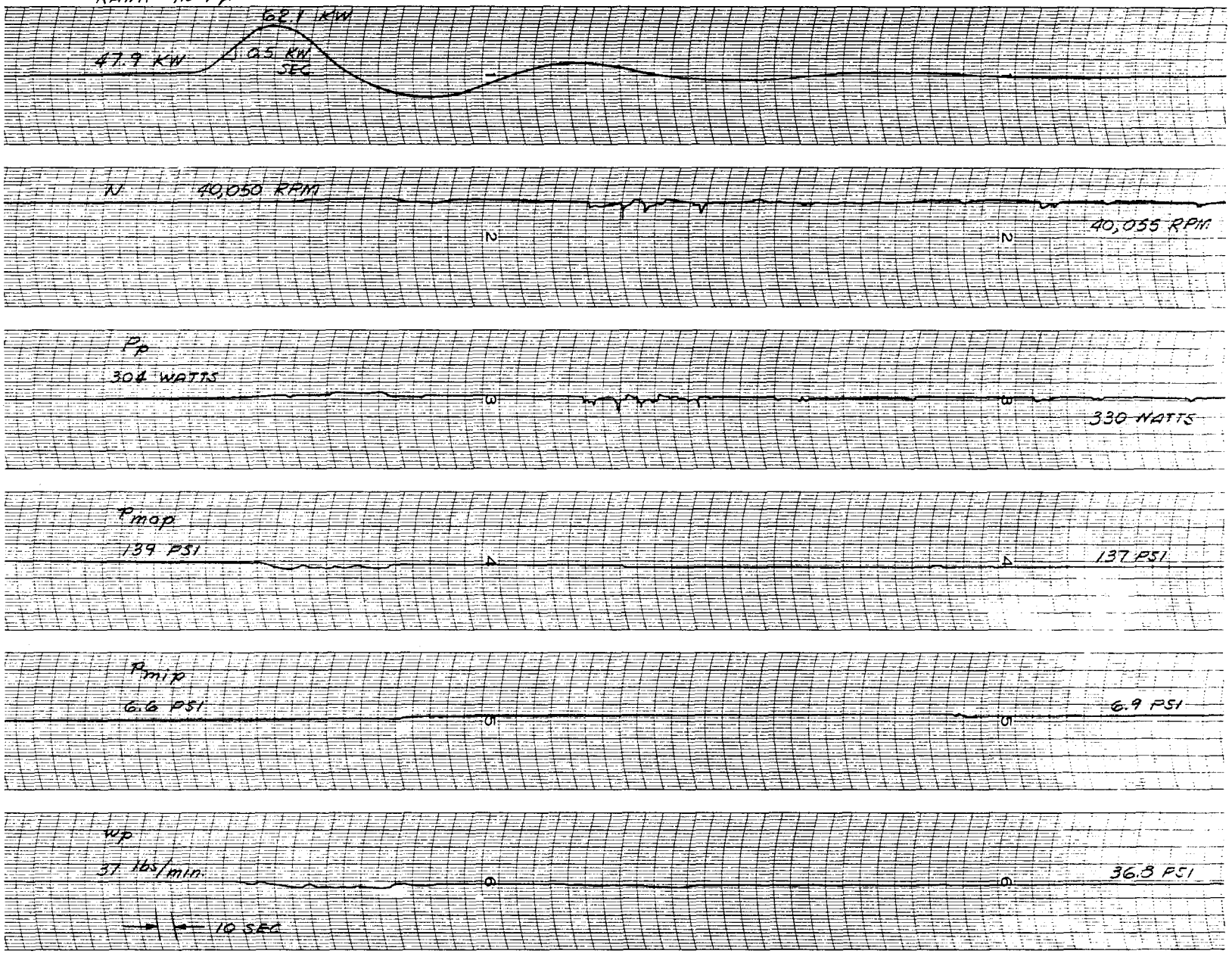

FIG 51a PUMP FLOW TRANSIENTS

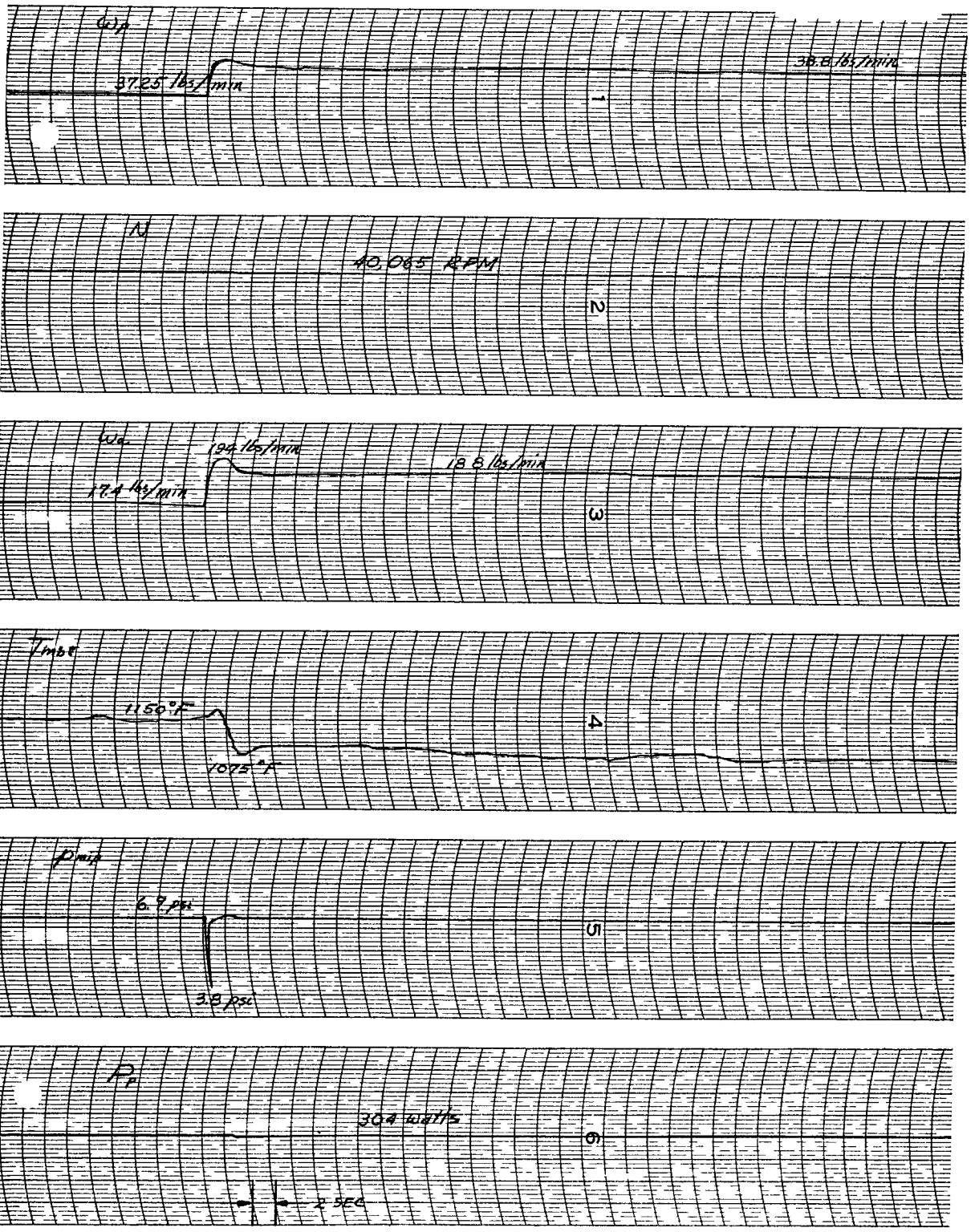

FIG 516 PUMP FLOW TRANSIENTS

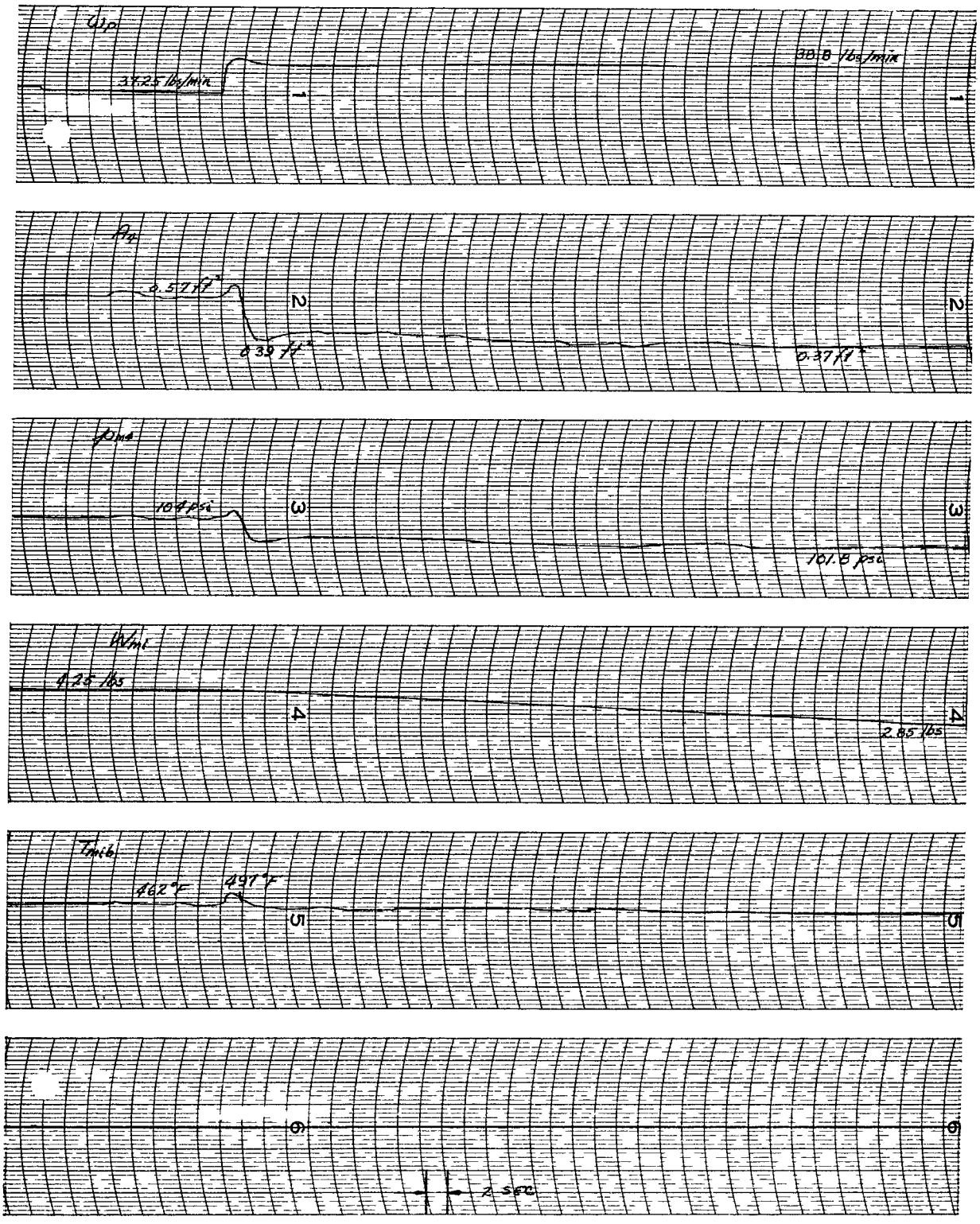

FIG 52a PUMP FLOW TRANSIENTS

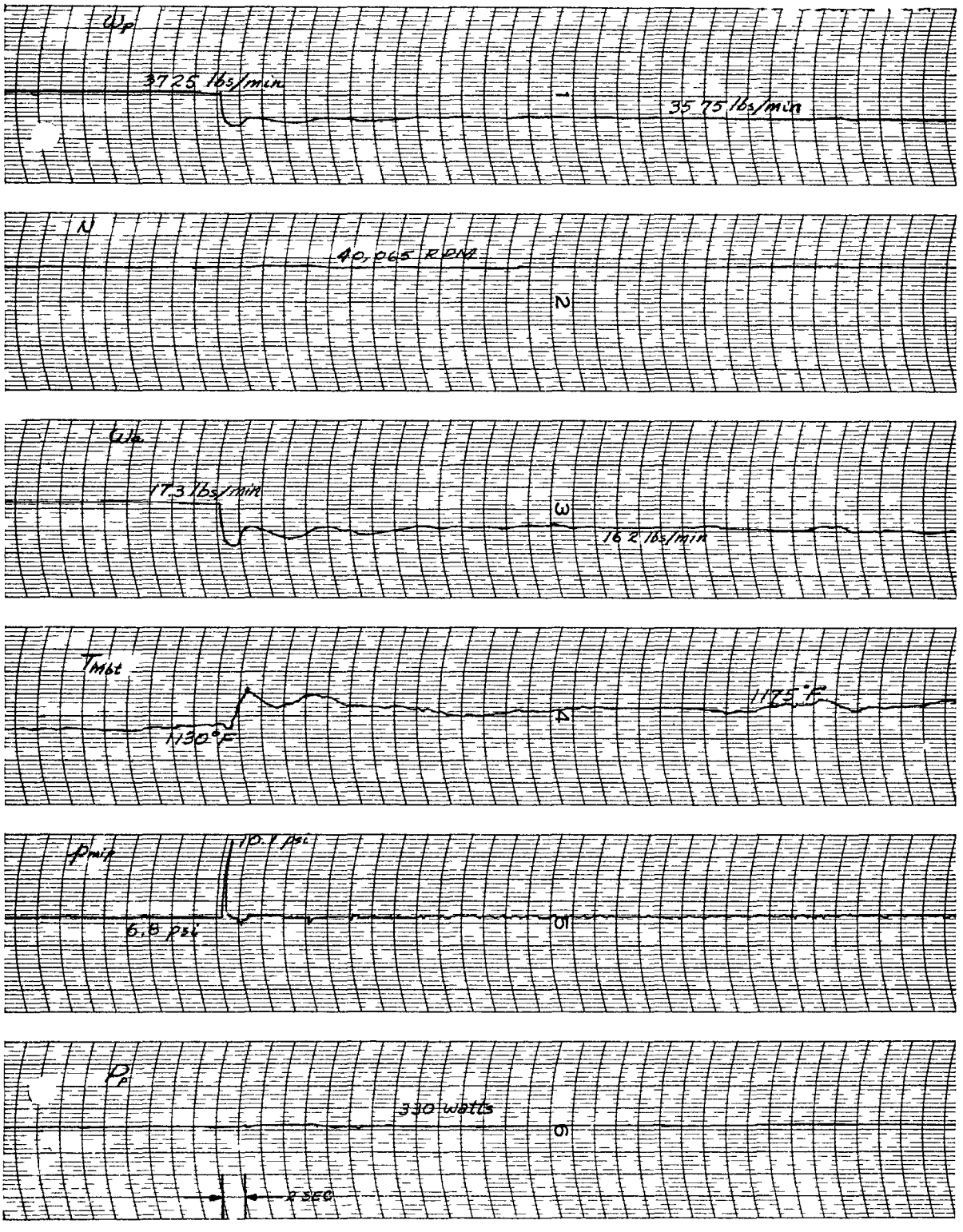

FIG 526 PUMP FLOW TRANSIENTS

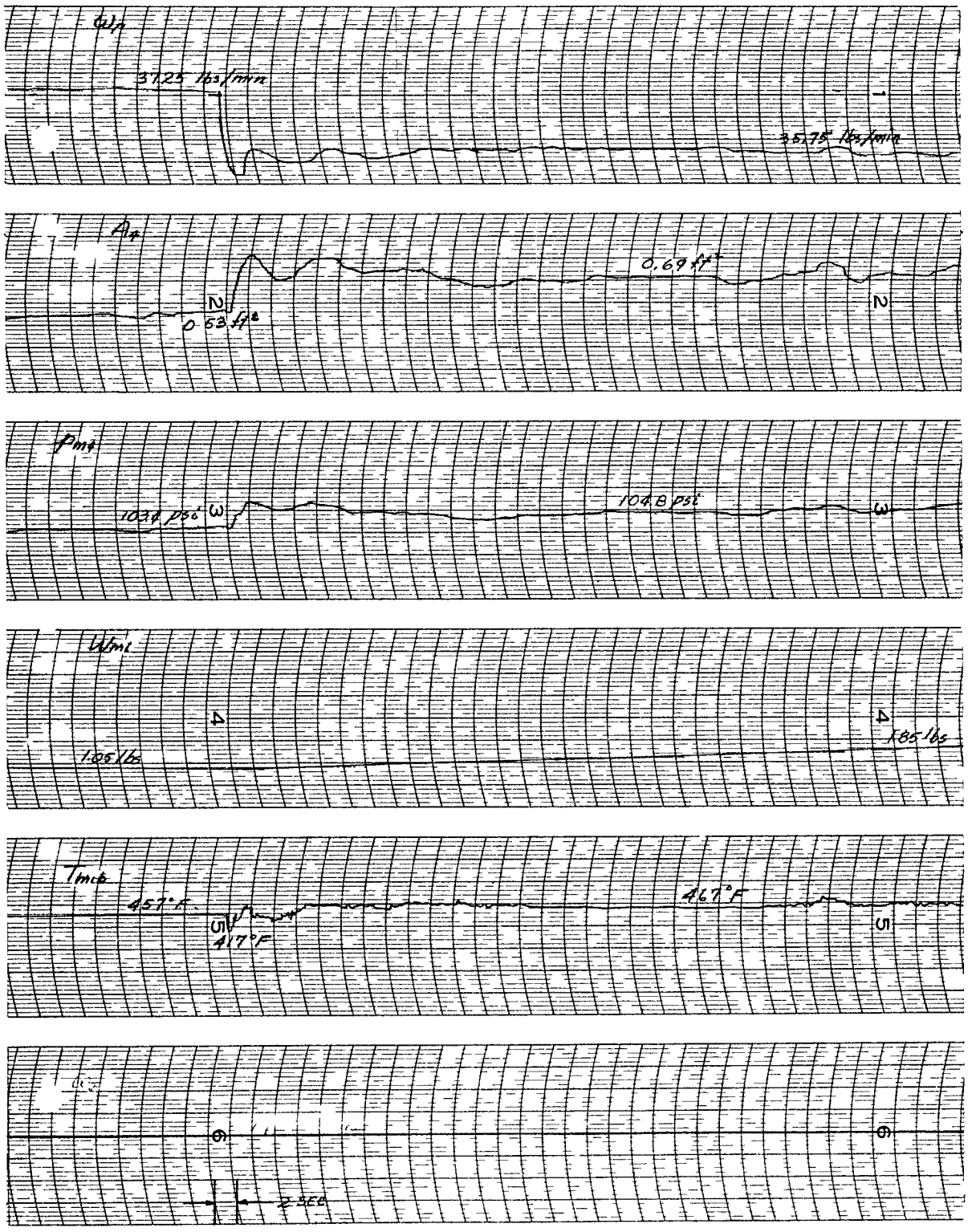

FIG 58a - BEARING FLOW TRANSIENTS

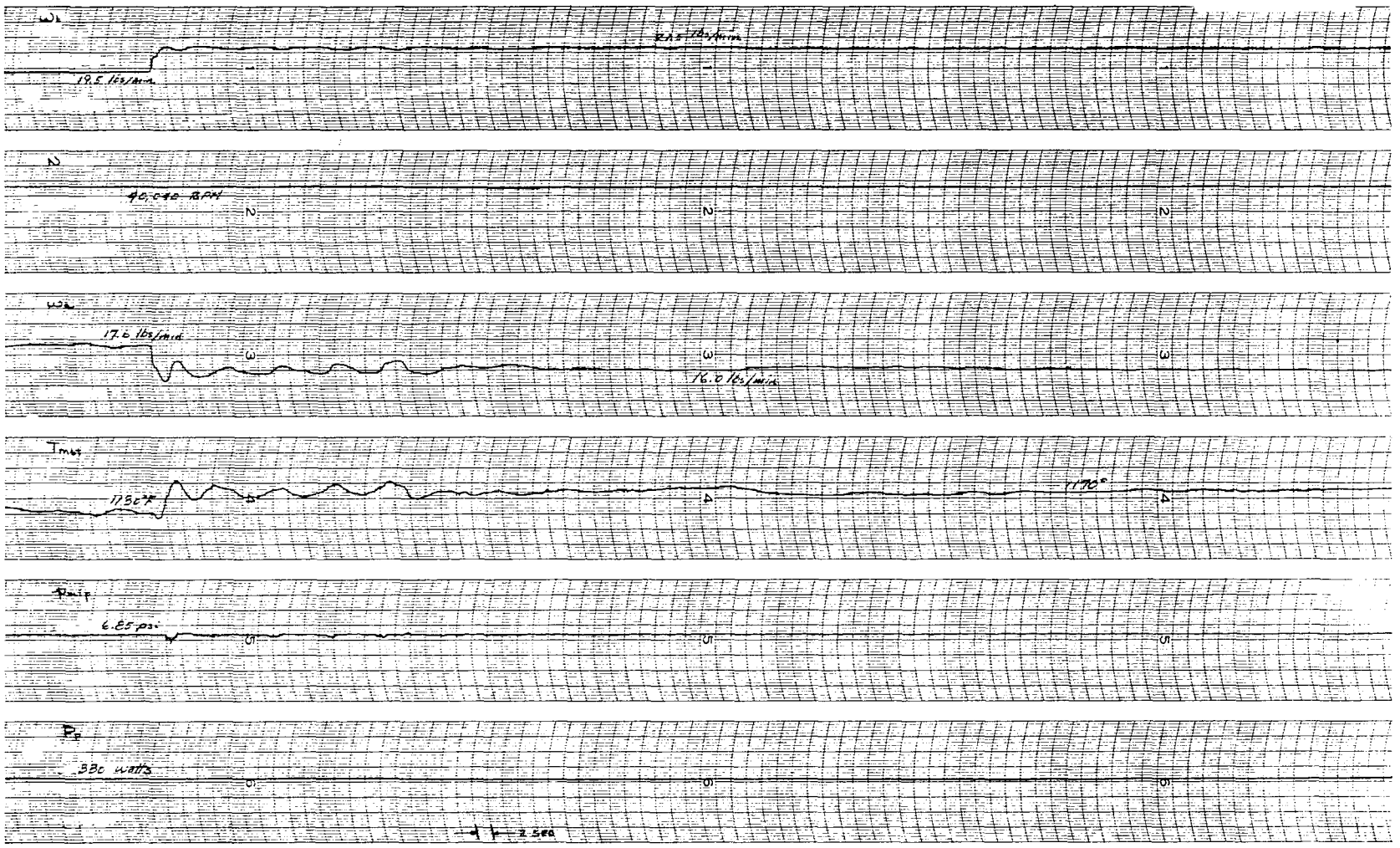

FIG 5B.6 - BEARING FLOW TRANSIENTS

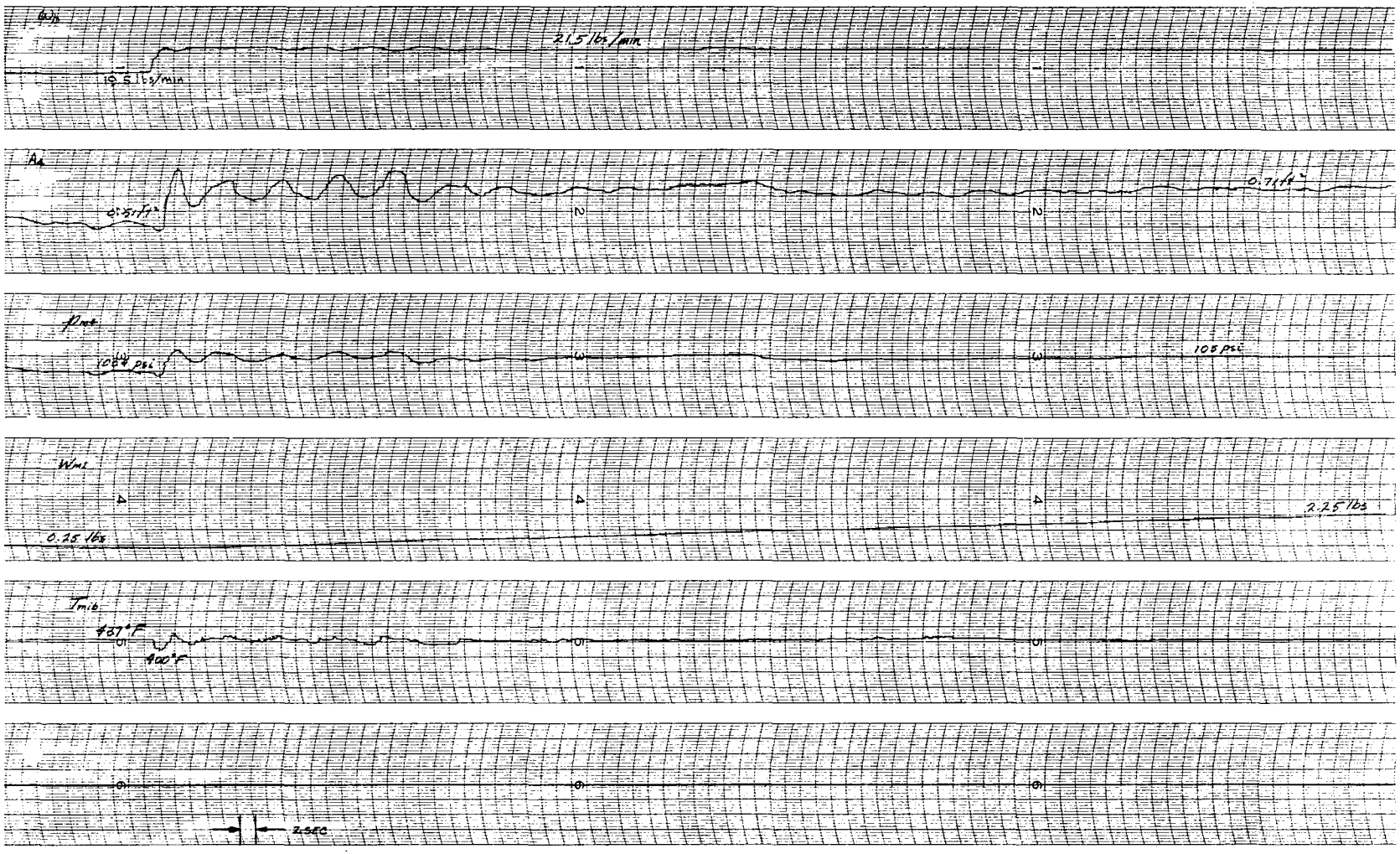

FIG 54a BEARING FLOW TRANSIENTS

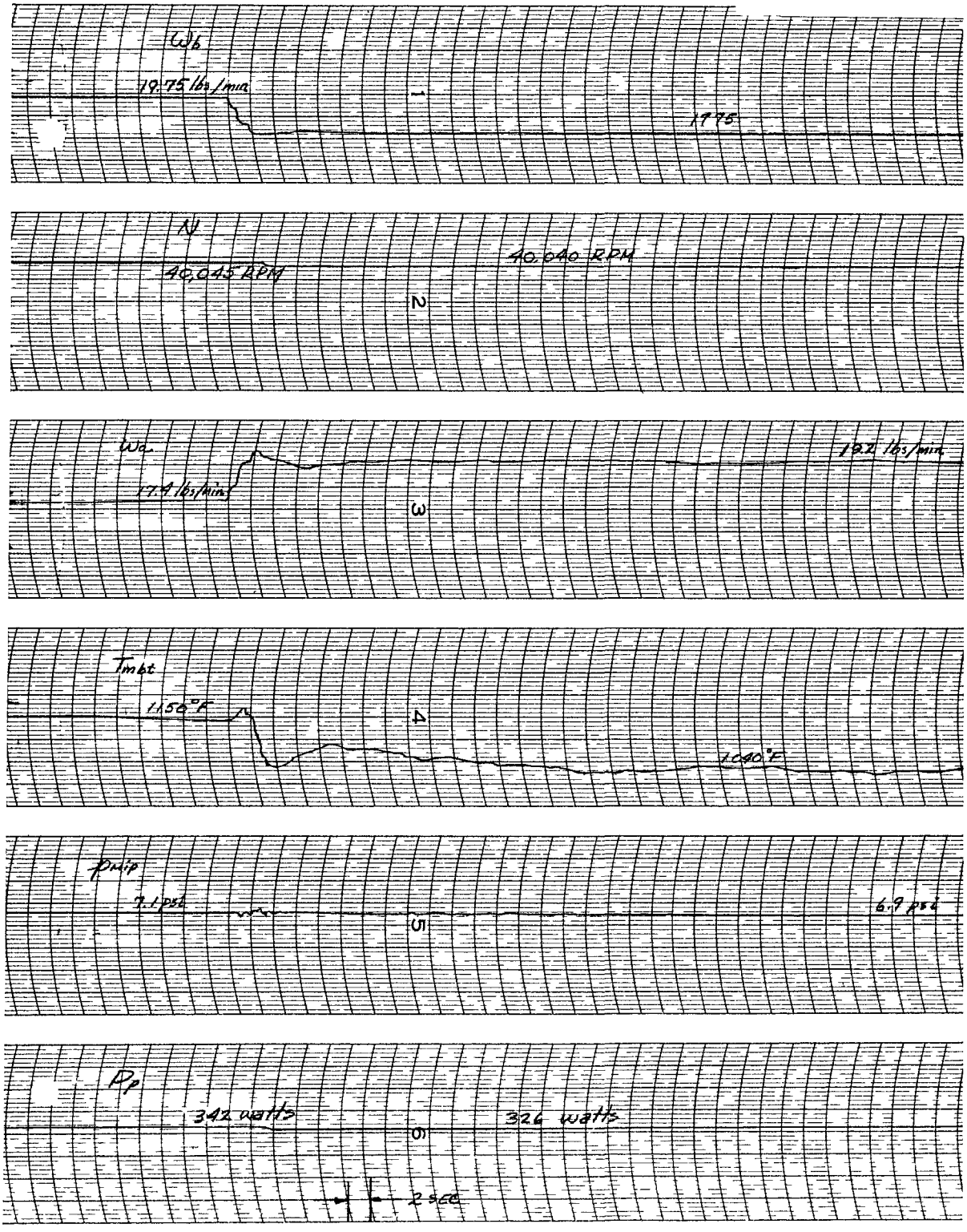

FIG 546 BEARING FLOW TRANSIENTS

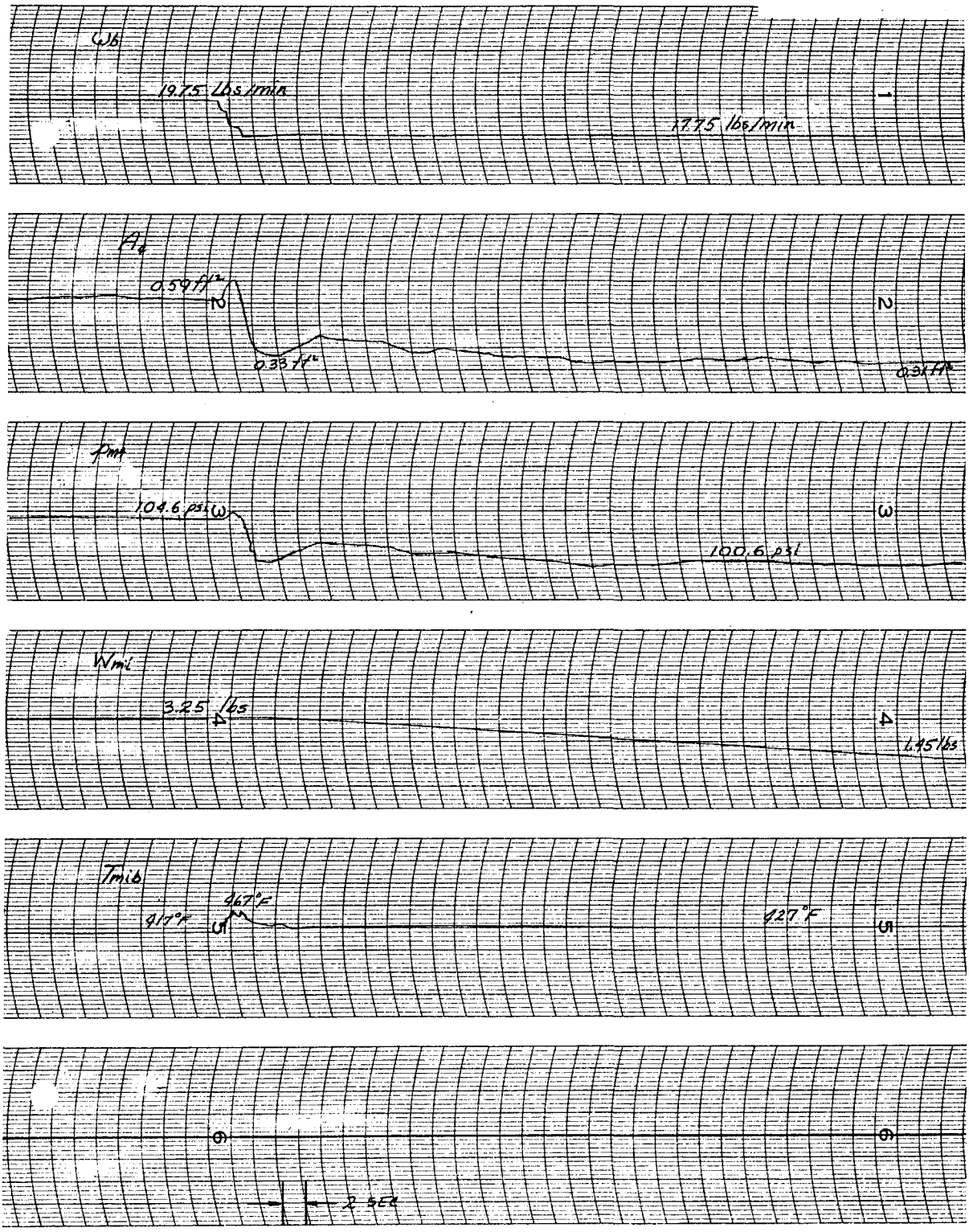

FIGURE 55 a SUN-SHADE OPERATION

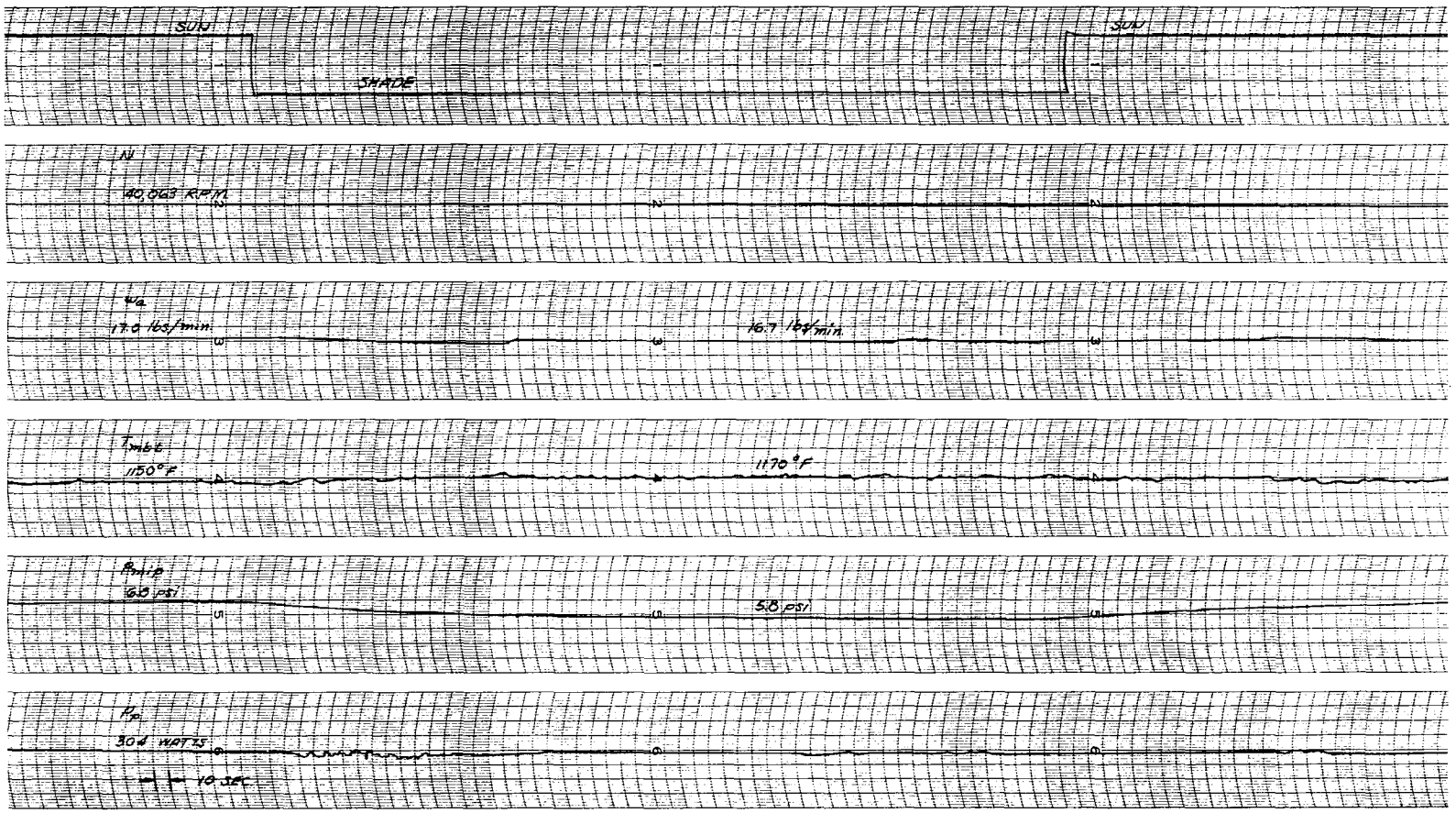

FIGURE 55b SUN-SHADE OPERATION

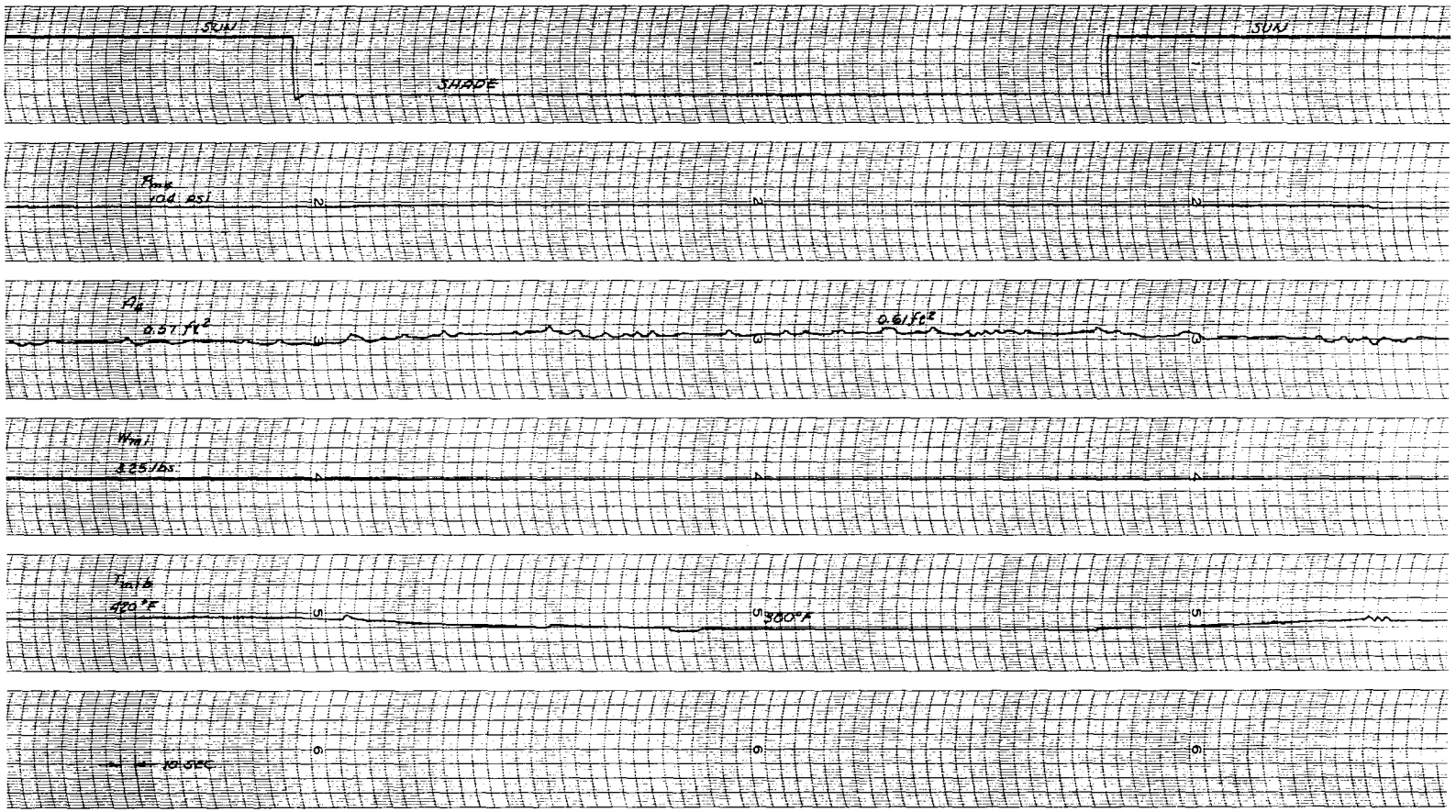

TABLE 1 - SYMBOLS-VARIABLES

A_c	-	Area, condenser
A_i	-	Area, intercooler
A_2	-	Area, preheater
A_3	-	Area, boiling section
A_4	-	Area, superheater
C	-	Spouting velocity, turbine
E	-	Output of alternator
h_i	-	Enthalpy, inlet to turbine
h_t	-	Enthalpy, mercury leaving turbine
Δh_i	-	Enthalpy drop across turbine, ideal
I_l	-	Current, load
l_3	-	Length, boiling section
N	-	Speed, rotating unit
P_a	-	Power, input to alternator
P_{al}	-	Power, useful load
P_b	-	Power, input to bearings
P_c	-	Power, losses in alternator
P_{mph}	-	Power, output of mercury pump
P_{mpt}	-	Power, input to mercury pump
P_p	-	Power, parasitic load
P_r	-	Power, reactor output

P_{spt} - Power, input to sodium pump

P_t - Power, output of turbine

P_c - Pressure, condenser

P_{ma} - Pressure, acceleration of mercury loop

P_{mh} - Pressure, mercury pump head

P_{mip} - Pressure, mercury into pump

P_{mop} - Pressure, mercury out of pump

P_{ms} - Pressure, mercury loop

P_{m23} - Pressure, mercury entering boiling system

P_{m24} - Pressure, mercury entering superheater

P_{m4} - Pressure, mercury in superheater

P_{sa} - Pressure, acceleration of sodium loop

P_{sh} - Pressure, sodium pump head

P_{ss} - Pressure, sodium loop

P_2 - Pressure, mercury in preheater

T_f - Temperature, reactor fuel mean

T_c - Temperature, condenser

T_i - Temperature, intercooler

T_{mbs} - Temperature, mercury bearings to subcooler

T_{mc} - Temperature, mercury in condenser

T_{mi} - Temperature, mercury in intercooler

T_{mib} - Temperature, mercury into heat exchanger

T_{mis} - Temperature, mercury intercooler to subcooler

T_{mbt} - Temperature, mercury heat exchanger to turbine

T_{ms} - Temperature, mercury in subcooler

T_{msp} - Temperature, mercury subcooler to pump

T_{m2} - Temperature, mercury in preheater

T_{m23} - Temperature, mercury preheater to boiling section

T_{m34} - Temperature, mercury boiling section to superheater

T_{m4} - Temperature, mercury in superheater

T_s - Temperature, subcooler

T_{slb} - Temperature, sodium into heat exchanger

T_{slr} - Temperature, sodium into reactor

T_{sob} - Temperature, sodium out of heat exchanger

T_{sor} - Temperature, sodium out of reactor

T_{sr} - Temperature, sodium average, reactor

T_{s2} - Temperature, sodium in preheater

T_{s32} - Temperature, sodium boiling section to preheater

T_{s3} - Temperature, sodium in boiling section

T_{s43} - Temperature, sodium superheater to boiling section

T_{s4} - Temperature, sodium in superheater

U_3 - Heat transfer coefficient, boiling section

u - Pitch velocity, turbine wheel

V_c - Volume, condenser

V_i - Volume, intercooler

V_{m2} - Volume, mercury in preheater

V_{m3} - Volume, mercury in boiling section

V_{m4} - Volume, mercury in superheater

V_{s2} - Volume, sodium in preheater

V_{s3} - Volume, sodium in boiling section

V_{s4} - Volume, sodium in superheater

W_{mc} - Weight, mercury in condenser

W_{mi} - Weight, mercury in intercooler

W_{m2} - Weight, mercury in preheater

W_{m3} - Weight, mercury in boiling section

W_{m4} - Weight, mercury in superheater

$W_c C_c$ - Heat capacity, condenser

$W_i C_i$ - Heat capacity, intercooler

$W_{s2} C_{s2}$ - Heat capacity, preheater

$W_{s3} C_{s3}$ - Heat capacity, boiling section

$W_{s4} C_{s4}$ - Heat capacity, superheater

δ_k - Reactivity

η - Efficiency, turbine

ρ_{mc} - Specific weight, mercury in condenser

w_a - Flow, mercury to heat exchanger

w_b - Flow, mercury to bearings

w_c - Flow, mercury out of condenser

w_i - Flow, mercury out of intercooler

w_p - Flow, mercury through pump

w_s - Flow, sodium

w_t - Flow, mercury through turbine

w_2 - Flow, mercury into boiling section

w_3 - Flow, mercury into superheater

w_4 - Flow, mercury out of superheater

γ - Speed ratio, turbine

TABLE 2 SYMBOLS-CONSTANTS

A_{bc}	-	Area, boiler cross-section - 0.875×10^{-3} ft^2
†A_{fs}	-	Area, fuel to sodium heat transfer - ft^2
A_s	-	Area, subcooler - 2.97 ft^2
A_{tr}	-	Area, condenser plus intercooler - 75.5 ft^2
A_t	-	Area, heat exchanger heat transfer - 5.235 ft^2
†C_f	-	Specific heat, fin of intercooler plus condenser - 0.226 btu/lb-°F
C_{fs}	-	Specific heat, fin of subcooler - 0.226 btu/lb-°F
C_m	-	Specific heat, liquid mercury - 0.0326 btu/lb-°F
C_{m_4}	-	Specific heat, gaseous mercury - 0.0251 btu/lb -°F
C_s	-	Specific heat, sodium - 0.301 btu/lb-°F
C_w	-	Specific heat, walls of heat exchanger - 0.118 btu/lb-°F
C_{ws}	-	Specific heat, wall of subcooler - 0.118 btu/lb-°F
C_{w_2}	-	Specific heat, walls of intercooler plus condenser - 0.118 btu/lb-°F
C_f	-	Specific heat, fuel - btu/lb-°F
d	-	Diameter, inside of mercury tube in heat exchanger - 0.033 ft
E_{ff}	-	Fin efficiency - 93.8%
e	-	Emissivity - 0.9
e_s	-	Efficiency, sodium pump - 5.5%
g	-	Gravitational constant - 116×10^3 ft/min^2
h_{fg}	-	Heat of vaporization, mercury - 123.3 btu/lb
h_g	-	Enthalpy, saturated mercury vapor - 153.3 btu/lb

I - Moment of Inertia, rotating parts - 2.06495 lb-in^2

J - Joules equivalent - 778 ft lbs/btu

‡ K_a - Constant, alternator proportionality - volts^2/rpm^2 - lines

K_b - Constant, bearing line flow - 0.151 in^2/min

K_c - Constant, bearing power - 0.375×10^{-9} kw/rpm^2

K_l - Constant, alternator loss - 0.4875×10^{-9} kw/rpm^2

K_{ma} - Constant, acceleration of mercury loop - 0.0555 in^2/sec^2

K_{mp1} - Constant, mercury pump power - 0.0924×10^{-12} ft/rpm^3

K_{mp2} - Constant, mercury pump power - 103.5×10^{-12} ft lbs/ min-rpm^3

K_r - Constant, rotor power - 2.84×10^{-5}/rpm^2 - in

K_{sa} - Constant, acceleration of sodium loop - 0.753 in^2/sec^2

K_{ss} - Constant, pressure loss of sodium loop - 5.29 sec^2/in^2 -lb

K_{sh} - Constant, sodium pump head pressure - 0.1875×10^{-8} lb/in^2-rpm^2

K_{t1} - Constant, turbine speed ratio - 0.435×10^{-2} sec $\left(\frac{\text{btu}}{\text{lb}}\right)^{1/2}$

K_{t2} - Constant, turbine design - 6.5 in^2 $^\circ$R$^{1/2}$ /min

K_{t3} - Constant, turbine power - 0.0175 min-kw/btu

K - Control loop setting - 4.65 watts/rpm

K_v - Constant, boiler dimensions 33.6×10^{-3} /ft

K_1 - Constant, low pressure acceleration, mercury loop - 0.0583 in^2/sec^2

K_2 - Constant, high pressure acceleration, mercury loop - 1.14 in^2/sec^2

l^* - Mean effective lifetime - 10^{-5} sec

N_r - Speed reference - 40,000 rpm

P_i - Power loss, incident - 2.72 btu/min - ft^2

P_l - Power loss, heat exchanger - 284 btu/min

R - Gas constant, mercury - 7.7 ft-lb/lb-°R

T_{fo} - Temperature, reactor fuel reference - 1136.8 °F

†U_{fs} - Heat transfer coefficient, fuel to sodium - btu/°F-ft^2-min

U_2 - Heat transfer coefficient, preheater - 4.32 btu/°F-ft^2-min

U_4 - Heat transfer coefficient, superheater - 1.075 btu/°F-ft^2-min

V_{mt} - Volume, mercury in heat exchanger - 0.035 ft^3

V_s - Volume, sodium in heat exchanger 0.3 ft^3

V_t - Volume, intercooler plus condenser - 0.276 ft^3

v_f - Specific volume, mercury saturated liquid - 1.18×10^{-3} ft^3/lb

v_{fg} - Specific volume, difference ($v_g - v_f$) - 0.764 ft^3/lb

v_g - Specific volume, mercury, saturated vapor - 0.764 ft^3/lb

v_m - Specific volume, liquid mercury - 1.18×10^{-3} ft^3/lb

v_s - Specific volume, sodium - 0.0189 ft^3/lb

W_f - Weight, fins of intercooler and condenser - 106 lb

W_{fs} - Weight, fin of subcooler - 4.17 lb

W_{ms} - Weight, mercury in subcooler - 3.22 lb

W_s - Weight, sodium in heat exchanger - 16 lb

†W_{sr} - Weight, sodium in reactor - lbs

W_w - Weight, walls of heat exchanger - 11 lb

W_{ws} - Weight, wall of subcooler - 0.78 lb

W_{w_2} - Weight, walls of intercooler and condenser - 25.5 lb

$\ddagger W_f$ - Weight, fuel in reactor - lbs

$W_{su}C_{su}$ - Heat capacity, subcooler - 1.14 btu/°F

α - Temperature coefficient - 5×10^{-5}/°F

β - Neutron ratio - 0.0084

λ - Decay constant of effective neutron - 0.1/sec

σ - Stefan-Boltzmann constant - 0.284×10^{-10} btu/°R-ft^2-min

ρ_m - Specific weight, liquid mercury - 845 lb/ft^3

ρ_{m_4} - Specific weight, gaseous mercury - 1.31 lb/ft^3

$\cos \Theta$ - Power Factor - 0.8

$\ddagger \phi$ - Flux - lines

R_p - Load resistance - 4.65 Ω

$\ddagger$ Lumped Constants

Reactor:

$$\frac{A_{fs}\, U_{fs}}{W_{sr}\, C_s} = 168/\text{min}$$

$W_f C_f = 12.6$ btu/°F

Alternator:

$K_a \phi = 9 \times 10^{-6}$ volts^2/rpm^2

DISTRIBUTION

SNAP II TOPICAL REPORTS

	No. of Copies
Air Force Ballistic Missile Division, Commander Commander, Air Force Ballistic Missile Division Hq., Air Research and Development Command, USAF P.O. Box 262 Ingelwood, California For: Major George Austin	1
Air Force Special Weapons Center, Commander Commander, Air Force Special Weapons Center Technical Information & Intelligence Office Kirkland Air Force Base, New Mexico Attn: Delmer J. Trester	2
Air Technical Intelligence Center, Wright-Patterson Commander, Air Technical Intelligence Center Wright Patterson Air Force Base, Ohio Attn: H. Holzbauer, AFCIN-4B1a	3
Army Ballistic Missile Agency Commanding General, Army Ballistic Missile Agency Redstone Arsenal, Alabama Attn: ORDAB-c	4-5
Atomic Energy Commission, Washington U.S. Atomic Energy Commission Technical Reports Library Washington 25, D.C. Attn: J.M. O'Leary For: Lt. Col. G.M. Anderson, DRD Capt. John Wittry, DRD Lt. Col. Robert D. Cross, DRE R.G. Oehl, DRE Technical Reports Library	6-10
Air Research and Development Command, Commander Andrews Air Force Base Washington 25, D.C. Attn: RDTAPS, Capt. W.G. Alexander	11

	No. of Copies
*Bureau of Aeronautics Chief, Bureau of Aeronautics Washington 25, D.C. Attn: C.L. Gerhardt, NP	12
Bureau of Ordnance Chief, Bureau of Ordnance Department of the Navy Room 4110 Main Navy Building Washington 25, D.C. Attn: Maryle R. Schmidt or Laura G. Meyers (To be opened by addresses only) For: REN	13, 14, 15
Bureau of Ships, Chief Chief, Bureau of Ships Code 1500 Department of the Navy Washington 25, D.C. Attn: Melvin L. Batt	16
Chicago Operations Office (AEC) U.S. Atomic Energy Commission Chicago Operations Office P.O. Box 59 Lemont, Illinois Attn: A.I. Mulyck For: M. Klein Thomas A. Nemzek	17, 18
Chief of Naval Operations Office of the Chief of Naval Operations Department of the Navy Washington 25, D.C.	19
Conoga Park Area Office (AEC) U.S. Atomic Energy Commission Canoga Park Area Office P.O. Box 591 Canoga Park, California For: A.P. Pollman, Manager	20, 21

	No. of Copies
Department of the Army Atomic Division Office of Chief of Research and Development Department of the Army Washington 25, D.C.	22
Diamond Ordnance Fuse Laboratories Diamond Ordnance Fuse Laboratories Washington 25, D.C. Attn: ORDTL 06.33, Mrs. M.A. Hawkins	23, 24, 25
Jet Propulsion Laboratory Jet Propulsion Laboratory California Institute of Technology Pasadena 3, California Attn: I.E. Newlan, Sup., Tech. Reports Distribution	26
Lockheed Missile Systems Division Asst. AF Plant Representative Missile Systems Division Lockheed Aircraft Corporation P.O. Box 504 Sunnyvale, California	27, 28, 29, 30
Los Alamos Scientific Laboratory Los Alamos Scientific Laboratory P.O. Box 1663 Los Alamos, New Mexico	31
The Martin Company The Martin Company P.O. Box 5042, Mail No. W-711 Middle River, Maryland Attn: AEC Contract Document Custodian For: D. Rauth	32
National Aeronautics and Space Administration, Ames Ames Aeronautical Laboratory Moffett Field, California Attn: Smith J. deFrance, Director	33
National Aeronautics and Space Administration, Langley Langley Aeronautical Laboratory Langley Field, Virginia Attn: Henry J. E. Reid, Director	34

	No. of Copies
National Aeronautics and Space Administration, Lewis Lewis Flight Propulsion Laboratory 21000 Brookpark Road Cleveland 35, Ohio Attn: George Mandel	35
National Aeronautics and Space Administration, Washington National Aeronautics and Space Administration 1512 H Street, N.W. Washington 25, D.C. Attn: Dr. Addison M. Rothrock	36, 37, 38, 39, 40
Naval Ordnance Laboratory Commander, U.S. Naval Ordnance Laboratory White Oak, Silver Spring, Maryland Attn: Eve Liberman, Librarian	41, 42, 43
Naval Research Laboratory Director, Naval Research Laboratory, Code 1572 Washington 25, D.C. Attn: Mrs. Katherine H. Cass	44
Office of Naval Research Office of Naval Research Department of the Navy, Code 735 Washington 25, D.C. Attn: E.E. Sullivan For: Code 429	45
Rand Corporation Director, OSAF Project Rand Via AF Liaison Office The Rand Corporation 1 1700 Main Street Santa Monica, California Attn: F.R. Collbohm For: Dr. Huth	46
Rome Air Development Center, Commander Commander, Rome Air Development Center Griffiss Air Force Base, New York Attn: RCSG, Mr. J.L. Briggs	47

	No. of Copies
School of Aviation Medicine, Randolph AFB School of Aviation Medicine, Randolph AFB Randolph Air Force Base, Texas Attn: Col. J.E. Pickering, Department of Radiobiology	48
Thompson Ramo Wooldridge Thompson Ramo Wooldridge, Inc. Staff Research and Development New Devices P.O. Box 1610 Cleveland 4, Ohio Attn: D.L. Southam	49, 50
Union Carbide Nuclear Co. (ORNL) Union Carbide Nuclear Company X-10 Laboratory Records Department P.O. Box X Oak Ridge, Tennessee	51
University of California Radiation Laboratory, Livermore University of California Radiation Laboratory Technical Information Division P.O. Box 808 Livermore, California Attn: Clovis G. Craig For: Dr. Hayden Gordon	52
Wright Air Development Center, Commander Commander, Wright Air Development Center Wright-Patterson Air Force Base, Ohio Attn: WCACT For: G.W. Sherman, WCLEE Capt. Clarence N. Munson, WCLPS WCOS	53, 54, 55, 56
Technical Information Service Extension U.S. Atomic Energy Commission Reference Branch Technical Information Service Extension P.O. Box 62 Oak Ridge, Tennessee	57-81

	No. of Copies
AI Library Atomics International P.O. Box 309 Canoga Park, California	82-92
Thompson Ramo Wooldridge Library	93-100